Cronfa
Swansea University's Research Repository

Novel wide bandgap semiconductor material based on ternary carbides

An investigation into Al_4SiC_4

By

SIMON FORSTER

Swansea University
Prifysgol Abertawe

UNIVERSITÉ
Grenoble
Alpes

College of Engineering
SWANSEA UNIVERSITY / GRENOBLE UNIVERSITY

A dissertation submitted to Swansea University and Grenoble University in accordance with the requirements of the degree of DOCTOR OF PHILOSOPHY in the Faculty of Engineering.

APRIL 2020

Copyright: The Author, Simon Forster, 2023.

UGA
Université
Grenoble Alpes

INSERER LE LOGO DE
L'UNIVERSITE PARTENAIRE

THÈSE

Pour obtenir le grade de

DOCTEUR DE L'UNIVERSITE GRENOBLE ALPES

Spécialité : **2MGE : Matériaux, Mécanique, Génie civil, Electrochimie**

Arrêté ministériel : 25 mai 2016

Présentée par

Simon FORSTER

Thèse dirigée par **Didier CHAUSSENDE**, Université Grenoble Alpes
et codirigée par **Karol Kalna**, Swansea University

préparée au sein du **Laboratoire Science et Ingénierie des Matériaux et Procédés**
dans **l'École Doctorale I-MEP2 - Ingénierie - Matériaux, Mécanique, Environnement, Energétique, Procédés, Production**

Nouveau matériau semi-conducteur à large bande interdite à base de carbures ternaires - Enquête sur Al4SiC4itre de la thèse en français

Novel wide bandgap semiconductor material based on ternary carbides - An investigation into Al4SiC4

Thèse soutenue publiquement le **9 décembre 2019**,
devant le jury composé de :

Monsieur FABIEN VOLPI
MAITRE DE CONFERENCES HDR, GRENOBLE INP, Examinateur
Monsieur GABRIEL FERRO
DIRECTEUR DE RECHERCHE, CNRS DELEGATION RHONE AUVERGNE, Rapporteur
Monsieur MICHAEL JENNINGS
PROFESSEUR ASSOCIE, UNIVERSITE DE SWANSEA AU PAYS DE GALLES, Examinateur
Monsieur HAROLD CHONG
PROFESSEUR, UNIVERSITE SOUTHAMPTON - GRANDE-BRETAGNE, Rapporteur
Monsieur CHRISTOPHER JOBLING
PROFESSEUR ASSOCIE, UNIVERSITE DE SWANSEA AU PAYS DE GALLES, Examinateur
Monsieur IVAN GLESK
PROFESSEUR, UNIVERSITE DE STRATHCLYDE (GLASGOW) - GB, Président

Abstract

Wide bandgap semiconductor materials are able to withstand harsh environments and operate over a wide range of temperatures. These make them ideal for many applications such as sensors, high-power and radio-frequencies to name a few. However, more novel materials are required to achieve significant power efficiency of various applications or to develop new applications to complement current wide bandgap semiconductors such as GaN and SiC.

In this dissertation, three different methods are used to study one of these novel materials, aluminium silicon carbide (Al_4SiC_4): (1) ensemble Monte Carlo simulations in order to study the electron transport properties of the novel ternary carbide, (2) experimental studies to determine its material properties, and (3) device simulations of a heterostructure device made possible by this ternary carbide. All these methods interlink with each other. Data from each of them can feed into the other to acquire new results or refine obtained results thus leading way to attractive electrical properties such as a bandgap of 2.78 eV or a peak drift velocity of 1.35×10^7 cm s^{-1}. In this work, we are purely focused on the electron transport material properties.

Ensemble Monte Carlo toolbox, developed in-house for simulations of Si, Ge, GaAs, $Al_xGa_{1-x}As$, AlAs, and InSb semiconductors is adopted for simulations of the ternary carbide by adding a new valley transformation to account for the hexagonal structure of Al_4SiC_4. The Monte Carlo simulations predict a peak electron drift velocity of 1.35×10^7 cms^{-1} at electric field of 1400 kV cm^{-1} and a maximum electron mobility of 82.9 cm^{2}V^{-1}s^{-1}. We have seen a diffusion constant of 2.14 cm^{2}s^{-1} at a low electric field and of 0.25 cm^{2}s^{-1} at a high electric field. Finally, we show that Al_4SiC_4 has a critical field of 1831 kV cm^{-1}. In the experimental part, Al_4SiC_4 semiconductor crystals are used that had previously been grown at IMGP, one by solution grown and the other by sublimation growth. Three different experiments are performed on them: (1) ultraviolet (UV), infrared (IR) and visible (Vis) Spectroscopy, (2) X-ray Photo Spectroscopy, and (3) two-probe measurements where metal contact are grown on the crystals. Here we have found a bandgap of 2.78 ± 0.02 eV UV, IR and Vis Spectroscopy and a thick oxide layer on the samples using XPS. The two-probing DC current-voltage measurements revealed a resistivity of 2.2165×10^{10} Ωm and a conductivity of 4.5117×10^{-11} Sm^{-1}.

A commercial software Atlas by Silvaco is utilized to predict performance of heterostructure devices with gates lengths of 5 μm, 2 μm and 1 μm, made possible by the ternary carbide in a combination with SiC. The 5 μm gate length SiC/Al_4SiC_4 heterostructure transistor delivers a maximum drain current of 168 mA/mm, which increases to

244 mA/mm and 350 mA/mm for gate lengths of 2 μm and 1 μm, respectively. The device breakdown voltage is 59.0 V which reduces to 31.0 V and to 18.0 V for the scaled 2 μm and the 1 μm gate length transistors. The scaled down 1 μm gate length device switches faster because of the higher transconductance of 65.1 mS/mm compared to only 1.69 mS/mm for the largest device. Finally, a sub-threshold slope of the scaled devices is 197.3 mV/dec, 97.6 mV/dec, and 96.1 mV/dec for gate lengths of 5 μm, 2 μm, and 1 μm, respectively.

Overall, Al_4SiC_4 has the potential to work in many electronic applications such as high electron mobility transistors, quantum well based semiconductor transistors, light emitting diodes, and X-ray sensors. Al_4SiC_4 can be used alongside current SiC technologies because of the similarities between its crystal lattice and the crystal lattice of SiC as well as chemical compatibility.

However, currently due to a large effective mass, that we calculated using a dispersion relation on the minima of the conduction band, has given a limited electron drift velocity and electron mobility which could limit the usability of Al_4SiC_4 in this study.

Dedication and acknowledgements

First, I would like to express my sincere gratitude to my supervisors Professor Karol Kalna and Dr Didier Chaussende for giving me this big opportunity. I would also like to thanks them for all their support throughout my Ph.D and for all their patience, motivation and extensive knowledge. They have undoubtedly been the best supervisors and mentors for my Ph.D study.

Besides my supervisors I would like to express my thanks to the rest of the Nano-Electronics Device Computational group at Swansea University, that being Dr Antonio Martinez, Dr Alnazer Mohamed, Dr Khaled Gribi and Mustafa Alqayasi who have all given me advice and contributed in some way to my Ph.D. On top of this I would like to thank Dr Thierry Maffeis, Dr. Sven Tengeler and Darmstadt Technical University for lending me their time and access to machinery in order to perform X-ray Photoelectron Spectroscopy experiments, without them I would not have been able to achieve what I did. I would also like to thank Professor Julien Pernot and the Neel Institute for lending me their time and access to machinery in order to perform the two- and four-probe current-voltage measurements, again without this I would not have been able to achieve what I did.

Last but not least I would like to thank my family and friends for supporting me in many ways throughout my Ph.D, especially during the time I was writing my thesis. Here I would like to off a special thanks to my Mother Debbie Wolton, Step Mother Lillian Wolton, siblings Luke and Laura Wolton and finally to two close friends Nick Jones and Stuart Layzell

AUTHOR'S DECLARATION

I declare that the work in this dissertation was carried out in accordance with the requirements of the University's Regulations and Code of Practice for Research Degree Programmes and that it has not been submitted for any other academic award. Except where indicated by specific reference in the text, the work is the candidate's own work. Work done in collaboration with, or with the assistance of, others, is indicated as such. Any views expressed in the dissertation are those of the author.

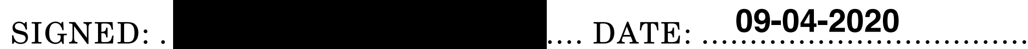
SIGNED: .... DATE: 09-04-2020

I hereby give consent for my thesis, if accepted, to be available for photocopying and for inter-library loan, and for the title and summary to be made available to outside organisations.

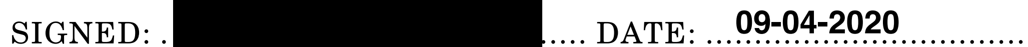
SIGNED: .... DATE: 09-04-2020

List of Contributions

Journal Publications

S. FORSTER, D. CHAUSSENDE, AND K. KALNA, *Monte Carlo simulations of electron transport characteristics of ternary carbide* Al_4SiC_4, ACS Applied Energy Materials **2**, pp. 715–720, 2019.

Conference Proceedings

S. FORSTER, J. CAÑAS, F. LLORET, M. GUTIÉRREZ, D. ARAUJO, K. KALNA, AND D. CHAUSSENDE, *Experimental extraction of the bandgap for* Al_4SiC_4, in Proceedings of ECSCRM, pp. 60, 2018.

S. FORSTER, J. CAÑAS, F. LLORET, M. GUTIÉRREZ, D. ARAUJO, K. KALNA, AND D. CHAUSSENDE, *Experimental extraction of the bandgap for* Al_4SiC_4, in Proceedings of UK Semiconductor (Sheffield, UK, 4-5 July 2018), pp. 180, 2018.

S. FORSTER, B. UBOCHI, AND K. KALNA, *Monte Carlo Simulations of Electron Transport in Bulk GaN*, in Proceeding of the International Workshop on Computational Nanotechnology (IWCN2017)(Windermere, U.K., 6-9 June 2017), pp. 135-137, 2017.

In-House Conferences

S. FORSTER, J. CAÑAS, F. LLORET, M. GUTIÉRREZ, D. ARAUJO, K. KALNA, AND D. CHAUSSENDE, *Experimental Study of* Al_4SiC_4, Zienkiewicz Centre for Computational Engineering (ZCCE2019)(Swansea, UK., January 2019)(Poster).

S. FORSTER, J. CAÑAS, F. LLORET, M. GUTIÉRREZ, D. ARAUJO, K. KALNA, AND D. CHAUSSENDE, *Electron and Optical Characteristics in Bulk* Al_4SiC_4, Swansea Grenoble Conference (Swansea, UK., November 2018)(Poster).

S. FORSTER, K. KALNA, A. MARTINEZ MUNIZ, AND D. CHAUSSENDE, *Novel wide bandgap semiconductor materials based on ternary carbides*, Zienkiewicz Centre for Computational Engineering (ZCCE2017)(Swansea, UK., January 2017)(Poster).

TABLE OF CONTENTS

Page

List of Tables **xiii**

List of Figures **xv**

1 Applications of Wide Bandgap Semiconductors **1**

1.1 What are Wide Bandgap Semiconductors? 1
1.2 Why Do We Want Wide Bandgap Semiconductors? 2
1.3 Wide Bandgap Semiconductor Applications 5
1.3.1 Wide Bandgap Semiconductors in High Power, High Temperature Electronics 5
1.3.2 Wide Bandgap Semiconductors in Radio-Frequency Applications . 6
1.3.3 Wide Bandgap Semiconductors in the Opto-Electronics and Lighting Applications 6
1.3.4 Wide Bandgap Semiconductors in Sensors 7
1.3.5 Aluminum Silicon Carbide in Wide Bandgap Semiconductors Applications 8
1.4 Aim and Objectives of the PhD Thesis 8
1.4.1 Ensemble Monte Carlo Simulations 9
1.4.2 Technology Computer Aided Design Device Simulations 9
1.4.3 Experimental Methods 10
1.5 Layout of the PhD Thesis 10

2 Aluminum Silicon Carbide **13**

2.1 History of Calculations of Material Properties 13
2.2 History of Experimental Measurements 15
2.3 Material Properties 18
2.4 Summary 22

3 Theoretical Background **25**

3.1 Effective Mass . . . 25

3.2 Boltzmann Transport Equation . . . 26

3.3 Bulk Ensemble Monte Carlo Simulations . . . 27

3.3.1 The Ensemble Monte Carlo Method . . . 28

3.3.2 Free Flight Generation . . . 29

3.3.3 Final State After Scattering . . . 31

3.3.4 Ensemble Monte Carlo Simulation . . . 32

3.3.5 Fermi's Golden Rule . . . 33

3.3.6 Scattering Process . . . 34

3.4 Beer-Lambert Law . . . 37

3.5 Semiconductor Light Absorption . . . 38

3.6 Band Tailing . . . 41

3.7 Photoelectric Effect . . . 43

3.8 X-ray Photons for X-ray Photoelectron Spectroscopy . . . 43

3.9 Four Probe Method . . . 44

3.10 Device Modelling . . . 46

3.10.1 Field-Dependent Mobility . . . 46

3.10.2 Shockley-Read-Hall Recombination . . . 47

3.10.3 Auger Recombination . . . 47

3.10.4 Poisson's Equation . . . 48

3.10.5 Continuity Equation . . . 49

3.10.6 Drift-Diffusion Transport Model . . . 50

3.11 Summary . . . 51

4 Methodology **53**

4.1 Ensemble Monte Carlo Simulator . . . 53

4.1.1 Monte Carlo Implementation . . . 54

4.1.2 Wave-vector Transformation . . . 57

4.2 Experimental Methods . . . 59

4.2.1 Spectrophotometry . . . 59

4.2.2 X-Ray Photoelectron Spectroscopy . . . 61

4.2.3 Two and Four Probe Measurements . . . 62

4.3 Technology Computer Aided Design . . . 62

4.3.1 Structure Specification . . . 64

4.3.2 Material Models and Method Specification 65
4.4 Summary 67

5 Computational Results **69**
5.1 Monte Carlo Simulations 69
5.1.1 Electron Transport Results 69
5.2 Device Simulations 74
5.2.1 Transistor Simulations 77
5.2.2 Device Structure 78
5.2.3 Device Model 79
5.2.4 Scaled SiC/Al_4SiC_4 Heterostructure Transistors 80
5.3 Discussion 84

6 Experimental Results **89**
6.1 Introduction 89
6.2 UV/Vis/NIR spectroscopy 90
6.3 XPS 92
6.3.1 Composition 92
6.3.2 Valence Band 96
6.3.3 Workfunction 100
6.3.4 Depth Profiling 102
6.4 I-V Measurements 105
6.5 Discussion 113

7 Summary and Conclusion **115**
7.1 Summary 115
7.2 Conclusion 119

Bibliography **121**

LIST OF TABLES

TABLE **Page**

2.1 A comparison of Al_4SiC_4 to other semiconductor material parameters. 20
2.2 Comparison of published energy band gaps for Al_4SiC_4 indicating a method and a source 21

4.1 Electron-phonon transitions considered in the bandstructure model of Al_4SiC_4 for the MC simulations of electron transport. 57
4.2 Al_4SiC_4 material parameters. 58

5.1 Corresponding dimensions of the scaled heterostructure transistors shown in Figure 5.15. Note that L_S and L_D dimensions in Figure 5.15 are assumed to be a large enough to make good Ohmic contacts. 79
5.2 Al_4SiC_4 material parameters considered in the simulations of heterostructure transistors. The electron mobility is calculated at an applied electric field of 0.01 kV/cm. 80
5.3 Maximum transconductance of the scaled heterostructure transistors. 83

6.1 Table of the chemical elements picked up in the XPS survey spectrum of Al_4SiC_4 in Figure 6.3 with their corresponding binding energy. 92
6.2 Percentage of chemical elements found in each of the XPS survey spectra as shown in the pie charts of Figures 6.4(a) - 6.4(f). 95
6.3 Comparison of resistivity, conductivity for Al_4SiC_4, un-doped GaN and un-doped 4H-SiC. Note: The doping has a large impact on the resistivity and conductivity and so these values might vary considerably. 110

List of Figures

Figure **Page**

1.1 Energy Band Gaps in Materials. 2
1.2 Pie chart of the elements in the Earth's crust. 3

2.1 (a) 2D hexagonal (0001) plane showing the location of the *M* valleys within the Al_4SiC_4 hexagonal structure and (b) a 3D hexagonal structure showing locations of principal valleys. 18
2.2 Crystal structures of Al_4SiC_4. 19
2.3 Re-scaled Al_4SiC_4 bandstructure 21
2.4 Polarized Raman spectra of Al_4SiC_4 single crystals. Spectra collected on the crystal surface (laser propagation along the *c*-axis) 23
2.5 Polarized Raman spectra of Al_4SiC_4 single crystals. Spectra collected on the crystal edge (laser propagation parallel to the crystal surface) 23

3.1 Generalized idea of the dispersion relation in a conduction band fitted with a polynomial trendline. 27
3.2 Evolution of particles in a Monte Carlo simulation. 29
3.3 Beer-Lambert law schematically showing the incident light, the sample and the transmitted light. 38
3.4 Transitions from the valence band to the conduction band: direct bandgap (a) and indirect bandgap (b). 39
3.5 Density of state for: ideal (a) and real semiconductor (b). 40
3.6 Theoretical curve shape of a Tauc Plot, showing a linear fit to determine the semiconductor optical bandgap. 41
3.7 Complex Tauc plot showing three different regions. 42
3.8 Schematic of a linear 4-Probe set up. 44
3.9 Van der Pauw four-probe set up. 45
3.10 Hall Voltage Measurement Configurations. 46

3.11 Groupings for generation - recombination process 48

4.1 Re-scaled Al_4SiC_4 bandstructure with two black arrows indicate the two valleys that we are considered in the MC simulations. 55

4.2 Schematic of conduction band minimum valleys in Al_4SiC_4 showing the number of equivalent bands in each valley and the separation between the two considered valleys. 56

4.3 Location of the M valleys within the Al_4SiC_4 hexagonal structure 58

4.4 Perkin Elmer Lambda 950 spectrophotometer. 60

4.5 Geometric set up of the UV/Vis/NIR Spectroscopy chamber. 61

4.6 Two-probe set up. 62

4.7 Probing station set up in Grenoble at Neel Institute with the chamber lid removed. 63

4.8 Side view of the probing station set up in Grenoble at Neel Institute with the chamber lid on and light shining onto the sample. 63

4.9 Flow diagram showing the process device CAD takes in order to run a simulation. 64

4.10 Schematic of the 5 μm gate heterostructure device that is studied. Full dimensions for the device are quoted in Chapter 5 65

4.11 Example of a mesh design for a heterostructure device. Here a 5 μm gate device is shown 66

5.1 (a) 2D hexagonal (0001) plane and showing the location of the M valleys within the Al_4SiC_4 hexagonal structure, where $\theta = \pm 60°$. (b) 3D hexagonal structure showing location of principal valleys. 70

5.2 Electron drift velocity on a linear scale as a function of applied electric field in bulk Al_4SiC_4 simulated below the critical electric field 71

5.3 The same electron drift velocity as in Fig. 5.2 but on a logarithmic scale as a function of applied electric field in bulk Al_4SiC_4 simulated below the critical electric field. 71

5.4 Average electron kinetic energy as a function of applied electric field in bulk Al_4SiC_4 simulated below the critical electric field. Red line show the thermal energy of electrons at 25.8 meV and the blue line the average kinetic energy of the electrons. 72

5.5 The same average electron kinetic energy as a function of applied electric field in bulk Al_4SiC_4 as in Fig. 5.4 but the field in plotted on logarithmic scale, simulated below the critical electric field. 72
5.6 Electron mobility on a linear scale as a function of applied electric field in bulk Al_4SiC_4 simulated below the critical electric field. 73
5.7 The same electron mobility as in Fig. 5.6 but on a logarithmic scale as a function of applied electric field in bulk Al_4SiC_4 simulated below the critical electric field. 73
5.8 Electron diffusion as a function of applied electric field on a linear scale in a bulk Al_4SiC_4 simulated below the critical electric field. 75
5.9 The same electron diffusion as a function of applied electric field in bulk Al_4SiC_4 as in Fig. 5.8 but on a logarithmic scale simulated below the critical electric field. 75
5.10 Stacked plot of the calculated valley occupancy of electrons in the three M and K valleys as a function of applied electric field in bulk Al_4SiC_4. 76
5.11 Electron mobility as a function of ionized impurity concentration in bulk Al_4SiC_4 at an applied electric field of 1 kV/cm. 76
5.12 Conduction and valence band profiles (left) overlapped with electron density (right) across the middle of the 5 μm gate length device in an off-state with zero bias applied (a), and in an on-state at V_D=5 V and V_G=1 V (b). 77
5.13 Conduction and valence band profile (left) overlapped with electron density (right) across the middle of the 2 μm gate length device in an off-state with zero bias applied (a), and in an on-state at V_D=5 V and V_G=1 V (b). 77
5.14 Conduction and valence band profile (left) overlapped with electron density (right) across the middle of the 1 μm gate length device in an off-state with zero bias applied (a), and in an on-state at V_D=5 V and V_G=1 V (b). 78
5.15 Cross-section of the heterostructure SiC/Al_4SiC_4 transistor designed for power applications, see Table 5.1 for dimensions. The concentration of n-type doped 4H-SiC layer is $2.5 \times 10^{18} cm^{-3}$. 79
5.16 $I_D - V_G$ characteristics at indicated drain biases (V_D) for the 5 μm gate length SiC/Al_4SiC_4 heterostructure transistor. 81
5.17 $I_D - V_G$ characteristics at indicated drain biases (V_D) for the scaled SiC/Al_4SiC_4 heterostructure transistor with a 2 μm gate length. 82
5.18 $I_D - V_G$ characteristics at indicated drain biases (V_D) for the scaled SiC/Al_4SiC_4 heterostructure transistor with a 1 μm gate length. 83

5.19 Breakdown of 59.0 V for a heterostructure device at a $V_G = 0$ with a 5 μm gate length on a linear scale (left) on a log scale (right) 84
5.20 Breakdown of 31.0 V for a heterostructure device at a $V_G = 0$ with a 2 μm gate length on a linear scale (left) on a log scale (right). 85
5.21 Breakdown of 18.0 V for a heterostructure device at a $V_G = 0$ with a 1 μm gate length on a linear scale (left) on a log scale (right). 86

6.1 Wave-number as a function of the light transmission through the solution grown sample of Al_4SiC_4 obtained from the UV/Vis/NIR spectroscopy. 90
6.2 Tauc plot showing photon energy as a function of absorption coefficient, showing a best fit to the Urbach tail giving a bandgap of 2.11 eV, as well as further band tailing giving a bandgap of 2.78 eV. 91
6.3 XPS survey spectra for a sublimation grown sample of Al_4SiC_4 over the range of 0 – 1200 eV measured on the DAISY FUN system at Darmstadt University. Here the peaks detail where certain elements have been found. We have added lines to these peaks to show what the elements are. 93
6.4 Compositions of surface treated or angled samples taken from XPS survey spectra that were recorded on the DAISY FUN system at Darmstadt University: annealed sample (a), ARXPS sample (b), unprocessed sample (c), sputtered at 250 V sample (d), sputtered at 500 V sample (e), wet etched sample (f). 94
6.5 XPS valence band profiles obtained on the DAISY FUN system at Darmstadt University for the unprocessed sample. A fitted step down function (blue line) and a tangent to this (red line) are also shown. The point at which the tangent crossed the axis is noted on each of the figures, this is the amount the Fermi level lies above the valence band. 97
6.6 XPS valence band profiles obtained on the DAISY FUN system at Darmstadt University for the unprocessed sample. A fitted step down function (blue line) and a tangent to this (red line) are also shown. The point at which the tangent crossed the axis is noted on each of the figures, this is the amount the Fermi level lies above the valence band. 97
6.7 XPS valence band profiles obtained on the DAISY FUN system at Darmstadt University for the sputtered sample at 500 V. A fitted step down function (blue line) and a tangent to this (red line) are also shown. The point at which the tangent crossed the axis is noted on each of the figures, this is the amount the Fermi level lies above the valence band. 98

6.8 XPS valence band profiles obtained on the DAISY FUN system at Darmstadt University for the wet etched sample with HF. A fitted step down function (blue line) and a tangent to this (red line) are also shown. The point at which the tangent crossed the axis is noted on each of the figures, this is the amount the Fermi level lies above the valence band. 98

6.9 XPS valence band profiles obtained on the Kratos Supra XPS spectrometer at Swansea University for the unprocessed sample. A fitted step down function (blue line) and a tangent to this (red line) are also shown. The point at which the tangent crossed the axis is noted on each of the figures, this is the amount the Fermi level lies above the valence band. 99

6.10 XPS valence band profiles obtained on the Kratos Supra XPS spectrometer at Swansea University for the sputter sample at 5 keV . A fitted step down function (blue line) and a tangent to this (red line) are also shown. The point at which the tangent crossed the axis is noted on each of the figures, this is the amount the Fermi level lies above the valence band. 99

6.11 UPS spectrum obtained on the DAISY FUN system at Darmstadt University showing the secondary cut-off point and the calculated workfunction for: unprocessed sample (a), and annealed sample (b). 101

6.12 UPS spectrum obtained on the DAISY FUN system at Darmstadt University showing the secondary cut-off point and the calculated workfunction for: sputter sample at 500V (a), and wet etched sample with HF (b). 101

6.13 UPS spectrum obtained on the Kratos Supra XPS spectrometer at Swansea University showing the secondary cut-off point and the calculated workfunction for: unprocessed sample (a), and sputter sample at 5 keV (b). 101

6.14 Microscope image of the Al_4SiC_4 sample under the Kratos Supra XPS spectrometer showing the area that has been sputtered, by the slightly darker square area. 102

6.15 Depth profile made up of XPS spectra in the O1s region during the 35 sputterings. The first spectra is at the further point along the z-axis and the last spectra is at the front of the z-axis in order to show the reduction of the O1s peak as the sputters take place. 103

6.16 Depth profile made up of XPS spectra in the C1s region during the 35 sputterings. The first spectra is at the front of the z-axis and the last spectra is at the further point along the z-axis. 104

6.17 XPS spectra taken from the middle of the C1s depth profile, see Figure 6.16, showing the chemical bonds that are present. 104
6.18 Final XPS spectrum of the C1s region after all the 35 sputterings have taken place and showing the chemical bonds that are present. 106
6.19 Depth profile made up of XPS spectra in the Al 2p region during 35 sputterings. First sputter is at the front of the z-axis and the last sputter is at the back of the z-axis 106
6.20 XPS spectra taken from the middle of the Al 2p depth profile, see Figure 6.19, showing the chemical bonds that are present. 107
6.21 Final XPS spectra of the Al 2p region after all the 35 sputterings have taken place and showing the chemical bonds that are present. 107
6.22 Four samples prepared and attached to a sapphire crystal. 108
6.23 I-V characteristics obtained from two probe measurements the Ossila four-probe system at Swansea University. Blue line shows the data collect and the red line is a linear fit against the slope. 108
6.24 I-V characteristics obtained from two probe measurements on the Ametek ModuLab XM Material Test System at Neel Institute. Blue line shows the data collect and the red line is a linear fit against the slope. 109
6.25 I-V characteristics obtained from two probe measurements for a sample with silver epoxy contacts showing the type of contact that is being made with the probes and the sample. 110
6.26 Microscope image of the Al_4SiC_4 sample showing the measured distance between the two probes. 111
6.27 Microscope image of the Al_4SiC_4 sample showing the measured width of the sample. 111
6.28 Microscope image on the Ametek ModuLab XM Material Test System showing the Al_4SiC_4 sample with four probes attached. 112
6.29 Microscope image of a Al_4SiC_4 sample with six titanium contacts grown on top.113

CHAPTER 1

Applications of Wide Bandgap Semiconductors

This chapter gives an introduction to the topic of wide bandgap semiconductors and the motivation behind why we want to use them over standard semiconductors. The latter part of the chapter will give details on the aims of this thesis and an overview of contents of the upcoming chapters.

1.1 What are Wide Bandgap Semiconductors?

Wide bandgap (WBG) semiconductors are named after their relative wide energy bandgap in comparison to silicon. This energy bandgap is an energy gap between the top of the valence band and the bottom of the conduction band in a material as illustrated in Figure 1.1.

When a material has a bandgap, the electrons can jump from the valence band to the bottom of the conduction band by means of thermal or optical excitation. This means that the material can conduct current or not conduct under externally adjusted conditions hence the name semi-conductor. The existence of the bandgap allows suitably designed semiconductor devices to be used as switches, diodes and other electronic components including the ability to switch currents on and off based on the electrical function they perform. The larger this energy bandgap, the larger electric field can be supported with material breakdown allowing the WBG materials to perform more efficiently in power applications than silicon does. Well designed WBG devices can achieve characteristics such as larger tolerance to high operating temperatures and other harsh environments

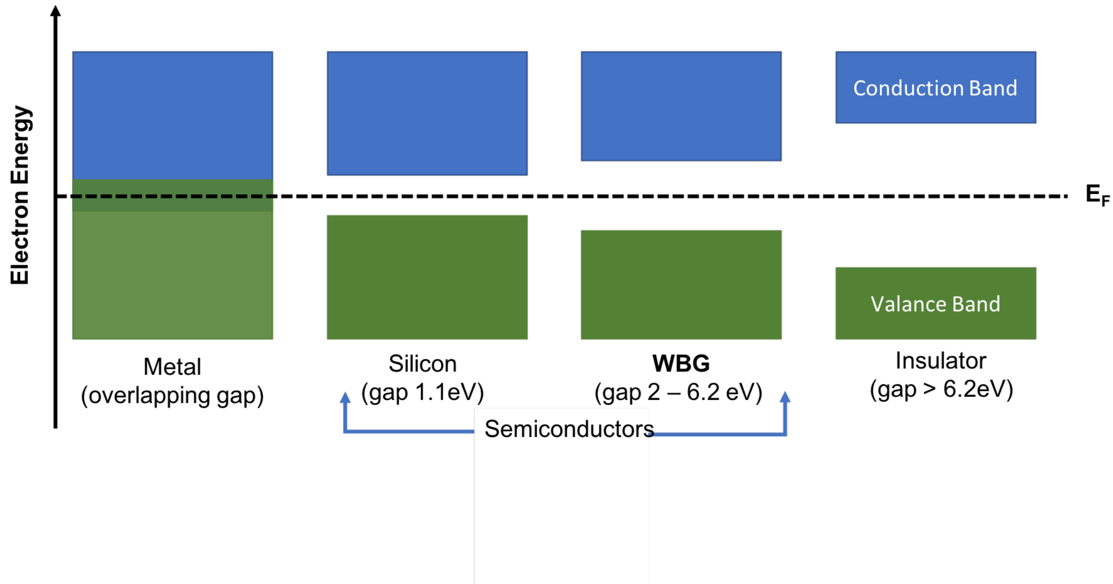

FIGURE 1.1. Energy Band Gaps in Materials.

like high radiation or large voltage environments. The WBG materials used in today's commercial applications are 4H-silicon carbide (SiC) and gallium nitride (GaN) with bandgaps of 3.23 eV [1] and 3.4 eV [2], respectively. However, both 4H-SiC and III-nitrides based semiconductor devices suffer from performance and reliability issues that hamper their employment into power and RF applications. Therefore, there is a prolonged need for more novel WBG materials which would overcome those issues. This work aims to examine and characterize one of these novel materials, aluminum silicon carbide (Al_4SiC_4), to see if the properties are suitable for use in electronic, opto-electronic or power applications.

1.2 Why Do We Want Wide Bandgap Semiconductors?

The invention of silicon (Si) integrated circuit over half a century ago laid the foundations of modern computing, communication, and data handling creating nowadays electronics era. Circuits made of silicon transistors are now the predominant commercial semiconductors material option for the majority of power diodes and switches used in power electronic systems. This has been mainly due to abundance of silicon, as it is seen in dusts, sands, planetoids and planets as a multitude of forms such as silica or silicates.

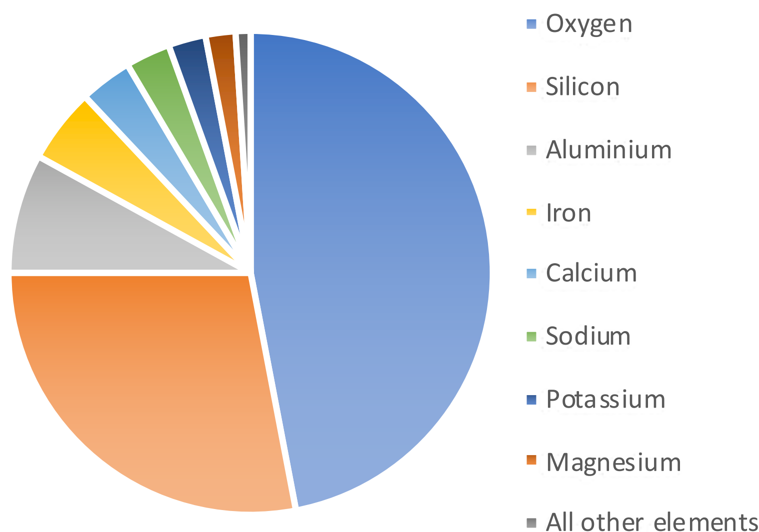

FIGURE 1.2. Pie chart of the elements in the Earth's crust data. From M. Fleischer [4].

On Earth alone, 90% of the crust is comprised of silicate minerals, thus making it the second most abundant element on Earth after oxygen (O), see Figure 1.2.

Silicon is unable to be used indefinitely because of operational issues such as adverse heating resulting from increasing population density of transistors as well as ever increasing leakage current due to the short channel effects occurring with transistor scaling [3]. The transistor self-heating has become very challenging to create new transistor chips with greater power density and energy efficiency to meet market demands.

Further more, the electronic and material properties of silicon like relatively large electron and hole mobility and saturation velocity, relatively wide energy bandgap, and existence of native oxide with a very good interface properties make it an ideal material to use for diodes, transistors and sensors. However, in many modern applications and, especially, in those environments classed as harsh, silicon has reach its physical limits [5]. The limitation of silicon electronics has led a way to the exploration of new novel semiconductor materials such as WBG semiconductor and silicon-on-insulator (SOI) adding new semiconductor technologies to the modern computing and electronic era.

Definition of the Harsh Environments

Harsh environments can include, but are not limited to:
High temperature $> 125°$ C, low temperature $< -40°$ C, high radiation > 100 Mrads, high voltage 1000 V (AC) or 1500 V (DC), high shock $> 50{,}000$ g, high frequency > 3 MHz and erosive flow and corrosive media (aggressive media).

Such novel WBG semiconductors with include SiC, GaN, AlN, indium gallium nitride (InGaN), diamond and β gallium oxide (β-Ga_2O_3) [6] to name a few. These WBG semiconductors have extended electrical properties over silicon and, therefore, do not break down as rapidly in the extreme environments and allow the operation of power electronics to continue even under these conditions. The WBG semiconductor based electronics finds its applications from electric and hybrid cars, buses and lorries, domestic appliances, energy distribution, ocean mining to space, and planetary exploration to nuclear reactors to X-ray detection.

The WBG semiconductor search to replace silicon technology in power applications and harsh environments sees materials such as SiC and GaN emerging as front runners to compensate for the slow-down in silicon in the high power, higher temperature domains. These two WBG materials have roughly ten times better conduction and switching power to that of silicon. WBG materials look to be the natural route to go for future power electronics. WBG materials also look to be able to produce devices that are smaller and more efficient along with having the ability to withstand harsh environments. Research in WBG materials estimates that replacing silicon with SiC or GaN can enhance many power electronic device metrics such as the increased DC-DC conversion efficiency from 85% to 99% [7, 8], AC to DC from 85% to 98% [9], and to optimize the efficiency of DC to AC from 96% to 99% [10]. Not only do power electronics benefit from the properties of WBG materials, but also RF applications. Where WBG semiconductor materials overcome the issues that the telecommunications industry face today with silicon-based RF power transistors.

Further more, WBG materials can also emit light. Therefore, WBG materials are suitable for various opto-electronic applications especially in the solid-state lighting industry, where GaN-based light emitting diodes (LEDs) provide energy-saving, durability and a long-life alternative to the old incandescent light bulbs. GaN has also become the choice for laser diodes, especially with the ever increasing popularity of Blu-Ray technology.

1.3 Wide Bandgap Semiconductor Applications

1.3.1 Wide Bandgap Semiconductors in High Power, High Temperature Electronics

Power electronics is ubiquitous today, as the majority of devices that use electricity, employ a power management unit such as ICs, PMICs or PMU, all of which are integrated circuits or system-on-a-chip devices. It was not until 1992 that WBG semiconductors [11] made their debut. Prior to this, silicon devices such as bipolar transistors were used. WBG semiconductor materials bring many advantages for power electronics when compared to mature semiconductor materials such as silicon. Such advantages are lower losses for higher efficiency, high switching frequency, volumetric efficiency, higher operating temperature (in excess of the maximum for silicon, 150°C), robustness in harsh environments, and high breakdown voltage. Such advantages lead way to lower capacitance and inductance which are ideal for filters. WBG materials can achieve a larger effective heat removal from devices which is necessary due to the self-heating that occurs at higher switching frequencies. Lower intrinsic carrier concentration at room temperature giving a greater thermal control before devices become overwhelmed with thermally generated carriers. These WBG semiconductor materials are also shown to work at low temperatures (-50°C), making them suitable over room temperatures and beyond. High power, high temperature electronics device applications span a wide range of uses from industrial uses to automotive and transport systems to wireless communications to clean energy generation. Such advantages, as mentioned above, are now enabling an almost unlimited number of device applications especially in the field of power electronics, where inverter yields have increased in excess of 2% due to the ability of these devices working at high frequency with low switching losses and ultra-fast switching regardless of temperature. Comparing a WBG semiconductor device such as a SiC diode to a silicon bipolar diode, a reduction in turn-on losses of 70% [12] can be seen for the SiC diode.

High Power devices are expected to work if possible at AC voltages in excess of 1000V and so Al_4SiC_4 based devices will be investigated to see if the breakdown voltage can achieve this. We would especially like to see breakdown voltage greater than for instance a AlGaN/GaN HEMT which can achieve breakdown voltages of at least 600 V [13]. If this is possible we could see new devices for power electronics industry based on our material Al_4SiC_4.

1.3.2 Wide Bandgap Semiconductors in Radio-Frequency Applications

As we all become more and more connected with each other and prefer a wireless communication, the range of radio-frequency (RF) devices is in a constant need of the expansion and their performance in a need of improvement to handle all the communication requests. Unfortunately, silicon-based RF devices such as power transistors have almost each their limits of power density, breakdown voltage and operating frequency to name a few. Therefore, a new material is needed in order to take RF devices further, this is where WBG semiconductors come into it. Comparing the most common WBG semiconductor, GaN, to silicon-based RF power transistors, the advantages seen are 3-5 times larger power densities and, therefore, reduced input and output capacitances, increased bandwidth, easier impedance matching, high breakdown voltage, lower losses for high efficiency, high temperature operation and larger transconductance. These advantages allow telecommunication industries to make considerable performance enhancements, taking RF devices from one generation into the next generation.

If Al_4SiC_4 devices could achieve a larger transconductance in comparison to, for instance, a AlGaN/GaN HEMT which can achieve a transconductance of 120 mS/mm [14], it could provide new devices for RF electronics that work at high temperatures and in harsh environments.

1.3.3 Wide Bandgap Semiconductors in the Opto-Electronics and Lighting Applications

More and more of our electronic devices are using LEDs from TV displays, to mobile phones to traffic lights. This has all become possible due to WBG semiconductors, mainly GaN and InGaN, taking the industry away from incandescent and filament-based lighting. Comparing LEDs to incandescent lighting, we see that LEDs convert 90% of their energy into light and only 10% into heat [15], while incandescent convert only 10% of their energy to light and 90% to heat [16] and so are extremely inefficient. Both the life expectancy and brightness of LEDs also surpasses that of incandescent lighting where LEDs last around 40 times longer [17] and produce 10 times more light (lumens) per watt [18]. These advantages result in high efficiency, ultra-fast switching, durability of devices based on WBG semiconductors which are also environmentally friendly (mercury-free). Significant savings through energy costs can be made and further applications beyond lighting are coming to fruition. Without the LEDs, the TV industry would not be where

they are today, and we would not have ultra-thin TVs and Blu-ray players.

Al_4SiC_4 has a potential to be used in opto-electronic as it has a very distinct bandgap which could produce light with wavelength of around 500 nm (green light) based up a bandgap of 2.5 eV. Here the material could compete with LEDs based on Ba_2SiO_4 phosphors [19] and InGaN/GaN [20] material systems.

1.3.4 Wide Bandgap Semiconductors in Sensors

In recent years, there has been much interested in the use of surface functionality of thin film and nanowire WBG semiconductors to produce sensors [21]. Such WBG semiconductors, that are of interest for sensing applications, are GaN, InN, ZnO and SiC. This is due to the need for chemical sensors to detect a target with high specificity and great sensitivity. The WBG materials can be tuned for sensing gases [21–24], heavy metals [21, 25], UV photons [21, 25], and biological molecules [21, 25] and can be used in a variety of applications from homeland security, medical, and environmental monitoring to food safety.

Through tuning these materials, electro-chemical measurements based on impedance and conductance and, in some cases, electrical measurements of micro-cantilever resonant frequency, changes in their operation can be measured. Quite often these materials are coated with a catalyst such as Pd or Pt in order to increase their detection sensitivity [26–29]. There are however other way of increasing detection sensitivity and functionality of the surface by use of oxides [30], polymers [31] and nitrides [32] depending on the application. Another type of sensors, that are in demand, are those for detecting X-rays and gamma rays [33] with WBG semiconductor materials such as CdTe [34] and CdZnTe [35]. The reasons for WBG semiconductors becoming popular choice for sensors is due to their ability to withstand harsh environments, ability to work in a wide range of temperatures, and the ability to integrate with existing GaN-based UV light-emitting diodes, UV detectors, and wireless communication chips. There is, however, still a lot of research needed as the majority of these devices are not ready for commercialization. This is due to numerous issues these device have regarding signal-to-noise ratio, size, and the time taken to make a detection (exceeding 2 hours [21]). Al_4SiC_4 is currently envisioned for X-ray detectors due to its potential to withstand large amounts of radiation. The Al_4SiC_4 could be used as a stand alone material or in parallel with SiC X-ray detectors [36].

1.3.5 Aluminum Silicon Carbide in Wide Bandgap Semiconductors Applications

There are many potential applications for Al_4SiC_4 as a WBG semiconductor material if we are able to synthesis it in large enough crystals. As Al_4SiC_4 has a smaller bandgap than than SiC, this ternary semiconductor might be used to design carbide heterostructures, carbide heterojunctions, or carbide quantum well devices such as a SiC/Al_4SiC_4 high electron mobility transistor (HEMT). The density of interface states between Al_4SiC_4s and SiC might be reduced when compared to the density of the interface states between oxide based dielectric layers and SiC due to the close matching of the lattice constants between the two materials. These heterostructure SiC/Al_4SiC_4 HEMTs could compete with such devices as as a AlGaN/GaN HEMTs [37] for high-energy-efficiency applications.

The heterostructure SiC/Al_4SiC_4 material system can allow to tailor the energy bandgap a value between the two bandgap values of the two components of 2.8 eV and 3.4 eV by adjusting the width of the quantum well. Other applications for Al_4SiC_4 could be in opto-electronics as it has a very distinct bandgap which could produce light with wavelength of around 500 nm (green light) based up a bandgap of 2.5 eV where it could compete with such LEDs as Ba2SiO4 phosphors [19] and InGaN/GaN [20] or take away the need to filter out light from other colour LEDs which requires to 30% of the light being filtered out [38]. The light absorption of Al_4SiC_4 around the green light spectrum could have the potential to be used in photovoltaics as thin films and as photo-electrochemical water splitting as the high-energy light absorber. Al_4SiC_4 also has a potential to work as an X-ray detector where it could either replace the SiC X-ray detectors [39] or work in parallel with them, due to its high tolerance to radiation and ability to absorb at a different energy value to that of SiC.

On top of these applications, Al_4SiC_4 is compatible with the 4H-SiC or the 6H-SiC technologies by having a close crystal lattice constant and by having a chemical compatibility with 4H-SiC and 6H-SiC giving way to many SiC/Al_4SiC_4 heterostructure or quantum well based devices such as HEMTs or LEDs.

1.4 Aim and Objectives of the PhD Thesis

This thesis focus is aimed at the characterization of a novel WBG semiconductor, Al_4SiC_4, which has refectory properties as detailed in the literature review in Chapter 2. The refectory properties and WBG of Al_4SiC_4 are of interest to the electronics industry.

However, many of its properties, such as electronic and opto-electronic, are yet to be characterised. In this work, we will focus only on the electron transport material properties because of their primary relevance to the operation and the performance of power and opto-electronic devices. The hole transport properties are not studied in this thesis because material characteristics of holes in Al_4SiC_4 with respect to the hole effective masses, valley minima, and scattering mechanisms are even less known that those of electrons in Al_4SiC_4. Therefore, in this thesis, we will be looking at the opto-electronic and electronic properties of Al_4SiC_4 (thermal conductivity will not be addressed as this is beyond the scope of the thesis) in order to fill a gap in current literature through three main research methods:

1.4.1 Ensemble Monte Carlo Simulations

The Monte Carlo (MC) simulations aim to provide an insight into the electronic properties of Al_4SiC_4 through computationally simulating the mobility of electrons though the material. This simulations use known parameters taken from current literature such as phonon energy, band gap, lattice constant, acoustic velocity (full list of parameters can be found in Section 4.1.1). Where parameters are unknown, 4H-SiC has been chosen as a material to take parameters from assuming that SiC material properties are close to material properties of Al_4SiC_4. The unknown parameters which will be looked at experimentally will be then used in the MC simulations in order to provide as accurate simulations as possible.

1.4.2 Technology Computer Aided Design Device Simulations

Commercial Technology Computer Aided Design (TCAD) device simulation tool Atlas will be used within a software package by Silvaco [40]. A heterostructure transistor designed using the novel ternary carbide in combination with established SiC is simulated to predict device characteristics such as DC current–voltage (I-V) characteristics, transconductance, and device breakdown voltage. The heterostructure transistor based on the Al_4SiC_4/SiC material system is also scaled down laterally and the performance of the scaled devices compared. Similar to the MC simulations, material parameters for the device simulations are taken from literature, experimental measurements, or from 4H-SiC where parameters are unknown.

1.4.3 Experimental Methods

The UV/Vis/NIR spectroscopy is performed in order to ascertain the bandgap of Al_4SiC_4 as it can directly link the transmission of light to photon absorption and plotted to form a Tauc plot which allows to extract the bandgap. A bandgap of approximately 2.5 eV is expected through this work based upon the literature in Chapter 2. Once determined, the bandgap will be used in the MC simulations in order to keep parameters as accurate as we can. The X-ray Photoelectron Spectroscopy (XPS) is also performed on samples of Al_4SiC_4. We look at the workfunction of the material, valence band position, and the structural make-up of the Al_4SiC_4 material. The final experiments performed on samples of Al_4SiC_4 is two-probe DC current voltage measurements. The two-probe current voltage measurements will determine such material characteristics as the resistivity, Hall coefficient, doping type, sheet carrier density, and electron mobility of Al_4SiC_4 by use of the Van der Pauw method.

1.5 Layout of the PhD Thesis

The subsequent six chapters of this thesis contain the following:

Chapter 2: Gives current knowledge of Al_4SiC_4 is over-viewed to form a literature review detailing both computational works and experimental works in the characterisation of Al_4SiC_4. In this chapter it details works that have been undertaken since 1961 [41] when Barczak first investigated sublimation grown samples of Al_4SiC_4, reported on the optical and X-ray powder diffraction properties. This chapter also provides details of the known material properties of Al_4SiC_4 and compared them to other well-known semiconductors. The band structure of Al_4SiC_4 is also detailed in this chapter and comments on the valleys that are of most interest to this thesis. Finally this Chapter comments on the phonon vibrational works that have been carried out by Zevgitis et al. [42] and Pedesseau et al [43] and comments on how these could potentially impact the electron transport properties of Al_4SiC_4.

Chapter 3: Details background information that was required for the work in this thesis. The bulk of this chapter is given to describing the computational structure of the MC method and how we implemented it as an embedded MC simulator. Within this it details; free flight generation, final state after scattering, the ensemble MC simulator, Fermi's Golden Rule and various scattering mechanisms. This chapter also gives details on the dispersion relationship which was used to calculate the electron effective mass for use in the MC simulator. Furthermore, this chapter gives background

details on the experimental works that were carried as part of this thesis. It started off by giving information for the UV, IR, Vis Spectroscopy, whereby the Beer-Lamberts Law was detailed followed by aspects of light absorption in semiconductors and band tailing. This is followed by details on the photoelectric effect and X-ray Photons for X-ray Photoelectron Spectroscopy. The last experiments detailed in this chapter are two- and four-probe I-V characteristic measurements. Here background information to the four-probe method is detailed in relation to Van der Pauw's approach and hall effect measurements. The last section of this chapter gives background details on the device modelling through Silvaco [40], where information on the transport models used in the simulation of carrier transport in a semiconductor device is given. Also given is details of field-dependent mobility model, Shockley-Read-Hall and Auger recombination, Poisson's Equation, continuity equation and finally the drift-diffusion transport.

Chapter 4: Provides information into the methodology of the research that was undertaken as part of this thesis. The first section of this chapter gives details on the ensemble MC simulator whereby it shows the two valleys of interest to this work. Following this in the section are details of a wave-vector transformation between the three M valleys, where an angular distance between the valleys is introduced. The parameters used in the MC simulator are also tabulated in this section. The second section in this chapter gives details on all the experimental research that were carried out. It first details how the spectrophotometry works by shining light over the range of 175-3300 nm of which only a range of 250-1000 nm was used for the experiment. It also details the geometric set up of the spectroscopy chamber. The experimental methodology then looks at X-Ray Photoelectron Spectroscopy (XPS)whereby monochromatic light illuminates the sample in order to ascertain details of the chemical makeup, valance band, bonds and workfunction. The final experimental setup that is detailed in this section is two- and four-probe measurements, that being a technique used to measure the I-V characteristics by passing voltage through two probes and either measuring the current on the same probes or two different probes. The final section of the methodology details the Technology Computer Aided Design (TCAD) work that is undertaken on a SiC/Al_4SiC_4 heterostructure device, here a Device CAD program called Silvaco Atlas [40] was used. This section details the process that the simulation takes along with the specific structure, mesh design and material models used in the program.

Chapter 5: The first half of this chapter details the results from ensemble MC simulations, the modification into the MC simulations to account for band structure and the material properties of Al_4SiC_4 that were used are tabulated. The second half

of this chapter details the results from the Silvaco Atlas [40] device simulations of a SiC/Al_4SiC_4 heterostructure device, along with providing details on the various device structures that were tested. A discussion on the results from both computational works is detailed at the end of the chapter.

Chapter 6: Details the experimental results that have been carried on both solution grown crystals [42] of Al_4SiC_4 and sublimation grown crystals [44] of Al_4SiC_4. First the bandgap results from the UV/Vis/NIR spectroscopy are detailed followed by XPS results on the composition, valance band, workfunction and depth profiling. The last section of this chapter details the results for the two- and four-probe I-V characteristic measurements. A discussion on all the results is from the three experiments is given at the end of the chapter.

Chapter 7: Summaries the work of this thesis starting with the computational works of which is split into two different areas: (1) bulk electrical properties of Al_4SiC_4 simulated based on an ensemble Monte Carlo code; and (2) device modelling based on a SiC/Al_4SiC_4 heterostructure transistor modelled through Silvaco Atlas [40]. It then goes on to summaries the experimental approach of which is split into three experiments: (1) UV/Vis/NIR Spectroscopy looked at defining the bandgap of Al_4SiC_4, (2) XPS looked at the workfunction, a position of the valence band and the overall composition of Al_4SiC_4, and (3) two- and four-probe DC current voltage characteristics which looked the resistivity of Al_4SiC_4. The final section of this chapter gives an overall conclusion based upon the results that have been collected in this thesis and concludes with the author opinion on Al_4SiC_4.

Chapter 2

Aluminum Silicon Carbide

Aluminum silicon carbide (Al_4SiC_4) has undergone a little investigation since it was first studied in a paper in 1961 [41] which looked at optical and X-ray powder diffraction. The primary interest of Al_4SiC_4 to date has been in the refractory and high temperature corrosion [45–47]. Although this is of interest, especially, for use in harsh environments, the electrical properties of Al_4SiC_4 are of most interest to the work being carried out in this thesis. Over the past half century, Al_4SiC_4 has been classified as a ceramic material with only the past decade or so having a shift towards an electronic classification. In this chapter, we are looking into how Al_4SiC_4 was characterized in the past, utilising the obtained experimental and theoretical data into both our computational work and device modeling. We also look at how Al_4SiC_4 has been characterized as a semiconductor material rather than a ceramic material.

2.1 History of Calculations of Material Properties

In 1995, Grobner et al. [48] optimized the thermodynamic modeling of Al-Si-C ternary systems to produce phase diagrams of the systems. They modelled both Gibbs energies along with a five binary parameter model. In their work, they have used experimental data both in their model and as a comparison to the outcome of their model.

Computational research into the characteristics of Al_4SiC_4 started around 2006 when T. Liao et al. [49] looked at the structural and mechanical properties giving details on the stress and strain, elastic stiffness, bonding strengths under various hydrostatic

pressures, and atomic deformation. The work used a combination of the first-principle pseudo-potential total energy method, generalized gradient approximation (GGA), plane-wave pseudo-potential total energy, Vanderbilt-type ultra-soft pseudo-potential and the Monkhorst pack method. As any many body system, the calculations of material properties of Al_4SiC_4 requires ab-initio methods such as density functional theory (DFT) in order to predict electrical or optical properties.

It was not until Hussain et al. [50] in 2008 who first investigated the electronic structure of Al_4SiC_4 through ab-initio calculations to give the first predictions for the band gap based upon the local density approximation (LDA). The LDA predicted Al_4SiC_4 to have a indirect band gap of 1.05 eV. However, LDA is known to underestimate band gap [51]. The shortcomings of LDA can be greatly improved with the addition of extra terms such as the use of a Hubbard term or by combining the method with other approximations such as the self-consistent many-body (scGW) model.

In 2015, computational modeling of the electronic structure of Al_4SiC_4 was improved by Pedesseau et al. [52] with the implementation of a DFT and scGW model. The calculations confirmed Hussain et al. [50] results for Al_4SiC_4, that the first band is an indirect band. However, the calculations predict a higher energy gap for the first band of 2.5 eV. Pedesseau et al. [52] also predicts a second direct band at 3.2 eV and reveals that the carbon atom plays an important role in the crystal structure, whereby it connects the distorted silicon and aluminum atoms. Lastly, this paper reports on the piezoelectric constants for the first time.

Most recently in 2016, two publications into the computational study of Al_4SiC_4 with publications by Li et al. [53] and Sun et al. [54] occurred. Using first principle DFT calculations, Sun et al. [54] investigated and reported on the structural stability, bonding characteristics, and anisotropic mechanical and thermal properties of Al_4SiC_4. The bulk modulus was reported as 171.9 GPa leading in a prediction that high temperature and high pressure would be needed in order to produce Al_4SiC_4. Li et al. [53] used a hybrid density function HSE06 to study the polarized optical dielectric functions of Al_4SiC_4 in multiple crystal orientations to report on the longitudinal-optical–transverse-optical (LO-TO) phonon splitting, the Born effective charges, and phonon eigen-vectors for all IR-active modes. The work reported that the Al-C bonding is mainly ionic while the S-C bonding is covalent in Al_4SiC_4 along with the LO-TO splitting resulting in large mode-effective charge vectors and mode-dissociated static dielectric constants. Finally, they reported that the IR response of phonon modes is strongly dependent on crystallographic direction, whereby they looked at the [010] and [001] directions.

2.2 History of Experimental Measurements

Experimental research into Al_4SiC_4 has been going on since it was first report in 1961 by Barczak [41] who look at optical and X-ray power diffraction data on Al_4SiC_4 that was grown via sublimation of Al_4C_3 and SiC in a vacuum furnace. They noted two phases of Al_4SiC_4, α and β, a yellow colour of their samples and a hexagonal lattice for α-Al_4SiC_4 with lattice parameter $c = 10.80$ a.u.

In 1979, Schneider et al. [55] found the compound Al_4SiC_4 while looking at the binary system SiC-Al_4C_3. Schneider [55] compared their findings with the only other report of Al_4SiC_4, that being Barczak [41]. They found differences in the lattice parameters giving $a = 0.3281$ nm and $c = 2.167$ nm, compared with $c = 0.5715$ nm that Barczak [41] found. Schneider et al. also found discrepancies with the X-ray measurements of Barczak [41] where an additional fourteen reflections due to d spacing were observed between 0.13 nm and 0.15 nm.

The following year (1980), Inque et al. [56] reported on a new phase of aluminum silicon carbide, that being $Al_4Si_2C_5$ along with further data on α-Al_4SiC_4. Inque et al. [56] synthesised α-Al_4SiC_4 by melting powered silicon carbide with Al_4C_3 before being headed up to $2000°C$ before being cooled. The lattice parameters of the Al_4SiC_4 crystals were measured and found to be in agreement with Schneider et al. [55]. Inque at al. [56] postulated on the space groups for Al_4SiC_4 with the possibilities of it being either P63 mc or P63/mmc, where X-ray diffraction data confirmed the space group as P63 mc.

Several years later, a paper by Schoennahl et al. [57] in 1983 gave an account of a method of preparation for Al_4SiC_4 along with crystallographic information on the structure of Al_4SiC_4 detailing the lattice parameters: $a = 0.328$ nm and $c = 2.172$ nm as well as confirming a hexagonal lattice for the material. The paper went on to give a detailed description of α-Al_4SiC_4 but no description of a β phase of Al_4SiC_4. Finally, they noted the possible existence of a family of compounds with the formula $Al_4C_3(SiC)_n$.

Three papers came out the following year (1984), one by Beyer et al. [58] and the other by Behrens et al. [59] and a final one by Kidwell et al. [60]. Beyer et al. [58] looked at the head capacity of Al_4SiC_4 over a range of temperature from 5.26 to 1047 K. They synthesized Al_4SiC_4 from powers of Al_4C_3 and SiC. What they found was that the standard molar enthalpy of formation is 203.3 ± 4.9 kJ mol^{-1} at 298.15 K. Behrens et al. [59] looked at the vaporization thermodynamics and enthalpy of the formation of Al_4SiC_4. Al(g) was the only vapor present in the equilibrium vapor of (Al_4SiC_4 + SiC + C) up to 1784 K. Ref. [59] found a formation of a micro-layer on the Al_4SiC_4 of (SiC + C)

and that the enthalpy formation for Al_4SiP_4 being -187 ± 34 kJ mo^{-1} at 298.15 K which is similar to that of Beyer et al. [58]. Kidwell et al. [60] presented a short communication into a new intermediate phase in the Al-SiC system. Several ternary phases were looked at during this work where they show the existence of Al_4C_3-SiC and a new ternary intermediate phase $2Al_4C_3$-SiC. However, they could not confirm the previously reported existence of Al_4C_4-SiC.

Later in the 80's, Yamaguchi et al. [45] (1987) looked at the synthesis and some properties of Al_4SiC_4. The paper noted that the addition of Al_2O_3 during synthesis helps to facilitate the formation of Al_4SiC_4. The paper looks at two main properties of Al_4SiC_4, the hydration resistance and oxidation resistance. The hydration resistance was found to admirable and sufficient for practical use and oxidation resistance was shown to be good up until 750°C where it started to oxidize as the temperature increased. The same year, the alloying of aluminum, silicon, and carbon was studied by Oden et al. [61]. Here, they used various methods to determine the isopleth of Al_4C_3-SiC at 2000°C and 2150°C. They also report on the solubility of carbon in aluminum and silicon at high temperature as well at the decomposition temperatures for Al_4C_3 among other Al-Si-C systems.

Oden et al. carried on the research on Al-Si-C systems and Al-C-N systems and published further works in 1990 [62]. The refractory nature of aluminum silicon carbonitrides was confirmed and the decomposition temperature for the two systems was measured to be 2265°C for Al_4C_3-AlN-SiC phases. One thing that restricted practical information was the formation of liquid phases on the AlN side at 2175°C and on the SiC side at 2070°C. This work also looked to the isothermal sections and, at 1860°C, indicated a pseudo-binary compound, Al_3C_3-AlN, in the Al_4C_3-Al_n subsystem along with two compounds $2Al_4C_3$-SiC and Al_4C_3-SiC in the Al_4C_3-SiC system and, finally, AlC_3-AlN and Al_4C_3-AlN-SiC in the Al_4C_3-AlN-SiC system.

Almost ten year later, in 1996, Grobner et al. [48] looked at the phase diagram of Al-Si-C systems optimizing it using past experimental data [63–71]. Grobner et al. [48] also gave an account of previous investigations from Barczak et al. [41] through to Oden et al. [62]. The optimized calculation of the phase diagram found small deviations which was put down to incompatibility between established solubilities in the binary subsystems and measured solubilities in the ternary system.

In 2002, Yamamoto et al. [46] looked at synthesizing Al_4SiC_4 from a powder mixture of aluminum, silicon and carbon black. It was noted that a small amount of triethanolamine (TEA) was needed in order to form Al_4SiC_4 as without TEA the mixture seem to form Al_4C_3 and SiC instead. The paper discusses the oxidation resistance of Al_4SiC_4 at various

temperatures up to 1450°C. Yamamoto et al. [46] found that Al_4SiC_4 has superior oxidation resistance below a temperature of 850°C. The same year, Inoue [47] also looked at the fabrication and oxidation resistance of Al_4SiC_4. Syntheses of Al_4SiC_4 was done by mixing powders of aluminum, silicon and carbon together before sintering by pulse electronic current. The work also reported on oxide grow at high temperature of 1250°C-1500°C and showed that the oxide layer grows exponentially as the temperature increases.

The following year (2003), Inoue et al. [72] looked at the electrical resistivity of Al_4SiC_4 sintered bodies at various temperatures. Inoue et al. [72] found that the material gave slightly insulating electrical properties. They also showed that the current-voltage characteristics followed a linear relationship and have an ohmic region. The same year, Inoue et al. [73] carried out further studies into the synthesis of Al_4SiC_4. They synthesized Al_4SiC_4 with a powdered mixture of aluminum, silicon and carbon together as well as amounts of kaolin powder. They discussed the various intermediate stages for synthesizing Al_4SiC_4 as well as the Gibbs energy of formation, which changes from positive to negative at a temperature of 1106°C.

Further works into the synthesis and the oxidation behavior were reported on by Wen et al. [74] in 2005. The process for synthesis that Wen et al. [74] used was by hot pressing aluminum, graphite powers and polycarbosilane (PCS). They report that the use of PCS helps promote the formation of Al_4SiC_4 and its densification into one event, rather than having intermediate stages. Further works were carried out by Wen et al. [74] on Al_4SiC_4 giving the first accounts into the mechanical and thermal properties. The same year came first reports of the compression and pressure behavior of Al_4SiC_4 by Solozhenko et al. [75]. The quasi-hydro-static compression of Al_4SiC_4 was studied up to a pressure of 6 GPa at room temperature. Through their work they were able to determine a bulk modulus, B0, of 182(10) GPa and an anisotropic nature of compression.

2007 came with further works into the synthesis of Al_4SiC_4, where Zhao et al. [76] studied the various factors that influenced the synthesis. The methods that were studied included heating mixtures of Al_20_3, $Si0_2$ and graphite in an argon atmosphere. Zhao et al. [76] noted that the optimum molar ratio of carbon, Al_20_3 and $Si0_2$ was 8:2:0.8, where by pure Al_4SiC_4 was formed. Within the works they also give a discussion about the formation mechanism of Al_4SiC_4.

Several years later, in 2010, Deng et al. [77] produced further information into the synthesis of Al_4SiC_4 and Al_40_4C. This work introduced the idea of using an Fe_20_3 additive in the synthesis process along with flint clay, activated carbon and aluminum

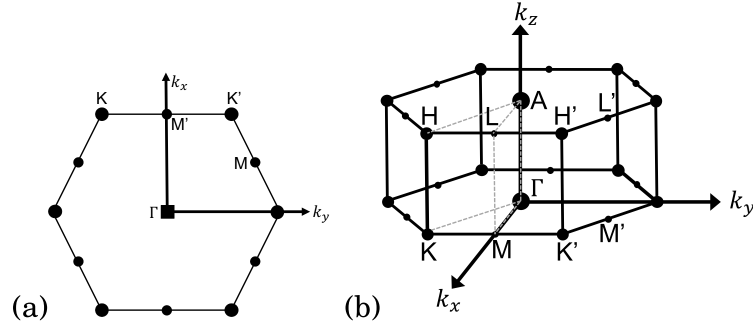

FIGURE 2.1: (a) 2D hexagonal (0001) plane showing the location of the M valleys within the Al_4SiC_4 hexagonal structure and (b) a 3D hexagonal structure showing locations of principal valleys.

powders. They report that the use of an Fe_20_3 additive promotes the nucleation and grain refinement of Al_4SiC_4 phase and leads to Fe_3Si coating Al_4SiC_4 grains. This giving way to fine granules structure instead of fibrous-like structures.

Come 2015, Zevgitis et al. [42] look at characterizing Al_4SiC_4 and compared it with Al_4C_3 [78]. Here they presented results from synthesising material by cooling an aluminium-silicon melt in a graphite crucible. Raman spectroscopy was used to determine the vibrational modes, where 18 Raman lines in the 80-920 cm^{-1} were found in Al_4SiC_4 which fell short of the 25 that were predicted hexagonal $P6_3mc$ structure. UV-Vis-NIR spectroscopy was also performed on samples of Al_4SiC_4 to determine the band gap which presents itself around 2-2.5 eV. The crystal structure was confirmed in this paper by both XRD and TEM and was in agreement with past examinations of Al_4SiC_4 showing the same hexagonal structure, an orange coloured crystal and a crystal orientation of $P6_3mc$.

2.3 Material Properties

Al_4SiC_4 belongs to a family of aluminium-silicon ternary carbides with the general formula $(Al_4C_3)_x(SiC)_y$ (x, y = 1 or 2) and exhibit a hexagonal structure, see Figure 2.1. Al_4SiC_4 in particular is a stacked unit of two-unit cells, that being Al_4C_3 and SiC, see Figure 2.2. It has a group spacing of P63mc [50, 52, 56, 61] with lattice parameters $a = b = 3.2812$ Å [52] and $c = 21.7042$ Å [52] and a mass density of 3.03 g/cm^3 [52]. Other parameters that are of use to this work are listed in a comparison of Al_4SiC_4 to other semiconductor material parameters like the piezoelectric constant, acoustic deformation potential, and the longitudinal and transverse acoustic velocities in Table 2.1.

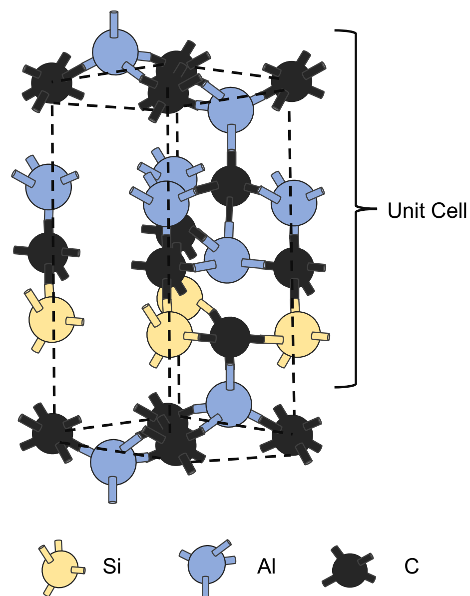

FIGURE 2.2. Crystal structures of Al_4SiC_4. The blue, yellow, and black spheres represent Al, Si, and C atoms, respectively.

Parameter	Si [79]	SiC [80] (3C / 4H / 6H)	GaN [80] (Wurtzite)	AlN [80]	Al_4SiC_4
Mass Density (g/cm^3)	2.32	3.21 / 3.211 / 3.21	6.15	3.23	3.03 [52]
Lattice Constant (Å)	5.43	4.36 / 3.07 / 3.07	3.16	3.11	3.28 [52]
Longitudinal Acoustic Velocity ($\times 10^5 cm/s$)	2.32	9.50 / 12.50 / 12.50	7.96	10.97	10.577 [54]
Transverse Acoustic Velocity ($\times 10^5 cm/s$)	5.34	4.10 / 7.10 / 7.10	4.13	6.22	6.431 [54]
Electron Effective Mass	0.916 m_0 0.190 m_0	0.68 m_0 / 0.29 m_0 / 0.20 m_0 0.25 m_0 / 0.42 m_0 / 0.42 m_0	0.20 m_0	0.4m_0	M_{long} 0.5678m_0 $^{(a)}$ M_{trans} 0.6952m_0 $^{(a)}$ K_{long} 1.0569m_0 $^{(a)}$ K_{trans} 0.9360m_0 $^{(a)}$
Optical Phonon Energies (meV)	63.00	102.80 / 104.20 / 104.20	91.2, 40.00	99.2	80.59 $^{(b)}$, 86.79 $^{(b)}$
Band Gap (eV) Direct(D)/Indirect(I)	1.12 I	2.40 – I / 3.26 – I / 3.02 – I	3.40 – D	Eg_1 = 6.2 Γ_1 Valley – D Eg_2 = 6.9 M-L Valley – I Eg_3 = 7.2 K Valley – I	Eg_1 = 2.78 M Valley – I $^{(c)}$ Eg_2 = 3.30 K Valley – D [52]
Acoustic Deformation Potential (eV)	9.0	12.6 / 11.6 / 11.2	8.16	9.5 [81]	11.4 $^{(d)}$
Static Dielectric Constant	11.7	9.72 [82] / 9.66 $^{(e)}$ / 9.66 [82]	8.43 [83]	6.99 [83]	8.32 [53]

TABLE 2.1. A comparison of Al_4SiC_4 to other semiconductor material parameters. References for the parameters are listed in the top of the column unless otherwise stated, (a) calculated values based on the DFT data that was received from L. Pedesseau [52], (b) calculated values based on the Raman and IR experiments at LMGP/Grenoble INP [43], (c) values calculated in this work, (d) average taken from Ref [84], (e) no published data for 4H-SiC, but the dielectric constant for 6H-SiC is often used instead.

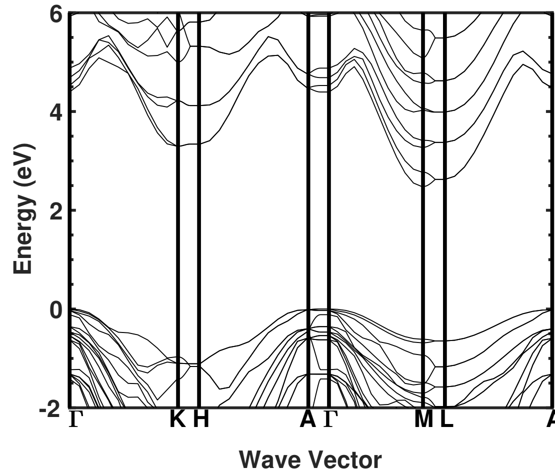

FIGURE 2.3. Re-scaled Al_4SiC_4 bandstructure obtained from Pedesseau et al. [52] density functional theory (DFT) calculations.

From the hexagonal crystal structure, Figure 2.1, and the band diagram, Figure 2.3, we have determined the following valleys: Γ, A, L, H, M and K. Not all of these valleys are of importance to the electronic properties. Only two lowest energy bands, the M and K valleys, that is Γ-to-M and Γ-to-K regions of the **k**-space, are considered as representation of the electron band structure of Al_4SiC_4 in our bulk Monte Carlo simulations. Further details on this band structure model can be found in Section 5.1.

A band gap of Al_4SiC_4 has been predicted in several computational studies starting with Hussain et al. [50] in 2008 at a value of 1.05 eV and the most recently in 2015 at 2.48 eV [52]. The comparison of various band gaps have been detailed in Table 2.2. The band gap from the computational works which use density functional theory (DFT)

Published Band Gap (eV)	Method
1.05	Computational (DFT)[50]
1.12	Computational (DFT)[54]
1.81	Computational (DFT)[53]
2-2.5	Experiment (UV-Vis-NIR)[42]
2.48	Computational (DFT) Experimentally (Ellipsomoetry)[52]
2.4-2.5	Experiment (UV-Vis-NIR and Ellipsomoetry)[43]

TABLE 2.2. Comparison of published energy band gaps for Al_4SiC_4 indicating a method and a source.

calculations [85] are well known to underestimate the real band gap of wide band gap materials [51] (because of principal difficulty to account for exchange and correlation effects in electron many body system), but refinements over the years have greatly improved the DFT models in order to predict more accurately the band gap of a material by including good approximations of the exchange and correlation effects. The variance in the band gap in experimental works has mainly come from difficulties to identify the absorption edge in a measured optical spectrum. The band gap will be investigated further in this thesis so that we will to pin point it more accurately.

The works on phonon vibration modes by Zevgitis et al. [42] and Pedesseau et al. [43] performed Raman spectroscopy measurements on Al_4SiC_4 single crystal platelets at different polarized configurations (laser propagation parallel to the c-axis and orthogonal to the c-axis), see Figures 2.4 and 2.5. The phonon vibration modes that are detailed in these figures are polar and non-polar optical phonons as described in Section 3.3.6 (3) and (4), Chapter 3, respectively. These vibration modes of phonons are important when calculating the electronic transport properties as they determine the electron interactions with phonons. The electronic properties and lattice properties of solid state material are closely related due to electron-phonon interaction [86] and both absorption and emission of phonon energy are possible. The kinetic energy of the electrons decrease by emitting of phonons or increase by absorption of phonons. Typically, at room temperature (approximately $300°C$), the kinetic energy of electrons is above the thermal energy of phonons and the probability of phonon emission is larger than the probability of phonon absorption. Unfortunately, there is no current literature that investigates phonon spectrum in Al_4SiC_4 and, therefore, it is still unknown as to what effect these vibrational modes of phonons have on the transport of carriers.

2.4 Summary

In this chapter, we have seen various material properties of Al_4SiC_4 come to light since it was first analysed in 1961 [41] by the X-ray power diffraction. Al_4SiC_4 was first characterised as a ceramic material until Hussain et al. [50] in 2008 when they undertook the first investigation into its electrical properties. This led way to Al_4SiC_4 being characterised as a semiconductor material with a band gap of 1.05 eV. However, at this stage, the computational work done on Al_4SiC_4 underestimated its band gap due to the LDA (Local Density Approximation) model that was being used. It was not until 2015 when two research groups [42, 52] reclassified Al_4SiC_4 as a WBG semiconductor with

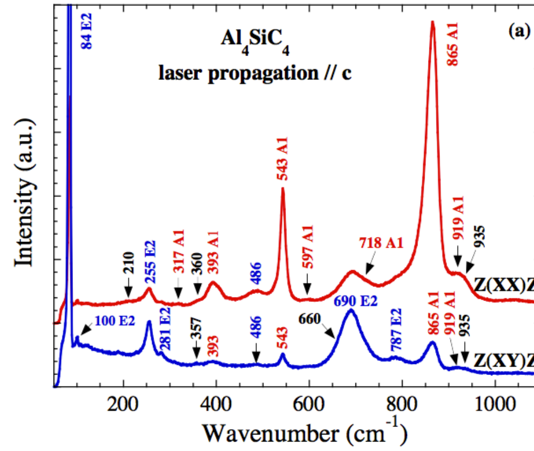

FIGURE 2.4. Polarized Raman spectra of Al_4SiC_4 single crystals. Spectra collected on the crystal surface (laser propagation along the c-axis). Image taken from [43].

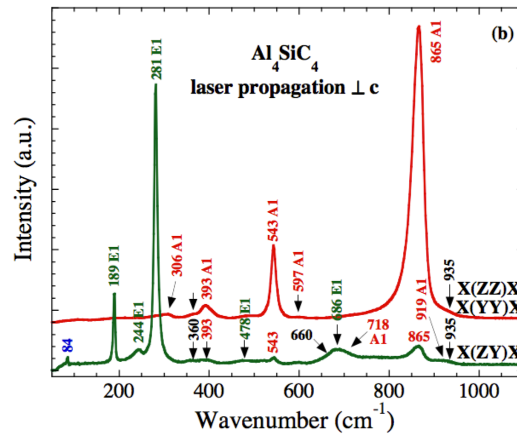

FIGURE 2.5. Polarized Raman spectra of Al_4SiC_4 single crystals. Spectra collected on the crystal edge (laser propagation parallel to the crystal surface). Image taken from [43].

a larger band gap of between 2.0 eV-2.5 eV. Other material properties of Al_4SiC_4 have also been investigated over the years including the structural and mechanical properties [49], structural stability, bonding characteristics, anisotropic mechanical and thermal properties [54], polarized optical dielectric function [53], method of preparation [57], synthesis [45, 46, 56, 74, 76, 77], lattice spacing [50, 52, 56, 61], space group [42, 56], refractory nature [45, 46, 62, 74], resistivity of Al_4SiC_4 sintered bodies [72], and vibrational

modes [42].

Chapter 3

Theoretical Background

This chapter gives background details on the methods used in this thesis. There are details on solid state physics, ensemble Monte Carlo (MC) technique employed to simulate transport properties of the bulk aluminium silicon carbide, device simulations and experiments. The main emphasis of this chapter is to give a theoretical background to the physical approaches and experimental techniques that make up the work in this thesis, from the approximation of effective carrier mass to describe a band structure of a semiconductor considering its relevance to the carrier transport, through carrier free flights assuming Newton mechanics and quantum-mechanical scattering, to Poisson's equation to self-consistently account for long-range electron-electron interactions (Coulomb scattering).

3.1 Effective Mass

When electrons and holes have a relatively small energy, they behave as free particles where their effective mass and energy dispersion follows a parabolic dispersion law. This law represents the $E-\mathbf{k}$ dispersion relation, that is, the relationship between the electron energy, E, and the crystal momentum or wave-vector, $\mathbf{k}$. When $\mathbf{k}=0$, the band minima, the energy dispersion takes on the form [87]:

$$E(\mathbf{k}) = \frac{p^2}{2m} = \frac{\hbar^2 k^2}{2m^*} = \frac{\hbar^2}{2m^*}(k_x^2 + k_y^2 + k_z^2) \tag{3.1}$$

where $E(\mathbf{k})$ represents the kinetic energy of electron when measured from the band minima, m is the mass of an electron, m^* is the effective mass, x, y and z refer to the axis and are aligned to the principal axes of the ellipsoids, p is the momentum and $\hbar$ is Plank's constant divided by 2π.

We can write Equation (3.1) for the effective mass, m^*, by differentiating E twice with respect to $\mathbf{k}$, leading way to:

$$\frac{1}{m*} = \frac{1}{\hbar^2}\frac{\partial^2 E(\mathbf{k})}{\partial k^2} \tag{3.2}$$

We can use this dispersion relation to calculate the effective mass from the band structure. As the conduction band has a zero slope at its minima, the dispersion is taken as a quadratic, as illustrated in Figure 3.1, and is fitted with a polynomial trend-line with the form:

$$y = a + b\,x + c\,x^2 \tag{3.3}$$

where a, b and c are constants and y and x refer to the axis.

The second order derivative of the parabolic equation can be related to the energy dispersion relation as follows:

$$2\,c = \frac{\partial^2 E(\mathbf{k})}{\partial k^2} \tag{3.4}$$

where c is a constant. This equation is used to determine the effective electron mass in both the longitudinal and transverse direction of Al_4SiC_4 so that we could use them as a material parameter in the MC simulations (see Chapter 5.1).

3.2 Boltzmann Transport Equation

The Boltzmann Transport Equation (BTE) is a statistical physical model describing carrier transport in semiconductors over time, both in real space and momentum space. A distribution of electrons can be described using the distribution function, $f(\mathbf{k}, v, \mathrm{t})$, for an individual electron with velocity, v, moving under an external force $\mathbf{F}$, such as a magnetic force. The BTE is given by [88]:

$$\frac{\partial f}{\partial t} = -(v \cdot \Delta_{\mathbf{r}} f + \mathbf{F} \cdot \Delta_{\mathbf{k}} f) + \left(\frac{\partial f}{\partial t}\right)_{collision} \tag{3.5}$$

where f is the distribution function and t is the time variable, the subscript $collision$ denotes the collision term and, $\Delta_{\mathbf{r}}$ and $\Delta_{\mathbf{k}}$ are the differential operators in terms of the position and momentum vectors, respectively.

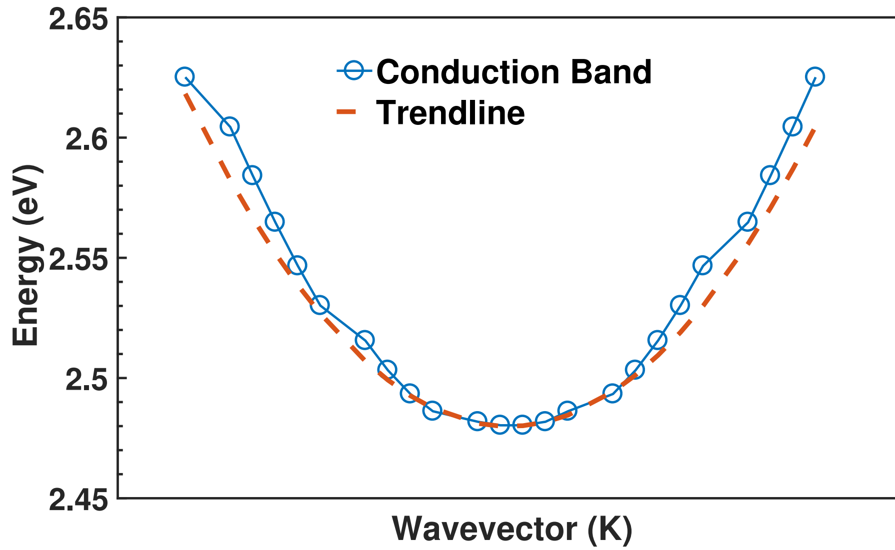

FIGURE 3.1. Generalized idea of the dispersion relation in a conduction band fitted with a polynomial trendline.

BTE (3.5) describes transport evolution of particles due to particle collisions (scattering) and their drift due to an applied external field in real and reciprocal space in time. In other words, the BTE describes the evolution of the distribution of particles through the motion of the particles, the force acting on them, and their scattering due to collisions. The BTE is an integral-differential time-dependent kinetic equation of motion over six-dimensional position-momentum space, and finding an analytically solution is extremely difficult [89]. Prior knowledge is usually needed in order to solve the BTE analytically which sometime is not known [90, 91]. Therefore, it is usually solved numerically through such methods as a MC technique to simulate the electron transport through a may-body system [92, 93]. Details on a specific MC technique, the ensemble MC technique, which simulates a transport of carriers in condensed matter, gas or plasma, can be found in Section 3.3.

3.3 Bulk Ensemble Monte Carlo Simulations

The behaviour of any semiconductor device such as a bipolar junction transistor (BJT) and field effect transistor (FET) can be adequately described by a semi-classical model of charge transport within device domain. This is due to the fact that the characteristic dimensions in question are typically of length scales much larger than those

where quantum-mechanical phase coherence is maintained. At these length scales, a particle-based description based on the BTE framework and its approximations can be used. However, as devices continue to shrink, their channel length are approaching the characteristic wavelength of particles, the so-called de Broglie wavelength, and the quantum-mechanical effects are expected to become increasingly important. For example, a quantum-mechanical confinement affects distribution of electrons and holes in the inversion layer of FETs. However, at room temperature and under strong electric fields, such effects are usually found to be of the second order in the overall behaviour of the device. This is not to say that as spatial dimensions reduce that the consideration of quantum effects will not take precedence over other effects.

When the BTE is applied to give a classical description of charge transport in semiconductors, a probability distribution function is assumed for particles which develops in real and momentum space in time. This probability distribution function, given by $f(\mathbf{k}, v, t)$, describes movement of charged carriers in a six-dimensional phase space of a real position and crystal momentum in time. When this probability distribution function is known, any physical observable of carriers or a system such as velocity, momentum, energy, charge or current can be monitored or calculated based on the averages of f (see Section 3.2 for further details on the BTE). An expansion of the BTE over a momentum space reveals a set of approximate partial differential equations in position space, leading way to the hydrodynamic model for charge transport. A simplification of the hydrodynamic model, where the continuity equation (Section 3.10.5) and the current density equation (Section 3.10.6) are written in term of the local electric field and concentration gradients, leads to the drift-diffusion transport model (see Section 3.10.6). This model can be reduced further if needed for the simulation of lumped parameter behaviour at a circuit level where many individual devices as well as passive elements can be simulated.

3.3.1 The Ensemble Monte Carlo Method

The ensemble MC technique [94–97] has been used as a numerical method to simulate non-equilibrium particle transport in many-body systems including semiconductors, both in bulk materials and devices, for several decades now. When the ensemble MC technique is applied to a simulation of carrier non-equilibrium transport in semiconductors, the simulation is semi-classical because the carrier movement between collisions is assumed to be classical govern by Newton equations while the probability of collisions or carrier scatterings is calculated quantum-mechanically. Technically, a random path is generated to simulate the stochastic motion of particles which can be subject to randomly selected

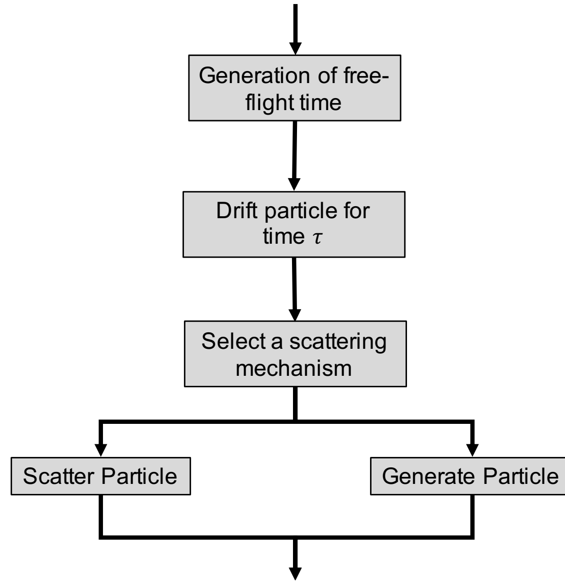

FIGURE 3.2. Evolution of particles in a Monte Carlo simulation.

collision processes. This random path generation evaluates integral equations and is a part of the general random sampling used in the evaluation of multi-dimensional integrals. The technique simulates free flights during a particle motion that gets terminated by instantaneous scattering events occurring with a quantum-mechanical probability. The algorithm for the MC technique consists of the generation of random free flight times for each particle, the generation of a scattering process determined by the quantum-mechanical probability which will occur at the end of the free flight, and the generation of a final energy and a momentum of the particle based on probability related to the scattering. This process is repeated for the next time step as illustrated in Figure 3.2.

The MC method will sample the particles motion at various times throughout the simulation. This will allow for an approximation of physical quantities of interest such as the single particle distribution function, the average drift velocity in an applied electric field, etc. Simulation of an ensemble of particles, which is representative of a physical system of interest, can provide the non-stationary time-dependent evolution of both the electron and hole distributions under the influence of a time-dependent driving force.

3.3.2 Free Flight Generation

The ensemble MC technique models the dynamics of particle motion by assuming that the particle free flights are terminated by instantaneous scattering events, that change

the momentum and energy of the particle. The selection of the time when scattering occurs, the selection of the scattering mechanism, and the selection of a final state after the scattering, as well as many steps in initialisation of a many-body system, is performed using random numbers within physically calculated probability.

In particular, the free flight is simulated with a probability density, $\mathbf{P}(t)$, in which $\mathbf{P}(t)\,dt$ is the joint probability. The probability that a particle will arrive without scattering at time, t, after a previous collision at $t = 0$, and then suffers a collision at the time t is given by:

$$t = \exp\left\{-\int_0^t \Gamma[\mathbf{k}(t')]\,dt'\right\} \tag{3.6}$$

where $\Gamma(\mathbf{k})$ is the total scattering rate given by:

$$\Gamma(\mathbf{k}) = \sum_{j=1}^{N} \Gamma_j(\mathbf{k}) \tag{3.7}$$

where j is the j-th scattering mechanisms and N is the number of all possible scattering mechanisms considered. The joint probability density is then:

$$\mathbf{P}(t) = \Gamma[\mathbf{k}(t)]\exp\left\{-\int_0^t \Gamma[\mathbf{k}(t')]\,dt'\right\} \tag{3.8}$$

where the probability of scattering in the time interval dt around t is $\Gamma[\mathbf{k}(t)dt]$ and $\Gamma[\mathbf{k}(t)]$ is the scattering rate of an electron or a hole with wave-vector $\mathbf{k}$.

The probability density, $\mathbf{P}(t)$, can be related to a uniform random number r by:

$$\mathbf{P}(r)\,dr = \mathbf{P}(t)\,dt \tag{3.9}$$

Integrating this with regards to $\mathbf{P}(r) = 1$ gives:

$$r = \int_0^t \mathbf{P}(t')\,dt' \tag{3.10}$$

Substituting $\mathbf{P}(t)$ from Equation (3.8) and integrating gives:

$$r = 1 - \exp\left\{-\int_0^t \Gamma[\mathbf{k}(t')]\,dt'\right\} \tag{3.11}$$

The relation for the random number r can be simplified because $1-r$ is statistically the same as r, the uniform random number. The fundamental equation, which is needed to generate random free flight time after each scattering event, is then given by:

$$-\ln(r) = -\int_0^t \Gamma[\mathbf{k}(t')]\,dt' \tag{3.12}$$

The overall scattering probability Γ is generally depending on wave-vector $\mathbf{k}$.

The numerical determination of the free flight time, t, from Equation (3.12) is computationally very time consuming. Therefore, a trick is used by introducing a self-scattering mechanism, invented by Rees [98], which leaves the state of an electron unchanged (neither the particle momentum nor energy is changed) in order to have the total scattering rate a constant. The total scattering rate, Γ, will be then given by:

$$\Gamma = \Gamma_0[\mathbf{k}(t')] + \Gamma[\mathbf{k}(t')] \tag{3.13}$$

where Γ_0 is the self-scattering rate chosen to be equal to or larger than the maximum Γ expected in the simulation as [95]:

$$\Gamma_0(\mathbf{k}) = \Gamma - \sum_{j=1}^{N} \Gamma_j(\mathbf{k}) \tag{3.14}$$

where Γ is defined as:

$$\Gamma = \sum_{j=0}^{N} \Gamma_j(\mathbf{k}) \tag{3.15}$$

The free flight time, t, therefore is given by:

$$t = \frac{1}{\Gamma} \ln r \tag{3.16}$$

3.3.3 Final State After Scattering

The final state after scattering is determined by the scattering mechanism that is randomly selected, i.e., electron interaction with acoustic phonons, electron interaction with non-optical phonons, distinguishing emission and absorption processes, etc. This scattering mechanism terminates the free flight and the final energy and momentum of a particle is determined. The total scattering rate, Γ is a sum of the relative total scattering rates from initial particle state $n, \mathbf{k}$ given by:

$$\Gamma = \Gamma_0[n,\mathbf{k}] + \Gamma_1[n,\mathbf{k}] + \Gamma_2[n,\mathbf{k}] + \cdots \Gamma_N[n,\mathbf{k}] \tag{3.17}$$

where Γ_0 is the self-scattering rate, n is the band index of the particle, and $\mathbf{k}$ is the initial wave-vector at termination of free-flight. The scattering mechanism is chosen by generating a uniform random number between 0 and Γ [98]. The relative total scattering rate which depends only on the initial state of carrier, $\Gamma_j[n,\mathbf{k}]$, has to be a sum of the all final states of carrier given by:

$$\Gamma_j[n,\mathbf{k}] = \sum_{m,\mathbf{k}'} \Gamma_j[n,\mathbf{k};m,\mathbf{k}'] \tag{3.18}$$

where the scattering rate $\Gamma_j[n,\mathbf{k};m,\mathbf{k}']$ is for the j-th scattering mechanism, and n and m are the initial and final band indices, and $\mathbf{k}$ and $\mathbf{k}$' are the wave-vectors before and after scattering, respectively.

The final state is very practical to determine in a spherical coordinate system in which the wave-vector $\mathbf{k}$ is described by its absolute value k ($k \equiv |\mathbf{k}'|$) and two angles ϕ and θ. The spherical space for a wave-vector simplifies determination of the final wave-vector $\mathbf{k}'$ because the three components need to specify the final wave-vector: absolute value of k' and two angles: azimuthal ϕ and polar θ, which are between the initial and final wave-vectors, can be calculated from relatively simple mathematical expressions which would be very complex in Cartesian space using the respective wave-vector components of the initial state: k_x, k_y, k_z and the final state: k'_x, k'_y, k'_z. If the scattering mechanism is energy conserving, the final absolute value k' of the wave-vector $\mathbf{k}'$ is simply the initial absolute value k of the wave-vector $\mathbf{k}$. The change of the initial wave-vector $\mathbf{k}$ to the final wave-vector $\mathbf{k}'$ after scattering depends on the angle θ between $\mathbf{k}$ and $\mathbf{k}'$ because of the conservation of energy and momentum [95, 97, 99]. Therefore, ϕ can be chosen using a uniform random number between 0 and 2π, while θ is generated according to the probability of cross-section arising from the scattering rate. If the probability for the scattering into a certain angle, $P(\theta)d\theta$, is integrable, then a random angle satisfying this probability density may be generated from a uniform distribution between 0 and 1 through an inversion expression for the relative total scattering rate (3.18). If not, then a rejection technique may be used to select the random angle according to $P(\theta)$.

3.3.4 Ensemble Monte Carlo Simulation

The above process/algorithm may be used to follow single particle over many scattering events in order to simulate the steady-state behaviour of an uniform system. However, the simulations of the realistic many-body semiconductor system require the use of an ensemble of particles where the above process/algorithm is repeated for each particle within the ensemble system of interest until the simulation is completed. This process happens by simulating a particle until the end of a time-step, Δt, then the next particle in the ensemble is treated. Over each of the time-steps, Δt, the motion of the particle is simulated independently of other particles. The nonlinear effects such as carrier-carrier interactions are updated at the end of each time-step.

The non-stationary many-body distribution function and related quantities, drift velocity, valley population, etc., are taken as averages of the time-step throughout the simulation. For example, the average drift velocity ($\bar{v}$) in the presence of the field given

by an ensemble average of the component of velocity in the direction of the applied field is given at the n-th time-step (Δt) by [100]:

$$\bar{v}(n\Delta t) \cong \frac{1}{N}\sum_{j=1}^{N} v^{j}(n\Delta t) \tag{3.19}$$

where N is the number of simulated particles and j labels each of the particles in the ensemble. The equation thus represents an estimation of the average velocity of particles (electrons or holes), which has a standard error, s, of:

$$s = \frac{\sigma}{\sqrt{N}} \tag{3.20}$$

where σ^2 is the variance which may be estimates from:

$$\sigma^2 = \frac{N}{N-1}\left(\frac{1}{N}\sum_{j=1}^{N}(v^{j})^2 - \bar{v}^2\right) \tag{3.21}$$

A similar distribution function for both electrons and holes may be tabulated by counting the number of electrons in each of the cells defined in **k**-space. The error that is estimated by Equation (3.20) decreased with the squared root of the number of particles in the ensemble. Typical sizes for good statistical ensemble models are in the range of $10^4 - 10^5$ particles, but is not limited to these values. However, there are a variety of techniques to decrease this standard error enhancing statistically rare events such as impact ionization or electron-hole recombination [97].

3.3.5 Fermi's Golden Rule

Fermi's Golden Rule, derived from perturbation theory, is a quantum mechanical equation of the transition rates or carrier scattering process. In what follows, we will focus only on electrons because the equations for holes are identical. The j-th electron scattering rate, Γ_j, of the transition of an electron from an initial state $|\mathbf{k}\rangle$ to a final state $|\mathbf{k}'\rangle$ will occur is given by [88]:

$$\Gamma_j[n,\mathbf{k};m,\mathbf{k}'] = \frac{2\pi}{\hbar}\left|H^{a,e}_{m,\mathbf{k}';n,\mathbf{k}}\right|^2 \delta(E(\mathbf{k}') - E(\mathbf{k}) \mp \hbar\omega) \tag{3.22}$$

which keeps an account of both phonon absorption (a) and phonon emission (e) energies with the $\mp\hbar\omega$. H in Equation (3.22) includes the scattering potential of the interaction, and $E(\mathbf{k}_0')$ and $E(\mathbf{k}_0)$ are the initial and final state energies of the particles. The delta function, δ, is the Kronecker delta and results in the conservation of energy for long

times after the collision. The scattering rate in Equation (3.22) can be transferred to three-dimensional (3D) space by converting it to an integral within a crystal volume, V, if required, giving the final scattering rate as:

$$\Gamma(\mathbf{k}) = \frac{V}{(2\pi)^3}\frac{2\pi}{\hbar}\int \left|H^{a,e}_{m,\mathbf{k}'_0;n,\mathbf{k}_0}\right|^2 \delta(E_{\mathbf{k}'_0} - E_{\mathbf{k}_0} \mp \hbar\omega)\delta_{\mathbf{k}'-\mathbf{k}\mp q,0}\, d\mathbf{k} \tag{3.23}$$

The assumption here is that any collision occurs instantaneously and has permanent effects, that is, until another collision occurs. This is due to the amount of time of each collision being much smaller than the time between collisions. This condition is satisfied in nanoscale semiconductor devices operating at sub-terahertz frequencies as many semiconductor transistor for digital and analogue applications [101, 102]. The typical electron scattering time at room temperature is in the range of picoseconds ($10^{-12}s$) to which only terahertz frequencies are comparable. Naturally, this assumption will not be valid at a very low temperature, for example, close to helium temperatures. When we sum up over all final states $|\mathbf{k}'_0\rangle$ of an electron in Equation (3.22), the j-th electron scattering rate of the electron with an initial state $|\mathbf{k}_0\rangle$, the total rate used to generate the free flight, from Equation (3.17), is then given by:

$$\Gamma_j[n,\mathbf{k}_0] = \frac{2\pi}{\hbar}\sum_{m,\mathbf{k}'} \left|H^{a,e}_{m,\mathbf{k}'_0;n,\mathbf{k}_0}\right|^2 \delta(E(\mathbf{k}'_0) - E(\mathbf{k}_0) \mp \hbar\omega) \tag{3.24}$$

3.3.6 Scattering Process

Both electrons and holes, aka free carriers, interact with the crystal lattice and each other through a variety of scattering mechanisms which relax the energy and momentum of the particle. The scattering mechanism is given by Fermi's Golden rule [88] as introduced in Section 3.3.5. However, there are limitation to the use of the Fermi's Golden rule due to the effects such as collision broadening and finite collision duration time [103] but these are beyond of the scope of this work.

Scattering mechanism are roughly divided into three categories: (1) crystal defects which are primarily elastic; (2) lattice scattering between carriers and phonons which are inelastic and finally; and (3) scattering between the carrier's, carrier-carrier scattering. Phonon scattering involves different modes of vibration, acoustic or optical along with both transverse and longitudinal modes. We also designate inter- or intra-valley scattering which comes from whether the initial and final states are in the same valley or in different valleys. Once the scattering rates are calculated using on Fermi's Golden rule, they are tabulated in a scattering table in order to be selected when required.

In this thesis, the MC simulator uses the following scattering mechanism; **(1) electron —acoustic phonon interaction; (2) electron—ionised impurity interaction; (3) electron—polar optical phonon interaction;** and **(4) electron—non-polar optical phonon interaction (intra-valley and inter-valley)**.

(1) Electron–Acoustic Phonon Interaction. The electron interaction with acoustic phonons assumes that the charge between neighbouring cells is minimal and only introduces a small change in the lattice constant and energy band. The instantaneous change of the energy band causes scattering of the carriers with a phonon. An electron scattering rate for the acoustic potential of phonons is calculated using the following formula:

$$\Gamma(E) = \frac{\sqrt{2}m^{3/2}k_B T_L D^2_{acoustic}}{\pi\rho v_S^2 \hbar^4}\sqrt{E(1+\alpha E)}(1+2\alpha E)F(E) \tag{3.25}$$

where $D_{acoustic}$ is the deformation potential, k_B is Boltzmann constant, α is the non-parabolic parameter for the initial valley, T_L is the lattice temperature, ρ is the density of the material, v_S is the velocity of sound and $F(E)$ is equal to the following:

$$F(E) = \frac{(1+\alpha E)^2 + 1/3(\alpha E)^2}{(1+2\alpha E)^2} \tag{3.26}$$

This electron-acoustic phonon scattering assumes that the acoustic phonon energy $\hbar\omega_0$ is much smaller than $k_B T$ at room temperature. Therefore, assuming the elastic equipartition approximation, the acoustic scattering in Equation (3.25) is considered to be an elastic scattering process ($\hbar\Omega = 0$, Ω is the phonon frequency) [104, 105].

(2) Electron–Ionised Impurity Interaction. Modern semiconductor devices are usually doped with either acceptors or donors or both. With these dopants a scattering is experienced due to Coulomb potential from the dopants in doped regions. An electron scattering rate for an interaction with ionised impurities with the form factor calculated using electron overlap wave-function approximation from [106]. The scattering rate can be calculated from:

$$\gamma(E) = \frac{N_i e^4}{8\pi\sqrt{2m}(\epsilon_0\epsilon_S)^2}\frac{1+2\alpha E}{[E(1+\alpha E)]^{3/2}}\left\{\frac{\left[1+2c_k^2\frac{\beta_E^2}{4E(1+\alpha E)}\right]^2}{\frac{\beta_E^2}{4E(1+\alpha E)}\left(1+\frac{\beta_E^2}{4E(1+\alpha E)}\right)} + c_k^2\left[1+2c_k^2\frac{\beta_E^2}{4E(1+\alpha E)}\right]\log\left[\frac{\frac{\beta_E^2}{4E(1+\alpha E)}}{1+\frac{\beta_E^2}{4E(1+\alpha E)}}\right] + \left(c_k^2\right)^2\right\} \tag{3.27}$$

where N_i is the concentration of ionised impurities, ϵ_0 is permittivity of vacuum, ϵ_S is the relative static permittivity of the material, α is the non-parabolic parameter for the initial valley and c_k^2 and β_E^2 are defined as:

$$c_k^2 = \frac{\alpha E}{1+2\alpha E} \tag{3.28}$$

$$\beta_E^2 = \frac{\hbar^2}{2m}\frac{e^2 N_i}{\epsilon_0 \epsilon_S k_B T_L} \tag{3.29}$$

where β_E^2 is the Debye-Hückley inverse screening length in the energy form.

(3) Electron–Polar Optical Phonon Interaction. An inelastic process which is usually anisotropic in nature. A scattering rate for the interaction of an electron with polar optical phonon is found using the following [97]:

$$\Gamma(E) = \frac{\sqrt{m}\,e^2\omega_{pop}}{4\sqrt{2}\pi\hbar\epsilon_0}\left(\frac{1}{\epsilon_\infty} - \frac{1}{\epsilon_S}\right)\begin{bmatrix} N_0 \\ N_0+1 \end{bmatrix}\frac{1+2\alpha E}{\sqrt{\gamma(E)}}F(E,E') \tag{3.30}$$

where ϵ_∞ is relative high-frequency permittivity of the material, γ is defined by $\gamma(E) = E(1+\alpha E)$, N_0 is the Bose-Einstein distribution [107], ω_{pop} is the frequency of polar optical phonons, the electron final energy E' is defined as $E' = E \pm \hbar\omega_{pop}$, and $F(E,E')$ is defined as:

$$F(E,E') = \frac{1}{C}\left(A \cdot \ln\left[\frac{\sqrt{\gamma(E)} + \sqrt{\gamma(E')}}{\sqrt{\gamma(E)} - \sqrt{\gamma(E')}}\right] + B\right) \tag{3.31}$$

where A,B,C are defined as:

$$A = \left\{2(1+\alpha E)(1+\alpha E') + \alpha[\gamma(E)+\gamma(E')]\right\}^2 \tag{3.32}$$

$$B = -2\alpha\sqrt{\gamma(E)\gamma(E')}\left\{4(1+\alpha E)(1+\alpha E') + \alpha[\gamma(E)+\gamma(E')]\right\} \tag{3.33}$$

$$C = 4(1+\alpha E)(1+\alpha E')(1+2\alpha E)(1+2\alpha E') \tag{3.34}$$

(4) Electron—Non-polar Optical Phonon Interaction (Intra-valley and Inter-valley). The inter-valley scattering from different valleys is a very rare transition occurring with a low probability due to large energy distances between valleys but the inter-valley scattering is included in the MC simulation toolbox as the transition will

play a role at large kinetic energy of an electron. An electron scatting rate for the intra-valley or inter-valley interaction with non-polar optical phonons can be found using the following:

$$\Gamma(E) = \frac{Z_{ij} m^{3/2} D_{ij}^2}{\sqrt{2}\pi\rho\omega_{ij}\hbar^3} \begin{bmatrix} N_0 \\ N_0+1 \end{bmatrix} \sqrt{E'(1+\alpha E')}(1+2\alpha E')F(E,E') \tag{3.35}$$

where Z_{ij} is the number of equivalent valleys, D_{ij} is the non-polar optical potential, ω_{ij} is the non-polar optical frequency, N_0 is the Bose-Einstein distribution [107], the final energy after the scattering E' is defined by $E' = E \mp \omega_{ij} - \Delta V_{ij}$, with V_{ij} being the energy difference between valleys for inter-valley transitions, otherwise $\Delta V_{ij} = 0$ and $F(E,E')$ is defined as:

$$F(E,E') = \frac{(1+\alpha E)(1+\alpha' E') + 1/3\alpha E \alpha' E'}{(1+2\alpha E)(1+2\alpha' E')} \tag{3.36}$$

3.4 Beer-Lambert Law

Many materials absorb ultraviolet (UV) or visible (Vis.) light. The light radiation that passes through the material can be expressed using the rate of the intensity of the radiation which is directly proportional to the intensity of the incident light. The rate of the intensity also relates to the attenuation of light to the properties of the sample and one can use the rate to determine such things as the concentration or the bandgap of the sample. This relationship can be expressed by the Beer-Lambert Law which provides the necessary equation to work out the absorption, A, from the following equation [108]:

$$A = \log\left(\frac{I_0}{I}\right) \tag{3.37}$$

where I_0 is the incident light and I is the transmitted light as illustrated in Figure 3.37. The transmission, T, is $T = I_0/I$.

Beer-Lambert Law also gives the relationship between absorption coefficient, α, and light intensity, I, as [109]:

$$I_x = I_0 e^{-\alpha x} \tag{3.38}$$

This can be rearranged to give us an equation for the absorption coefficient in the form:

$$\alpha = \frac{1}{x}\ln\frac{I_0}{I} \tag{3.39}$$

where x is the thickness of the material and α is the absorption coefficient.

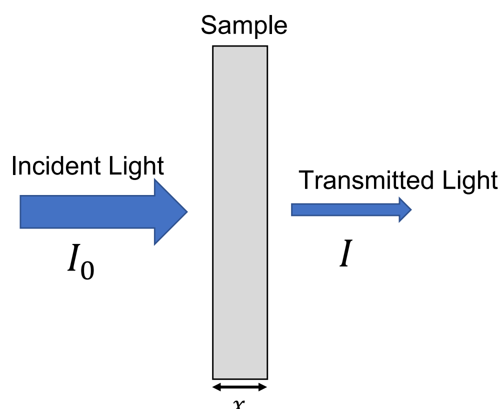

FIGURE 3.3. Beer-Lambert law schematically showing the incident light, the sample and the transmitted light.

3.5 Semiconductor Light Absorption

In this section, the fundamental absorption will be discussed, and refers to band-to-band or to excitation transitions, and other types of absorption such as dopant, excitonic or free carrier absorption will be neglected. This fundamental absorption is the process where electron-hole pairs are generated as a result of optical excitation of electrons from the valence band to the conduction band and a rapid rise in absorption can be seen. This process of light absorption must obey the conservation of energy and momentum laws. This leads to the fact that the minimum quantum energy needed to excite electrons from the valence band to the conduction band is equal to the bandgap of a semiconductor material. The fundamental absorption occurs at the red edge of the spectrum, usually within the visible and near ultraviolet spectral range, allowing the determination of a semiconductor materials bandgap energy, E_G, from UV-Vis Spectroscopy.

Semiconductor materials can be divided into two groups according the nature of their bandgap: (1) direct bandgap semiconductor materials where the position of the valence band top and the conduction band bottom coincide in **k**-space as shown in Figure 3.4(a) and (2) indirect bandgap where the valence band top and the conduction band bottom do not coincide in **k**-space as schematically shown in see Figure 3.4(b). Near the edge of the fundamental absorption in direct bandgap semiconductor materials only photon absorption is necessary for the transition from the valence band to the conduction band in order to conserve energy. However, in the case for an indirect bandgap semiconductor material, the addition of a particle, which changes the momentum of the electron is necessary in order to conserve energy and so a phonon assisted transition is

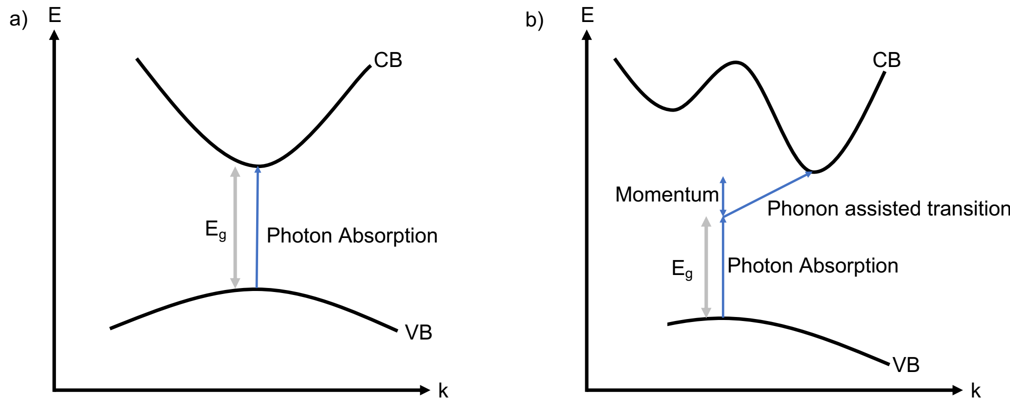

FIGURE 3.4. Transitions from the valence band to the conduction band: direct bandgap (a) and indirect bandgap (b).

observed. The probability of this process in indirect bandgap semiconductors decreases with increasing the number of particles [110]. Therefore, light absorption in indirect bandgap semiconductor materials near the absorption edge occurs less intense compares with direct bandgap semiconductor materials.

From the above discussion, this rise in absorption can be used to determine the energy or bandgap of a semiconductor material using the relation [111]:

$$E_G = \frac{hc}{\lambda_{red}} \tag{3.40}$$

where h is Planck's constant, c is the speed of light, λ_{red} is the red edge of absorption, i.e., the wavelength at which light absorption occurs and E_G is the bandgap. However, this is only a rough estimate of the bandgap as the energy distribution of the electron states differ from that of the density of state for an ideal crystal, see Figure 3.5a. This difference is due to the fact that real semiconductors are not perfect and the presence of inhomogeneities (defects) creates additional fields with respect to the periodic field of the lattice. These additional fields create the potential which depends randomly on the coordinates. The presence of these additional fields introduces the appearance of so-called band tails, as detailed in Section 3.6, in the density of the electronic state shown in Figure 3.5(b). The band tails will result in a red shift absorption edge, and so a reduced bandgap of the disordered semiconductor compared to that of an ideal semiconductor material.

To determine the bandgap energy more precisely, one can use the spectral dependence of the absorption coefficient, α, for transitions between the allowed states which can be

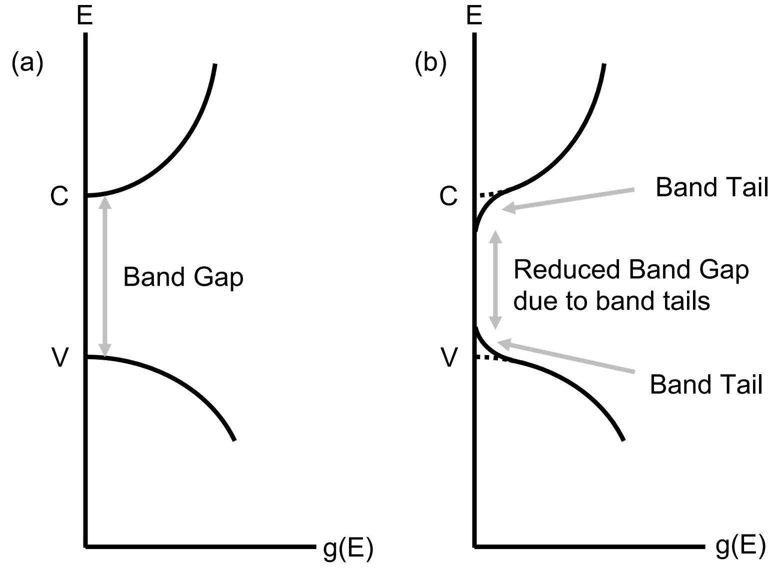

FIGURE 3.5. Density of state for: ideal (a) and real semiconductor (b).

described by the following relations [109]:

$$\alpha(h\nu) = A(h\nu - E_g)^{1/2} \tag{3.41}$$

and

$$\alpha(h\nu) = B(h\nu - E_g)^{2} \tag{3.42}$$

for direct and indirect transitions, respectively. In Equations (3.41) and (3.42), A and B are constants for that are independent of the wavelength and $h\nu$ is the photon energy. For example, $A = 100\ eV^{-1}$ for GaAs [112] and $B = 10\ eV^{-1}$ for Si [113].

Using the absorption coefficient, one can produce a Tauc plot, where certain power of the absorption coefficient can be taken in order to find the bandgap of the semiconductor to form so called Tauc coordinates. Equations (3.41) and (3.42) determine that the plot for a direct bandgap the Tauc coordinates would take a α^2 relation whereas, for an indirect bandgap, the plot would take $\alpha^{1/2}$ relation. These plots allow to extrapolate the energy gap, normally, with a straight line fit to the data and the intersection with the x-axis which then determines the bandgap value as illustrated in Figure 3.6. Note that this does not take into consideration the effects of band tailing.

An example of a complex Tauc plot for a indirect bandgap semiconductor material is shown in Figure 3.7 with three primary regions. First region is high absorption and corresponds to absorption due to electron transitions from one delocalized (band like)

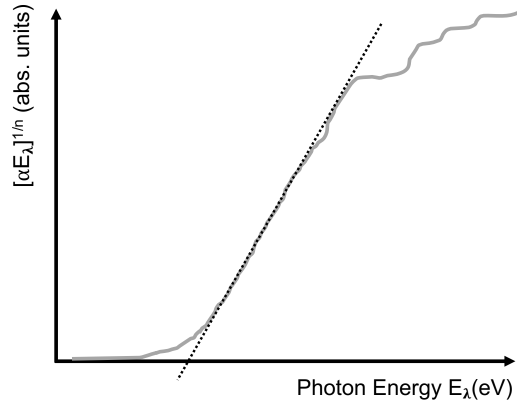

FIGURE 3.6. Theoretical curve shape of a Tauc Plot, showing a linear fit to determine the semiconductor optical bandgap.

state to another delocalized state. Typically, this region is for band-to-band transitions where the absorption coefficient exhibits a power-law decrease. The second region is absorption from band like states to band tail states, or band tail states to other band tail states. The density of states is still quite high. In this region, the absorption coefficient typically falls exponentially. Finally, region three have transitions to/from or among localized states in the mobility gap and the absorption is roughly constant has less of a decay than the other regions.

3.6 Band Tailing

Here we will discuss the perturbation of the bands with the formation of 'band tails' or 'tail states' that extend the bands into the energy gap, see Figure 3.5. These band tails can influence the fundamental absorption in so, by reducing the bandgap. This is more likely to be a feature of indirect bandgap due to the phonon process that is seen in conserving energy. This phonon process can be impacted by impurities and or disorder in the semiconductor. Therefore, it is worth taking this into account when extracting the bandgap of indirect bandgap semiconductors from optical spectroscopy.

Characterized by the tail parameter, E_0, and depend on impurity and carrier concentration, temperature and structural disorder [115], band tailing theory is still something of a current problem being investigated. It is however a feature of amorphous semiconductors [116] and heavily doped semiconductors [117].

At the absorption edge, the band density of states just beyond the mobility edge for a

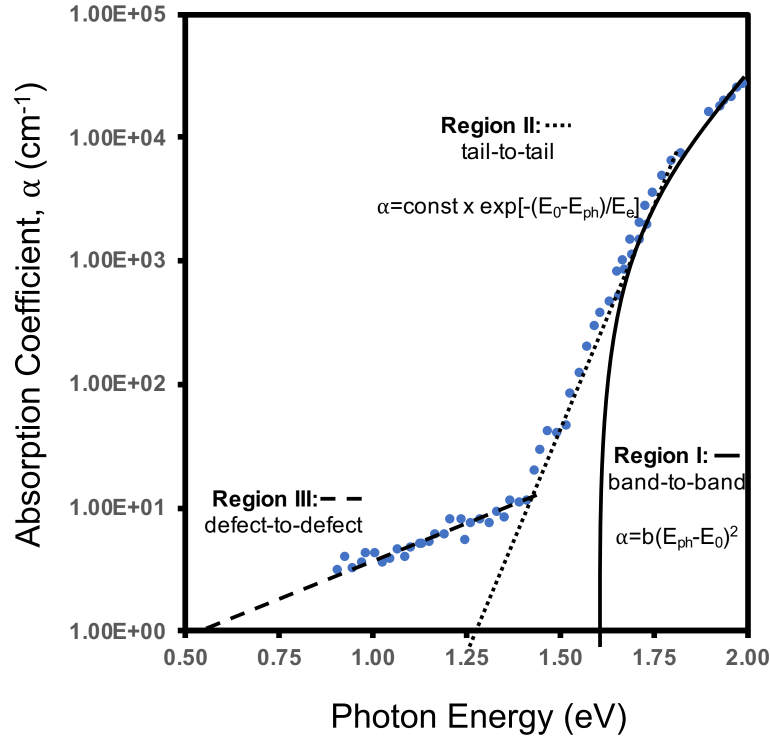

FIGURE 3.7. Complex Tauc plot showing three different regions, image based on Figure 8.11 from [114]

.

free-electron system is normally represented by a power law [114, 118]. Likewise, the same power law expansion can be used as we know that there is a quadratic dependence near the maximum or the minimum of any power-law expansion of any function around an extremum. This power law is seen in Region I of Figure 3.7 where an absorption edge is defined based on fitting this section of the absorption spectrum with the function:

$$\alpha = b\,(E_{ph} - E_0)^2 \tag{3.43}$$

where E_{ph} is the photon energy, E_0 is the absorption edge energy, and b is a constant.

In semiconductor materials, there are states in the energy gap that decrease in density roughly exponentially as one moves into the bandgap [114]. This results in the absorption coefficient decreasing exponentially below the absorption edge energy, E_0, in Equation (3.43) forming:

$$\alpha = \text{const} \times \exp[-(E_0 - E_{ph})/E_e] \tag{3.44}$$

where E_{ph} is the photon energy, E_0 is the absorption band edge energy and E_e is the characteristic width of the dominant band edge, typically < 0.1 eV. The less steep the

absorption band edge the wider the band-tail is. This band-tail depends upon the details of the semiconductor involved. For instance, in a homopolar semiconductor such as silicon, the band-tail will be relatively symmetrical with differences primarily resulting from the effective mass of the bands. If we have a more complex ternary or multinary compound semiconductor, the sublattice on which the substantial disorder occurs may determine the greater band edge width.

3.7 Photoelectric Effect

The principle of the photoelectric effect states that, under some circumstances (such as light shining on a metal), electrons known as photoelectrons are emitted from a material. It was first explained by Einstein winning him a Nobel Prize in 1921. These photoelectrons are produced from a single step process whereby electrons that are initially bound to an atom/ion are ejected by a photon. This process involves the transfer of energy from the photon to the electron. If this energy is sufficient, the process will result in the emission of the electron from the atom/ion and, therefore, from the material.

The photoelectron effect can be very useful in the study of material proprieties by using photons in the X-ray regime to bombard a sample. Such a process is known as X-ray Photoelectron Spectroscopy (XPS) and will be details in Section 3.8.

3.8 X-ray Photons for X-ray Photoelectron Spectroscopy

XPS uses an incident X-ray photon which knocks out an electron that has a binding energy keeping it in its orbit around the atom. The kinetic energy (KE) of this emitted electron can be measured making it a useful tool in surface analyse of a material as the KE is element and environment specific and a function of the binding energy (BE):

$$KE = E_{ph} - BE - \Phi \tag{3.45}$$

where E_{ph} is the known photon energy and Φ is the work function of the instrumentation. The KE of the emitted photoelectron allows calculate the binding energy from Equation (3.45) by knowing the work function of the instrumentation and the energy of the incident X-ray photon.

Equation (3.45) does not cover Auger emissions as Auger electron emission is a three-stage process. The first electron represents the photoelectron, E_{ph}, the second and

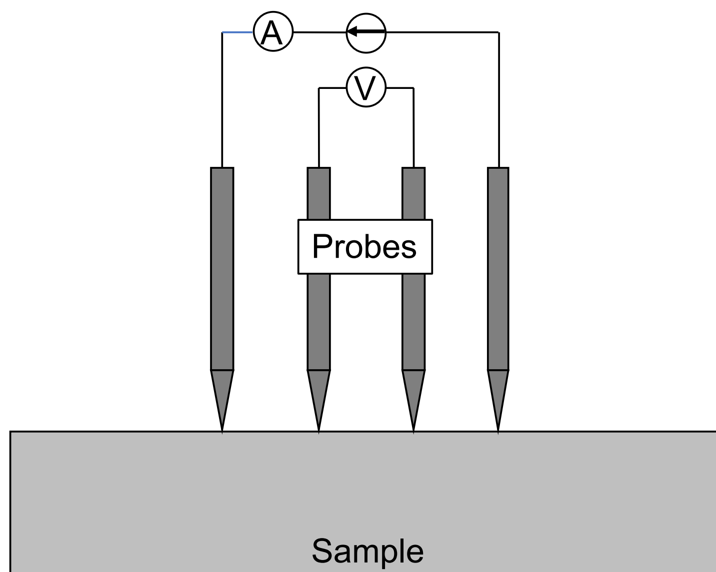

FIGURE 3.8. Schematic of a linear four-probe set up for mobility measurements.

the third are associated with energy of core holes. The second electron drops down from a level which is less that BE in order to fill a core hole. The third electron is used to conserve energy and remove excess energy associated with this transition.

3.9 Four Probe Method

In 1958, Van der Pauw [119] showed a new four-probe technique for measuring electrical properties such as resistivity, that is easier to implement than the linear four-probe approach that has been previously used as shown in Figure 3.8.

Van der Pauw's approach [119] showed that the sheet resistivity of a metallic sample can be obtained from any arrangement of four probe contacts on the edge of a flat homogeneous sample of known thickness. This four-probe method works by passing a current through two probes and measuring the voltage through two separate probes as shown in Figure 3.9. The resistance $R_{ab,dc}$ is defined as $R_{ab,dc} = (V_c - V_d)/j_{ab}$ using a potential difference between probes, c and d when current j_{ab} flows between probes a and b. Likewise, the resistance $R_{bd,ac}$ is defined in a similar way.

The Van der Pauw relationship is given by:

$$\exp\left(-\frac{R_{ab,dc}}{\lambda}\right) + \exp\left(-\frac{R_{bd,ac}}{\lambda}\right) = 1 \tag{3.46}$$

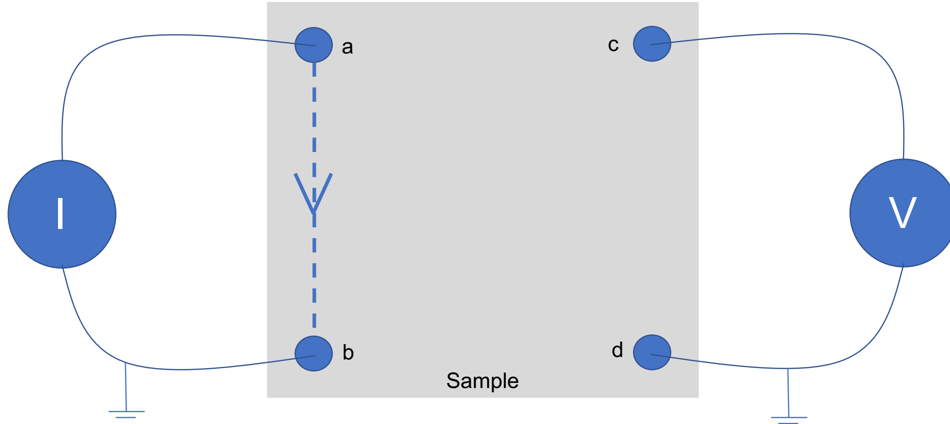

FIGURE 3.9. Schematic of Van der Pauw four-probe set up.

where $\lambda = \rho/\pi d$ and ρ is the resistivity of the metallic sample with thickness d. The Van der Pauw relation enables various measurements to be made to find out the resistivity , mobility, carrier density, and Hall coefficient of a metallic sample that have arbitrary geometry.

The Hall effect measurements are commonly used to characterize semiconductors in order to acquire physical quantities like Hall voltage, conductivity type, carrier density, and mobility. To facilitate the Hall effect, a magnetic field needs to be introduced in order to obtain the Hall voltage which can be measured using the configuration in Figure 3.10. By taking eight Hall voltage measurements, the average Hall coefficient, R_H, can be calculated from following expressions for Hall coefficients. The vertical Hall coefficient can be obtained as:

$$R_{HC} = \frac{t_s(V_{b-c+} - V_{c-b+} + V_{c-b-} - V_{b-c-})}{4BI} \tag{3.47}$$

while the horizontal Hall coefficient can be obtained as:

$$R_{HD} = \frac{t_s(V_{d-a+} - V_{a-d+} + V_{a-d-} - V_{d-a-})}{4BI} \tag{3.48}$$

where t_s is the sample thickness, V is the voltage, I is the current through the sample and B is the magnetic flux. The average Hall coefficient (R_H) can be calculated from vertical R_{HC} and horizontal Hall coefficients R_{HD} as follows:

$$R_H = \frac{R_{HC} + R_{HD}}{2} \tag{3.49}$$

The mobility (μ_H) of the sample can be determined from the Hall coefficient (R_H) and the resistivity (ρ) using the expression:

$$\mu_H = \frac{|R_H|}{\rho} \tag{3.50}$$

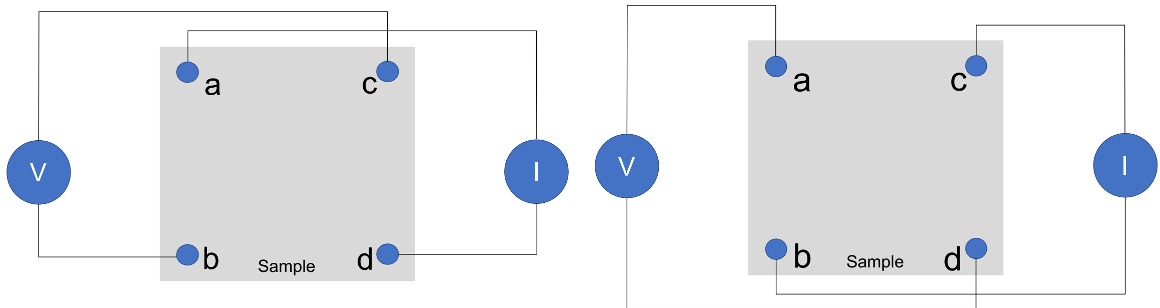

FIGURE 3.10. Hall voltage measurement configurations. Here a, b, c and d are the locations of the probes on the sample with two configurations: (left) c and b are to apply a voltage and a and d are to measure a current, (right) a and d are to apply a voltage and c and b are to measure a current.

3.10 Device Modelling

Device modelling primarily uses transport models in the simulation of carrier transport in a semiconductor device and can vary in their degree of complexity and computational cost. These are both usually a sign of how accurate the model is in describing the physical behaviours of a semiconductor device. When a given problem is presented, the approach that is normally taken requires a compromise between accuracy and time it takes. The simplest of transport models is the drift-diffusion model assumes that the carrier temperature is at equilibrium with a lattice temperature. The drift-diffusion model along with some other basic semiconductor equations make up the basic approach to device modelling and will be described in the following sections. In this work, a drift-diffusion model in commercial software Atlas by Silvaco [40] adopts the following models for modeling a heterostructure device: **(1) field-dependent mobility; (2) Shockley-Read-Hall (SRH) recombination; (3) Auger recombination; and (4) Poisson's equation**.

3.10.1 Field-Dependent Mobility

There are two types of electric field-dependent mobility models that are used in Silvaco Atlas: (1) The Standard Mobility Model, and (2) Negative Differential Mobility Model. We will only consider the standard mobility model which takes into account velocity

saturation and is defined as [40]:

$$\mu_n(E) = \mu_{n0}\left(\frac{1}{(1+\left(\frac{\mu_{n0}E}{V_{\mathrm{SAT}N}}\right)^{\beta_n}}\right)^{1/\beta_n} \tag{3.51}$$

$$\mu_p(E) = \mu_{p0}\left(\frac{1}{(1+\left(\frac{\mu_{p0}E}{V_{\mathrm{SAT}P}}\right)^{\beta_p}}\right)^{1/\beta_p} \tag{3.52}$$

where $V_{\mathrm{SAT}N}$ and $V_{\mathrm{SAT}P}$ are the saturation velocities for electrons and holes, β_n and β_p are constants, and μ_{n0} and μ_{p0} are the electron and hole low field mobility.

3.10.2 Shockley-Read-Hall Recombination

Shockley-Read-Hall (SRH) recombination [120] is a two particle process as illustrated in Figure 3.11. The SHR recombination considers carrier generation in space charge regions and recombination in, for example, high injection regions. The SHR recombination is given [121]:

$$R^{SRH} = \frac{n \cdot p - n_i^2}{\tau_p \cdot (n+n_1) + \tau_n \cdot (p+p_1)} \tag{3.53}$$

where τ_p and τ_n are the lifetimes of the holes and electrons, respectively, p and n are hole and electron concentration, respectively, and $n_i^2 = n_1 \cdot p_1$ and n_i is the intrinsic concentration. The variables n_1 and p_1 are defined as follows:

$$n_1 = N_C(T_L) \cdot \exp\left(\frac{-E_C + E_T}{k_B \cdot T_L}\right) \tag{3.54}$$

$$p_1 = N_V(T_L) \cdot \exp\left(\frac{-E_T + E_V}{k_B \cdot T_L}\right) \tag{3.55}$$

where E_T is the trap energy level, N_C and N_V are the carrier effective densities of state, T_L is the lattice temperature, E_C and E_V are the conduction band and valence band energy, respectively, and k_B is the Boltzmann constant.

3.10.3 Auger Recombination

Auger recombination is a three particle process, as shown in Figure 3.11, in which an electron and a hole recombine in a band-to-band transition. However, the resulting

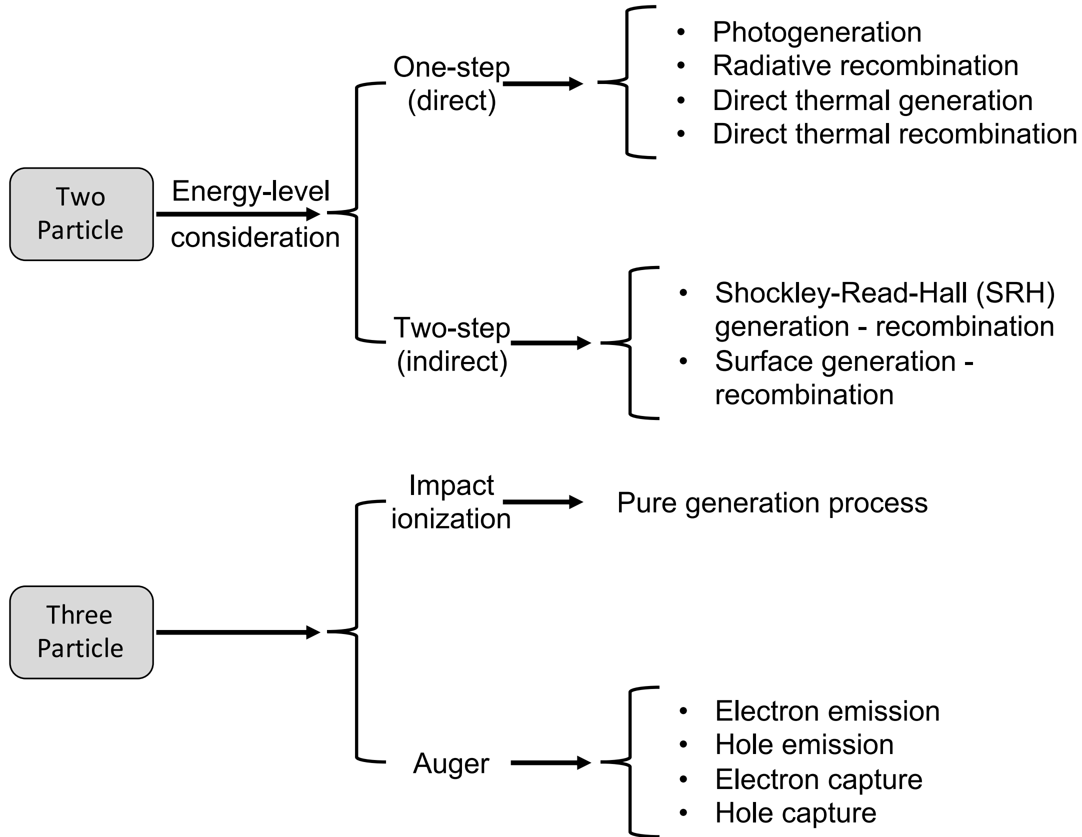

FIGURE 3.11. Groupings for generation - recombination process.

energy is given off to another electron or hole. As Auger recombination involves a third particle, it had to be treated differently from the band-to-band recombination. The standard equation for Auger recombination is given by:

$$R_{Auger} = C_n(pn^2 - nn_1^2) + C_p(np^2 - pn_1^2) \tag{3.56}$$

where C_n and C_p are the Auger coefficients, n and p are electron and hole concentrations, respectively, and n_1 is defined in Equation (3.54).

3.10.4 Poisson's Equation

Poisson's equation gives the relationship between electrostatic potential and the local charge densities. The electric field is defined as a negative gradient and therefore as a negative derivative of the electrostatic potential. This is due to the electric field starting off at a higher potential region and pointing towards a lower potential region. Poisson's

equation is given by [122]:

$$\frac{d\Psi(x)}{dx} = -E(x) \tag{3.57}$$

where E is the electric field and Ψ is the electrostatic potential. From Gauss Law, the electric field is related to the local charge density, $\rho(x)$, by the following relation [122]:

$$\frac{dE(x)}{dx} = \frac{\rho(x)}{\epsilon} \tag{3.58}$$

where ϵ is the permittivity of free space. Substituting the expression of the electric field from Equation (3.57) into Equation (3.58) gives the relationship of the charge density against the potential as:

$$\frac{d^2\Psi(x)}{dx^2} = -\frac{\rho(x)}{\epsilon} \tag{3.59}$$

Equation (3.59) is commonly used, for example, to determine the potential and field distribution caused by a charge density, ρ, within the depletion layer.

3.10.5 Continuity Equation

Derived from the first Maxwell Equation [123], the continuity equation (3.65) can be obtain with the following modifications. First the divergence operator 'div' is applied to the first Maxwell Equation:

$$\text{div rot } \vec{H} = \text{div } \vec{J} + \frac{\partial \rho}{\partial t} = 0 \tag{3.60}$$

where $\vec{J}$ is the total electric current density, t is time, ρ is the electric charge density and rot $\vec{H}$ is given by:

$$\text{rot } \vec{H} = \vec{J} + \frac{\partial \vec{D}}{\partial t} \tag{3.61}$$

Then we need to split the total conduction current density $\vec{J}$ into individual components for holes $\vec{J}_p$ and electrons $\vec{J}_n$ as:

$$\vec{J} = \vec{J}_p + \vec{J}_n \tag{3.62}$$

The space charge density is also needed to be taken into account when deriving the continuity equation. This is simply given by:

$$\rho = q \cdot (p - n + C) \tag{3.63}$$

where n and p are electron and hole concentrations, respectively, C is the net ionized impurity concentration, and q is the elementary charge.

We will assume that all charges in the semiconductor (not including the mobile carrier electrons and holes) are invariant. Therefore, we can neglect the influence of charged defects giving:

$$\frac{\partial C}{\partial t} = 0 \tag{3.64}$$

If we combine Equations (3.60), (3.62), and (3.63), while making use of Equation (3.64), we obtain the following continuity equation:

$$\mathrm{div}(\vec{J}_p + \vec{J}_n) + \frac{\partial}{\partial t}(p - n) = 0 \tag{3.65}$$

3.10.6 Drift-Diffusion Transport Model

In this thesis, the drift-diffusion transport model have been primarily used in our device modeling. The drift-diffusion transport model assumes that carrier are in thermal equilibrium, and that the velocity of carriers will respond to changes in the electric field instantaneously. With these simple assumptions, the drift-diffusion transport model gives a simple computational effective tool for simulating semiconductor devices.

The drift-diffusion model is made up of the following set of equations: **(1) Current-Density Equations; (2) Continuity Equations;** and **(3) Poisson's Equation** as follows:

(1) Current-Density Equations [87]. The most common current conduction consists of the drift component, usually caused by an electric field, and the diffusion component, caused by the carrier-concentration gradient. These two components can be written for both the electrons (n) and the holes (p) in a device using equations:

$$J_n = qn\mu_n E + qD_n \nabla n \tag{3.66}$$

$$J_p = qp\mu_p E - qD_p \nabla p \tag{3.67}$$

$$J_{cond} = J_n + J_p \tag{3.68}$$

where J_n and J_p are the electron and hole current densities, respectively, μ_n and μ_p are the electron and hole mobility, respectively, E is the electric field, and D_n and D_p are the diffusion coefficients of electrons and holes, respectively.

(2) Continuity Equations include time-dependent phenomena such as low-level injections, generation, and recombination. The continuity equations for the electrons (n) and holes (p) can be written as:

$$\frac{\partial n}{\partial t} = G_n - U_n + \frac{1}{q}\nabla \cdot J_n \tag{3.69}$$

$$\frac{\partial p}{\partial t} = G_p - U_p + \frac{1}{q}\nabla \cdot J_p \tag{3.70}$$

where G_n and G_p are the electron and hole generation rates, respectively, and U_n and U_p are the the electron and hole recombination rates, respectively.

(3) Poisson's Equation for drift-diffusion which takes into account ionised donor and acceptor impurity densities is given by:

$$\nabla \cdot \epsilon \nabla V = -(p - n + N_D^+ - N_A^-) \tag{3.71}$$

where V is the electrostatic potential, E is the applied electric field, n and p are the density of electrons and holes, respectively, and N_D^+ and N_A^- are the density of ionised donor (D^+) and acceptor (A^-) impurities, respectively.

3.11 Summary

This chapter provides information on calculation of the effective mass using a dispersion relationship at the point where the conduction band is at its minimum. The chapter gives details about the ensemble MC technique that was used to obtain bulk transport properties including a Fermi's Golden Rule assumed to be valid for scattering mechanisms, selection of the scattering process, free flight generation, and a generation of the final state after scattering.

The middle section of this chapter provides background information for the experiments that were performed as part of this thesis. This started off by description of the UV, IR, Vis Spectroscopy, whereby the Beer-Lamberts Law was detailed followed by aspects of light absorption in semiconductors and the band tailing. This is followed by details on the photoelectric effect and X-ray Photons for X-ray Photoelectron Spectroscopy. The last experiments that are performed are two- and four-probe methods for I-V characteristic measurements. Therefore, the four-probe method is detailed in relation to Van der Pauw's approach and Hall effect measurements.

The last section of this chapter details the device modelling that was undertaken using Silvaco Atlas. We have overviewed the transport models used in the simulation of carrier transport in a semiconductor device describing the field-dependent mobility model followed by two recombination models (Shockley-Read-Hall and Auger). Finally, Poisson's equation and the equations for drift-diffusion transport model including the continuity equation are detailed.

Chapter 4

Methodology

The chapter is organized as follows: Section 4.1 starts with an introduction into the MC simulator used and the material properties of Al_4SiC_4 that are of interest to the computational model. The chapter also outlines the scattering mechanisms relevant to carrier transport in Al_4SiC_4. Also, due to the positioning of the valleys in Al_4SiC_4 a new valley transformation is derived for two of the three M valley, that is the M_2 and M_3 valleys, see Figure 2.1, because of their respective positions from the principle M valley. Section 4.2 looks at the experimental method for spectrophotometry, X-ray photoelectron spectroscopy and two and four probe measurements. The final section, Section 4.3, details the methodology for the device simulations which uses commercial Technology Computer Aided Design (TCAD) software and mentions material models and specifies methods used in the simulations.

4.1 Ensemble Monte Carlo Simulator

The ensemble MC technique detailed in Chapter 3 is well suited to forecast electron transport properties of semiconductors [124]. Therefore, this technique is used to assess electron transport properties of ternary carbide Al_4SiC_4 by adopting our in-house developed ensemble bulk MC code [125]. The bulk MC method assumes that carriers move in infinite real space and, therefore, the particle position is sufficient to track only in

momentum/**k**-space. In the momentum space, Equation 3.5 simplifies to:

$$\frac{\partial f}{\partial t} = -\mathbf{F} \cdot \Delta_{\mathbf{k}} f + \left(\frac{\partial f}{\partial t}\right)_{collision} \tag{4.1}$$

The in-house ensemble bulk MC code uses analytical non-parabolic ellipsoid band structure with the $E - \mathbf{k}$ relation given by:

$$E(\mathbf{k}) = \frac{\hbar^2}{2m^*}(k_x^2 + k_y^2 + k_z^2) \tag{4.2}$$

The simulation moves the particles individually at a set time step for a set amount of time with scattering events occurring assuming free flights under constant electric field. This process requires calculation of free flight time for each particle, which intern depends on the total scattering rate. The free flight time is determined stochastically by generating a uniform random number r into the analytical form in Equation 3.16. After the free flight has been determined, the scattering can take place using a pre-calculated scattering probability followed by determination of the electron state after the scattering. The electron scattering probability is calculated using Fermi Golden Rule which is first-order time-dependent perturbation theory assuming a weak perturbation [104], see Section 3.3.5. Physical quantities of interest for carriers such as average velocity, total and kinetic energy, diffusion constant, relaxation time, or valley occupation can be monitored during the simulation run at any time step and outputted, typically, at the end of the whole simulation run. Further information on the MC code can be found in Section 3.3.

4.1.1 Monte Carlo Implementation

The in-house developed ensemble bulk MC simulation code has been adapted to investigate the electron transport in bulk Al_4SiC_4 with full details of the model outlined in Section 3.3. The simulations predict bulk properties of Al_4SiC_4 when electron transport can be considered to be free in the 3D **k**-space. We have employed a two-valley model for the conduction band of Al_4SiC_4 based on the band-structure obtained by Pedesseau et. al. [52] as seen in Figure 4.1. The two arrows in this figure indicate the two valleys that we are considering in the simulation model. The first valley, the M valley, is situated 2.78 eV above the valence band maximum of the Γ valley and provides an indirect bandgap. The second valley, the K valley, is situated 0.52 eV above the M valley, see Figure 4.2, and provides also an indirect bandgap. We have chosen to use the value of 2.78 eV for the bandgap as this has been obtained in our experimental work [126].

Figure 4.2 includes the number of equivalent bands that have been identified for the two valleys of interest for MC simulations. The number of equivalent valleys in

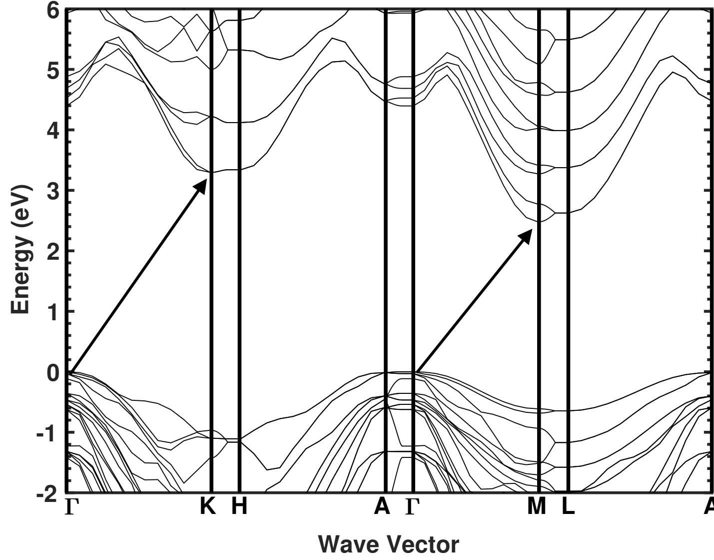

Figure 4.1: Re-scaled Al_4SiC_4 bandstructure obtained from Pedesseau et. al. [52] DFT calculations, with two black arrows indicate the two valleys that we are considered in the MC simulations.

each of the two valleys is based on the hexagonal lattice that Al_4SiC_4 is known to have [41–43, 50, 52, 57, 75]. Figure 5.1(a) shows that the K valley is present in six locations, each of which contribute one third to the first Brillouin zone leading way to a total of two equivalent bands. The M valley is present in six locations similar to the K valleys. However, due to their positions between the K valleys, each of these six M valleys contribute one half to the first Brillouin zone leading way to a total of three equivalent bands. The band-structure model of Al_4SiC_4 is analytical non-parabolic anisotropic band-structure [127]. We have considered the following electron scattering mechanisms in the MC simulations which will play a decisive role in the electron transport (see Table 4.1): electron interactions with acoustic phonons, with polar and non-polar optical phonons, and with ionised impurities when simulating electron transport properties in a n-type doped Al_4SiC_4.

The MC simulations assume a crystal temperature at 300 K and the orientation of applied electric field along ⟨0001⟩ crystallographic direction of hexagonal lattice structure [41–43, 50, 52, 57, 75]. The material parameters, including parameters for electron-phonon interactions, are collected in Table 4.2. In the case of acoustic deformation potential, we have opted for the value reported for 4H-SiC [84] as the closest semiconductor material to Al_4SiC_4 with a well-known electron-phonon deformation potential

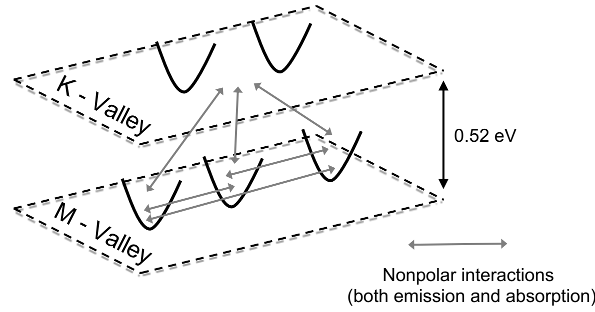

Figure 4.2: Schematic of conduction band minimum valleys in Al_4SiC_4 showing the number of equivalent bands in each valley and the separation between the two considered valleys.

because an acoustic deformation potential is currently unknown in Al_4SiC_4. The critical electric field of Al_4SiC_4 is calculated, to ensure that we only simulate below this value, using [128]:

$$\epsilon_c = a(E_G)^n \tag{4.3}$$

where $a = 2.3818 \times 10^5$ and $n = 1.995$ for an indirect bandgap semiconductor, and E_G is the bandgap of the semiconductor. Assuming the bandgap of 2.78 eV, we obtain a critical electric field of 1831 kV cm^{-1} for Al_4SiC_4. This critical electric field is well below our maximum electric field of 1400 kV cm^{-1} we have simulated to.

The optical phonon energies that have been used in these simulations have been extracted from IR/Raman spectroscopy from the works of Zevgitis et al. [42]. Here, we have taken the three highest peaks in the Z(XX)Z polarisation configuration, where one would expect to see only A_1 and E_2 modes. The first peak we have taken is at a wave-number of 690 cm^{-1}, which relates to an energy of 85.55 meV, is an E_2, non-polar mode, longitudinal optical phonon. The second peak is at a wave-number of 543 cm^{-1}, which relates to an energy of 67.32 meV, and is an A_1, polar mode, transverse optical phonon. Finally, the third peak is at a wave-number of 865 cm^{-1}, which relates to an energy of 107.25 meV, and is an A_1, polar mode, longitudinal optical phonon.

At the moment, a specific relationship between vibrational states and electrons is not clear as to which vibrational states directly contribute or hinder the electron mobility. The electron effective masses in Table 4.2 have been extracted from DFT calculations by Pedesseau et al. [52]. Here, we have assumed that the minima of conduction band have a parabolic energy dispersion, see 3.1. The relative effective mass, m^*, can be then

Valley	Scattering Between	Polar / Non Polar	Inter / Intra - Valley
M_1	$M_1 \to M_1$	Polar	Intra
	$M_1 \to M_1$	Polar	Intra
	$M_1 \to M_2$	Non Polar	Inter
	$M_1 \to M_3$	Non Polar	Inter
	$M_1 \to K$	Non Polar	Inter
M_2	$M_2 \to M_2$	Polar	Intra
	$M_2 \to M_2$	Polar	Intra
	$M_2 \to M_1$	Non Polar	Inter
	$M_2 \to M_3$	Non Polar	Inter
	$M_2 \to K$	Non Polar	Inter
M_3	$M_3 \to M_3$	Polar	Intra
	$M_3 \to M_3$	Polar	Intra
	$M_3 \to M_1$	Non Polar	Inter
	$M_3 \to M_2$	Non Polar	Inter
	$M_3 \to K$	Non Polar	Inter
K	$K \to M_1$	Non Polar	Inter
	$K \to M_2$	Non Polar	Inter
	$K \to M_3$	Non Polar	Inter

Table 4.1: Electron-phonon transitions considered in the bandstructure model of Al_4SiC_4 for the MC simulations of electron transport.

extracted from the following relation:

$$\frac{1}{m^*} = \frac{1}{\hbar^2} \frac{\partial^2 E(\overrightarrow{k})}{\partial k^2} \tag{4.4}$$

The dispersion relation is a quadratic polynomial, as illustrated in Figure 3.1, in the form: $y = a + b\,x + c\,x^2$. The second order derivative, $2c$, is related to the energy dispersion relation by:

$$2c = \frac{\partial^2 E(\overrightarrow{k})}{\partial k^2} \tag{4.5}$$

Equation (4.4) is solved for the M and K valleys in both the longitudinal and transverse directions giving values of relative effective masses shown in Table 4.2.

4.1.2 Wave-vector Transformation

The location of the principal electron valley, M, in Brillouin zone requires that components of electron wave-vectors in the band structure anisotropic analytical model of MC simulations are transformed accordingly. Therefore, we have enhanced our MC

Table 4.2: Al_4SiC_4 material parameters.

Parameter (Unit)	Value
Mass Density (g/cm^3)	3.03[a]
Lattice Constant (Å)	3.28[a]
Piezoelectric Constant (C/m^2)	0.47[a]
Longitudinal Acoustic Velocity (m/s)	10577[a]
Transverse Acoustic Velocity (m/s)	6431[a]
Polar Optical Phonon Energies (meV)	67.32[b], 107.24[b]
Non-Polar Optical Phonon Energy (meV)	85.55[b]
Acoustic Deformation Potential (eV)	11.4[a]
Indirect BandGap (eV)	$E_G^{(M)}$ = 2.78 M-Valley
	$E_G^{(K)}$ = 3.30[a] K-Valley
Electron Effective Mass	$m_l^{*(M)} = 0.5678 m_e$ [c]
	$m_t^{*(M)} = 0.6952 m_e$ [c]
	$m_l^{*(K)} = 1.0569 m_e$ [c]
	$m_t^{*(K)} = 0.9360 m_e$ [c]

[a]Ref. [52] [b]Ref. [42]
[c]Extracted value from DFT calculations [52]

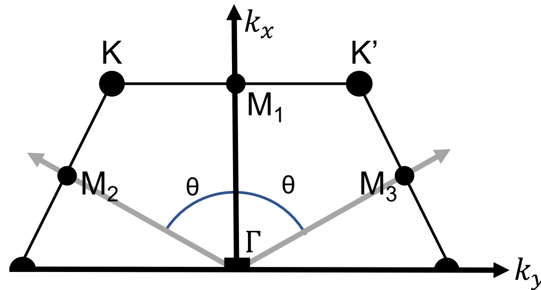

FIGURE 4.3. Location of the M valleys within the Al_4SiC_4 hexagonal structure, where $\theta = \pm 60$.

code with the wave-vector transformations which include a combination of Herring-Vogt transformation [129] and a rotational transformation of valleys.

The rotational transformation applied to the M valleys looks at transforming from an elliptical space **k**-vectors components, k_x, k_y, and k_z, to spherical vector components, k_x^*, k_y^*, and k_z^*, while considering the angular distance that the M_2 and M_3 valleys have in

relation to the M_1 valley, our reference valley, located along the k_x direction as illustrated in Figure 4.3. The angular distance that the M_2 and M_3 valleys have in a relation to the M_1 valley can be defined along the k_x and k_y axes, as these valleys are rotated about the k_z axis (the k_z axis does not need to be transformed). The **k**-vector transformations for each of the components are defined as:

$$k_x^* = k_x \cos(\theta) - k_y \sin(\theta) \tag{4.6}$$

$$k_y^* = k_y \cos(\theta) + k_x \sin(\theta) \tag{4.7}$$

$$k_z^* = k_z \tag{4.8}$$

In Eqs. (4.6—4.11), θ represents the angular distance the M_2 or M_3 valley rotates from the M_1 valley. The inverse transformations are given by:

$$k_x = k_x^* \cos(\theta) + k_y^* \sin(\theta) \tag{4.9}$$

$$k_y = k_y^* \cos(\theta) - k_x^* \sin(\theta) \tag{4.10}$$

$$k_z = k_z^* \tag{4.11}$$

Finally, we assume an isotropic valley approximation for the K valleys due to their low electron occupation.

4.2 Experimental Methods

4.2.1 Spectrophotometry

Spectrophotometry, also known as Transmission/Absorption Spectroscopy, is an analytical technique. It is based on measuring the amount of light absorbed, transmitted or reflected by a sample at a given wavelength, through the conservation of energy they are related as:

$$T + R + A = 1 \tag{4.12}$$

This technique is useful in characterising the absorption, transmission and reflectivity of a sample to reveal optical or electronic properties of a material.

FIGURE 4.4. Perkin Elmer Lambda 950 spectrophotometer (image taken from the Perkin Elmer website [130]).

In this work, a Perkin Elmer Lambda 950, see Figure 4.4, has been used to study the optical absorption of Al_4SiC_4 crystals. This spectrophotometer can measure transmittance and reflectance of light on or through a sample. Two sources of light provide the necessary frequencies of light in order to preform UV/Vis/NIR spectroscopy, first a deuterium arc lamp for UV light and then a tungsten-halogen lamp for visible and IR light. This allows the spectrophotometer to operate between 175-3300 nm of which we performed our experiments in the range of 250-1000 nm. Two detectors were used to cover this range. First, a photo-multiplier (PM) for the UV and visible wavelength and, second, an InGaAs sensor for the NIR wavelength. The two detectors switch over at 860.8 nm which is visible on the output data by a small blip. A custom aperture was made in order to mount the Al_4SiC_4 samples in order to cope with the small size of the crystals with diameters of 0.5, 1 and 2 mm. The acquisition of the optical signal was done in a cylindrical chamber with a geometric configuration to allow for a total transmittance acquisition, as shown in Figure 4.5.

The energy range of this spectrometer is adequate to excite inter-band excitation of outer electrons but over the threshold for vibrational states as this would require infrared energy levels. Figure 4.5 shows that the light is orthogonal to the sample. This allows for optical absorption to be calculated from the total transmittance using Beer-Lambert Law given by Equation (3.37) in Section 3.4.

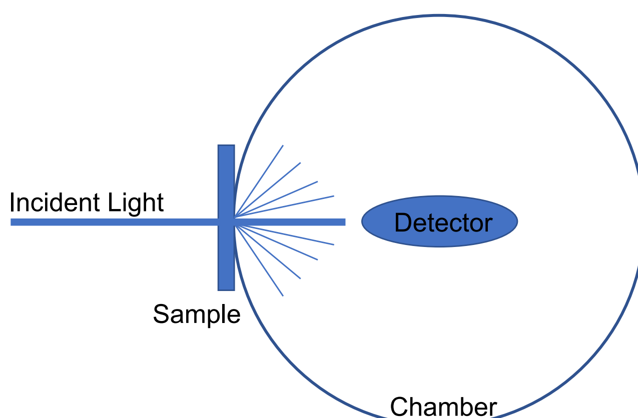

FIGURE 4.5. Geometric set up of the UV/Vis/NIR Spectrscopy chamber.

4.2.2 X-Ray Photoelectron Spectroscopy

A X-ray Photoelectron Spectroscopy (XPS) is a surface-sensitive quantitative spectroscopic technique. It is based upon the photoelectric effect, see Section 3.7, where emission of electrons is seen following the excitation of core level electrons by photons. It is useful for characterising the chemical composition and surface properties of materials as well as details regarding the valance band and work function of a material.

In this work, two different XPS set ups have been used. First, DAISY Fun (Darmstadter Integrated System for Fundamental Research) that incorporates PHOIBOS 150, Focus 500 with XR50M (SPECS) Al Kα at 1486.74 eV and, second, Kratos Supra XPS with Ocean optics USB 2000+ spectrometer. The operating principle for both set-ups remains the same.

Once the sample has been prepared and inserted into the apparatus, the sample is illuminated with a monochromatic light of energy $E_{ph} = h\nu$ where ν is the frequency of the light and h is Planck's constant. The energy range of E_{ph} will determine if the process is known at X-ray photoelectron spectroscopy (XPS) for $E_{ph} \approx 10^3$ eV or ultraviolet photoelectron spectroscopy (UPS) for $E_{ph} \approx 10^1$ eV. Energy transference for this process has been detailed in Section 3.8. The electron core levels for a element are displayed by a low energy distribution and their positions are characteristic for the emitting element and have a range of a few eV for different oxidation states. However, when it comes to the valence band, this is less well defined and exhibits a broad spectrum, with shifts large enough to make a clear assignment of elements difficult.

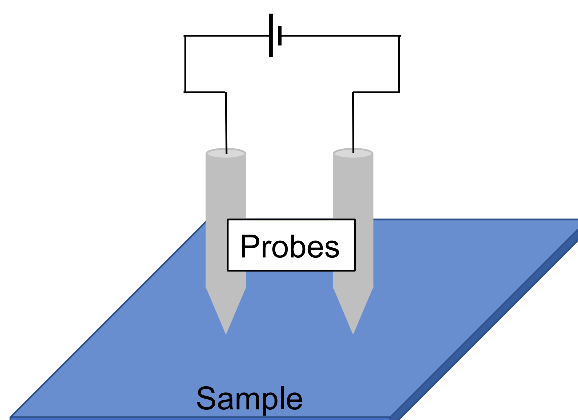

FIGURE 4.6. Two-probe set up.

4.2.3 Two and Four Probe Measurements

Two- and four-probe based instrumentation are techniques used to measure the I-V characteristics of a material and thus extract a sheet resistance of the material. The two-probe set up is simply passing a voltage through a sample and measuring the current output, see Figure 4.6. A four-probe set up is slightly more complicated as it employs a constant current through two of the probes and measures the voltage output across another set of probe and works by the Van der Pauw method described in Section 3.9 (see Figure 3.9).

In this work, both two- and four-probe set ups by a Ametek ModuLab XM Material Test System are used where the data are collected using the XM-studio Software in Grenoble, see Figures 4.7 and 4.8. In Swansea, the measurements has been taken by using the commercial software Ossila.

4.3 Technology Computer Aided Design

Technology Computer Aided Design (TCAD) is an electronic program design to automate the models of integrated circuit (IC) fabrication and device operation. Based on their application, there are two main categories: **(1) Process CAD** and **(2) Device CAD**.

(1) Process CAD is related to the simulations at the front-end of processing ICs and the steps required to fabricate a devices up to metallization. It is used to simulate such steps as oxidation and diffusion and deposition and etching to name a few. The process CAD is not used in this thesis and so will not be covered in any further depth.

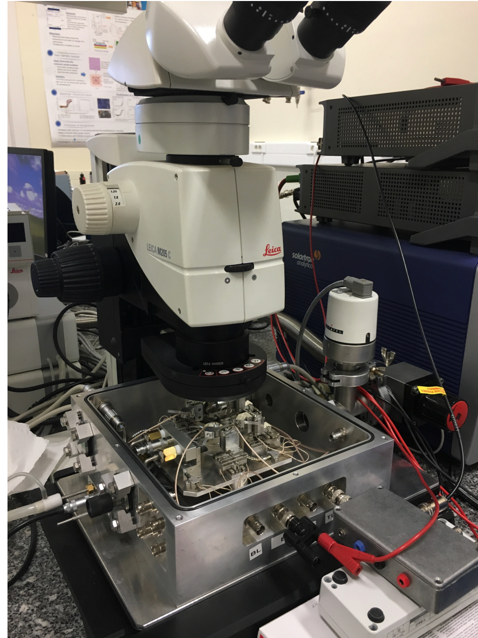

FIGURE 4.7. Probing station set up in Grenoble at Neel Institute with the chamber lid removed.

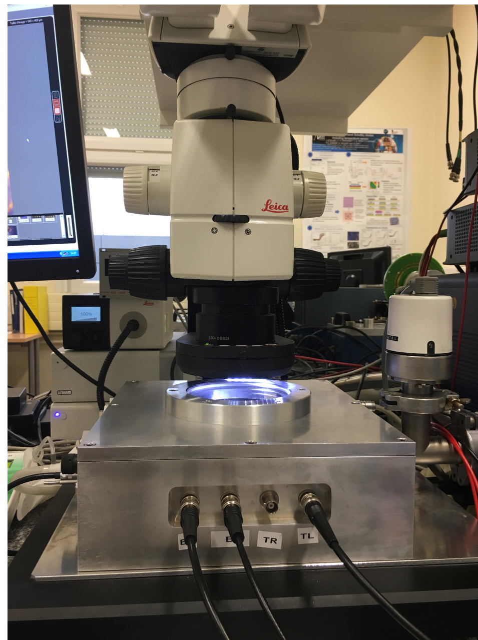

FIGURE 4.8. Side view of the probing station set up in Grenoble at Neel Institute with the chamber lid on and light shining onto the sample.

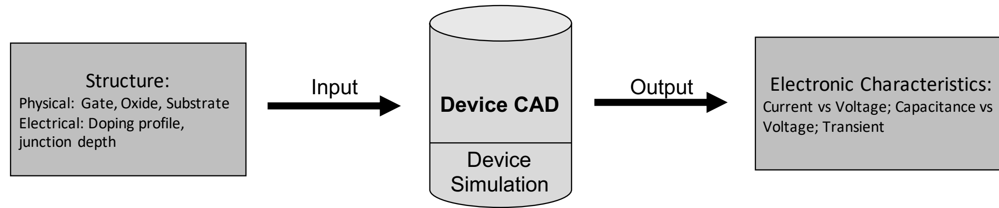

FIGURE 4.9. Flow diagram showing the process device CAD takes in order to run a simulation.

(2) Device CAD simulates IC device operations based on a suite of physical models that describe carrier transport in a material (see Figure 4.9). Device CAD ranges from simple drift-diffusion where it solves Poisson's Equation, Equation (3.71), and the continuity equations, Equations (3.69) and (3.70), to more complex and thus computationally challenging models such as the energy balance transport model, which solves a simplification of the BTE, or ensemble MC technique.

With TCAD, one is able to study a particular technology and explore it over a wide range of scenarios. This means that there is a fast and cost efficient way for device optimisation and technology development as well feasibility and reliability studies of a device.

In this thesis, the TCAD software of choice is the Silvaco package, which has the ability for both Process CAD (Silvaco Athena) and Device CAD (Silvaco Atlas). Here, Silvaco Atlas is used to model a SiC/Al_4SiC_4 heterostructure device. The methodology used in Silvaco Atlas is comprised in the following way [40]: **(1) structure specification; (2) material models specification; (3) numerical method selection; (4) solution specification;** and **(5) result analysis**, each of which are described in detail in the following sections.

4.3.1 Structure Specification

Apart from specifying the device structure to the required dimensions, it is important to specify an adequate mesh in order to define the geometry of the structure to be simulated, see Figures 4.10 and 4.11.

The mesh is used to define the points in the structure at which the physical parameters are calculated, i.e. electron or hole density. Silvaco Atlas uses the finite element method where the simulation domains are subdivided into small triangular regions and solved for the dependent variable in the sub-regions using a polynomial approximation [123]. This approach is easy to manipulate computationally and resulting smooth func-

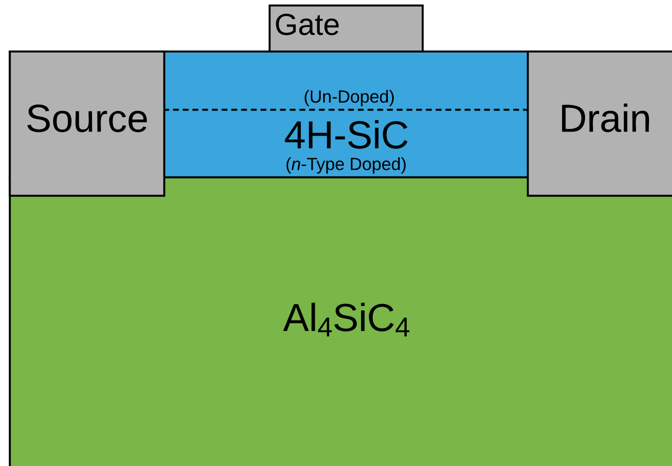

FIGURE 4.10. Schematic of the 5 μm gate heterostructure device that is studied. Full dimensions for the device are quoted in Chapter 5.

tions can be accurately approximated. It therefore comes at no surprise that if one has a dense mesh or a large number of nodes, the accuracy of the model improves, but at the cost of computational time. Therefore, one has to create a balance between accuracy and computational time.

The approach that is therefore taken is to have a dense mesh in the area where there is high electric field, interfaces, or regions of abrupt changes in the doping profile or concentration. If required, there are guidelines on how to create an effective mesh within the Silvaco Atlas manual [40].

4.3.2 Material Models and Method Specification

The semiconductor materials that make up the heterostructure device have their material properties defined using energy bandgap, permittivity, effective density of states, etc.. Additionally, a workfunction of the metal gate, that is associated with Schottky barrier height, is specified. The simulation of electron transport needs a model describing the dependence on the following: electric field, carrier concentration, and lattice temperature.

The Silvaco software provides a choice of numerical techniques that are used in solving the coupled, non-linear partial differential equations, that can describe semiconductor device operation. These numerical techniques are iterative and include: (1) Newton, (2) Gummel, (3) combined Newton-Gummel, and (4) Block methods. The it-

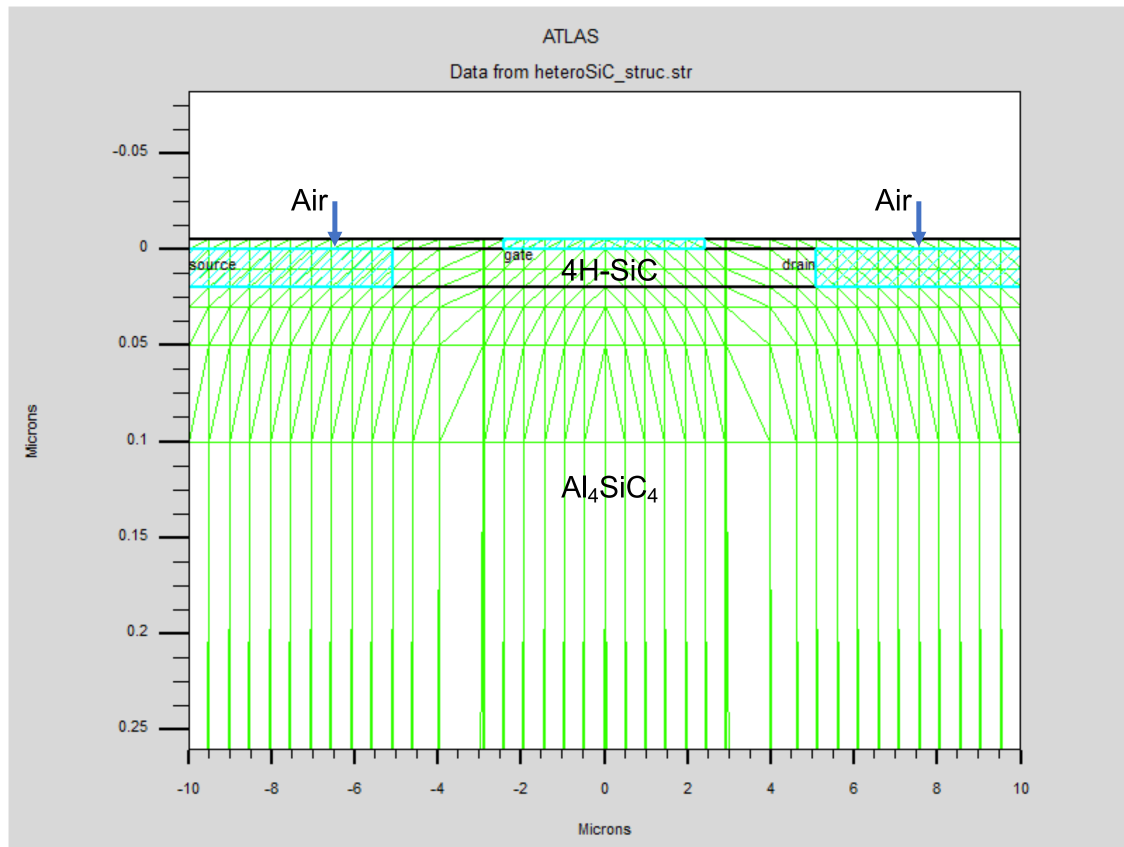

FIGURE 4.11. Example of a mesh design for a heterostructure device. Here a 5 μm gate device is shown.

erations begin with an initial guess of the solution based on analytical model using Boltzmann or Fermi-Dirac statistics. This initial guess is subsequently updated with a new estimate of the solution and the iterations continue with continuous refinement until the solution convergence criteria is met. In the simulation work, the stand alone Newton method is chosen.

Doping has to be also specified in the relevant areas of the device. The drain and the source contacts in a semiconductor device will melt in an alloy made of a metal and the ternary semiconductor (Al_4SiC_4) ideally creating a good Ohmic contact. This alloy is modelled by a heavily doped region of n-type doping in order to mimic this a good Ohmic contact at the metal-semiconductor interface [131].

4.4 Summary

This chapter over viewed the methodology of the research that was undertaken as part of this thesis. The first section of this chapter gave details on the ensemble MC simulations. The MC simulations represent the band structure of Al_4SiC_4 by considering the two lowest valleys in conduction band, the M and K valleys, and the interactions that are foreseen between the valleys playing the decisive role in the electron transport in Al_4SiC_4. The first section also gave details on the optical phonon energies and deformation potentials that have been selected. We have also derived a wave-vector transformation for the M valleys which are principal valleys in the hexagonal lattice structure of Al_4SiC_4. The material parameters used in the MC transport model are also tabulated in this section.

The second section in this chapter gave details about all the experimental research that were carried out. It first details how the spectrophotometry works by projecting light through the sample in the range of $175-3300$ nm wave lengths of which only a range of $250-1000$ nm wave lengths was used in the experiments. This narrow range of wave lengths was used because we wanted only to cover the spectrum around the absorption peak rather than to carry out the experiment of a full range of wave lengths the equipment offers.

We have outlined the geometric set up of the spectroscopy chamber. The experimental methodology employs X-Ray Photoelectron Spectroscopy (XPS) whereby monochromatic light illuminates the sample in order to ascertain details of the chemical makeup, valence band, bonds and workfunction. The final experimental set up that is detailed in this section is two- and four-probe measurements, that being a technique used to measure the I-V characteristics of a material to obtain such physical quantities as sheet resistance and Hall voltage.

The final section of the methodology details the Technology Computer Aided Design (TCAD) work that was undertaken on a heterostructure device designed using the ternary compound carbide, Al_4SiC_4, in a combination with SiC. The device simulations were carried out within commercial TCAD software Silvaco Atlas. This section details the process that the simulations take, from a specific structure design and its mesh to material models used in the TCAD simulations.

CHAPTER 5

COMPUTATIONAL RESULTS

The chapter starts with an details of the ensemble MC simulation code used to obtain the results on electron transport in the ternary carbide. The chapter then reports on the modeling by Atlas of a heterostructure High Electron Mobility Transistor (HEMT) designed using the ternary carbide. Details on transport models employed in the simulator are outlined before reporting on the device performance ending by drawing a conclusion on the device modeling results.

5.1 Monte Carlo Simulations

In this work, we have employed an in-house bulk ensemble MC simulation code to foresee electron transport properties of Al_4SiC_4. The MC simulation uses a combination of known material properties from reported experimental data and theoretical calculations using the DFT. Al_4SiC_4 has a hexagonal lattice [41–43, 50, 52, 57, 75] comprising of multiple valleys, Γ, A, L, H, M, and K, as shown in Figure 5.1(a) and 5.1(b). We will demonstrate that only the two lowest valleys, the M and K valleys, are of interest for electron transport as the occupation of all other upper valleys is negligible.

5.1.1 Electron Transport Results

This section details the results from the ensemble MC simulator starting with Figure 5.2 and 5.3 which illustrates the electron drift velocity as a function of the applied electric

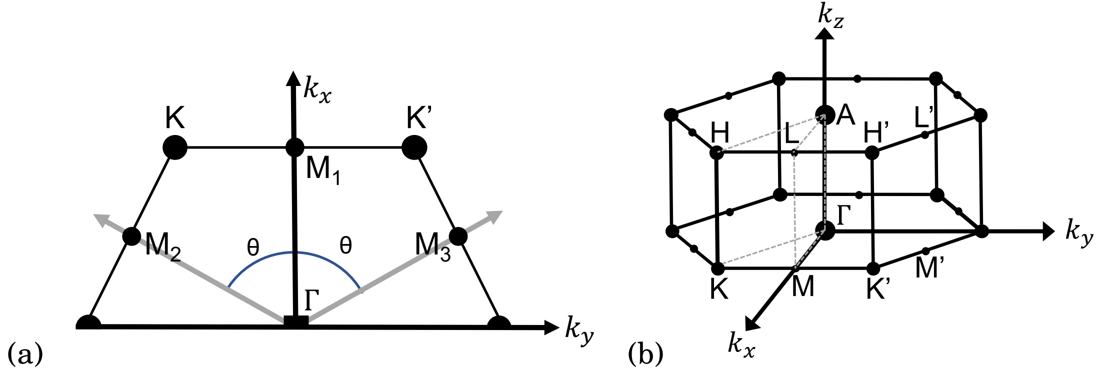

Figure 5.1: (a) 2D hexagonal (0001) plane and showing the location of the M valleys within the Al_4SiC_4 hexagonal structure, where $\theta = \pm 60°$. (b) 3D hexagonal structure showing location of principal valleys.

field. The figure shows the applied electric field in a range from 0.01 to 1400 kVcm^{-1}. The electron velocity increases with increasing electric field quickly at a relatively low electric field and starts to saturate at about electric field of 200 kVcm^{-1}. At an applied electric field of 1400 kVcm^{-1}, the maximum drift velocity is approximately 1.35×10^7 cms^{-1} at which point the electron velocity is very well saturated. This saturation is caused by a strong emission of two polar optical phonons at energies of 67 meV and 107 meV (see Table 4.2). The average kinetic energy as a function of applied electric field is plotted in Figure 5.4 and 5.5. The kinetic energy has approximately a linear increase as the electric field increases considering that electric field is plotted on a logarithmic scale.

We have monitored electron kinetic energy that is larger than the band gap of Al_4SiC_4 in the simulations. At the largest electric field of 1400 kVcm^{-1} occurring in the simulations in Figures 5.2 to and 5.5, the amounts of electrons over this energy amounts to 0.119% of the total number of electrons simulated. This indicates that electron transport in the material is close to a breakdown due to excessive impact ionisation at electric field of 1400 kVcm^{-1}. This result indicating onset of impact ionisation supports our calculated critical electric field of 1831 kVcm^{-1}.

Figures 5.6 to 5.9 show electron mobility and electron diffusion as a function of applied electric field, respectively. The electron mobility and the electron diffusion have an exponential decay as electric field increases. The electron mobility and electron diffusion at a low electric field of 5 kVcm^{-1} are 82.9 cm^2 $V^{-1}s^{-1}$ and 2.1 cm$^2s^{-1}$, which are at their respective maxima, while they are 9.63 cm$^2V^{-1}s^{-1}$ and 0.25 cm$^2s^{-1}$ at a high electric field of 1400 kVcm^{-1}, respectively. The small values of electron mobility even at a

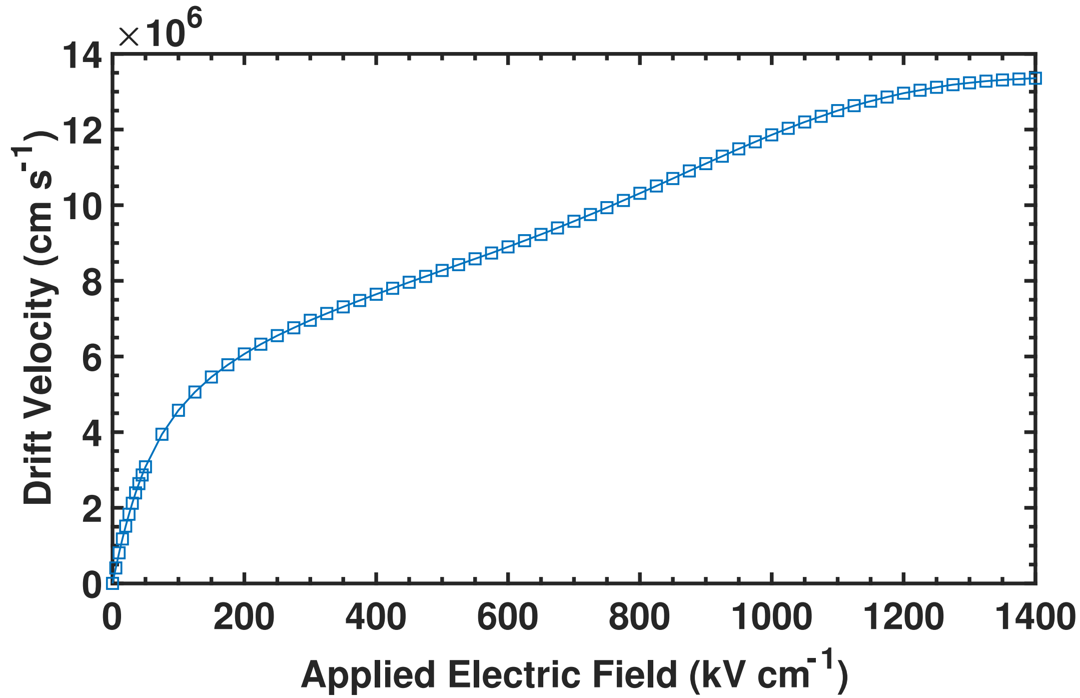

Figure 5.2: Electron drift velocity on a linear scale as a function of applied electric field in bulk Al_4SiC_4 simulated below the critical electric field

.

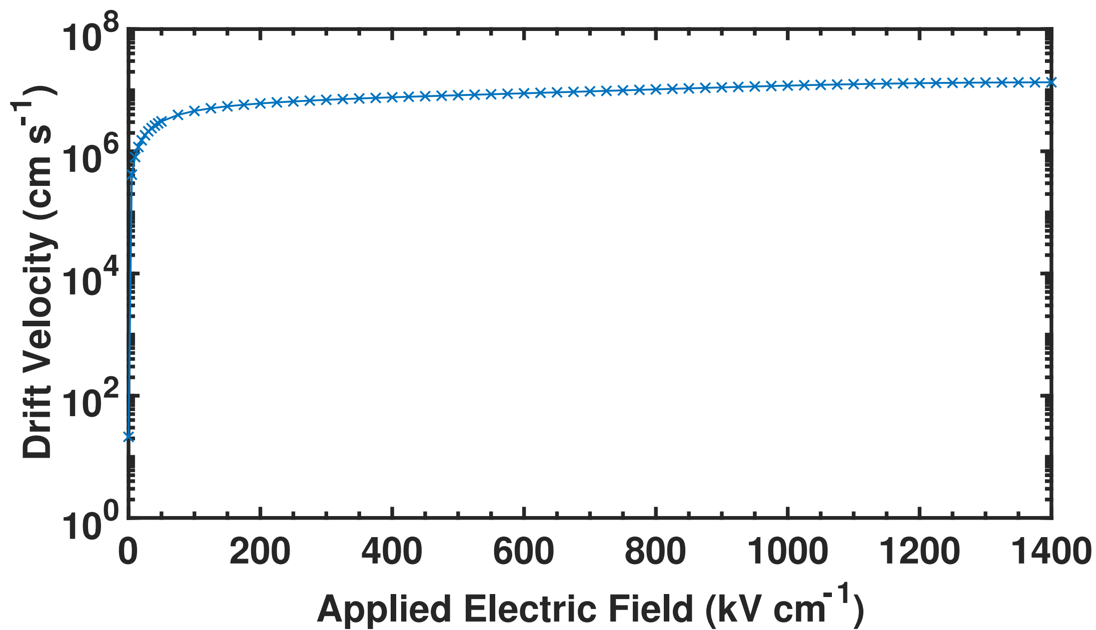

Figure 5.3: The same electron drift velocity as in Fig. 5.2 but on a logarithmic scale as a function of applied electric field in bulk Al_4SiC_4 simulated below the critical electric field.

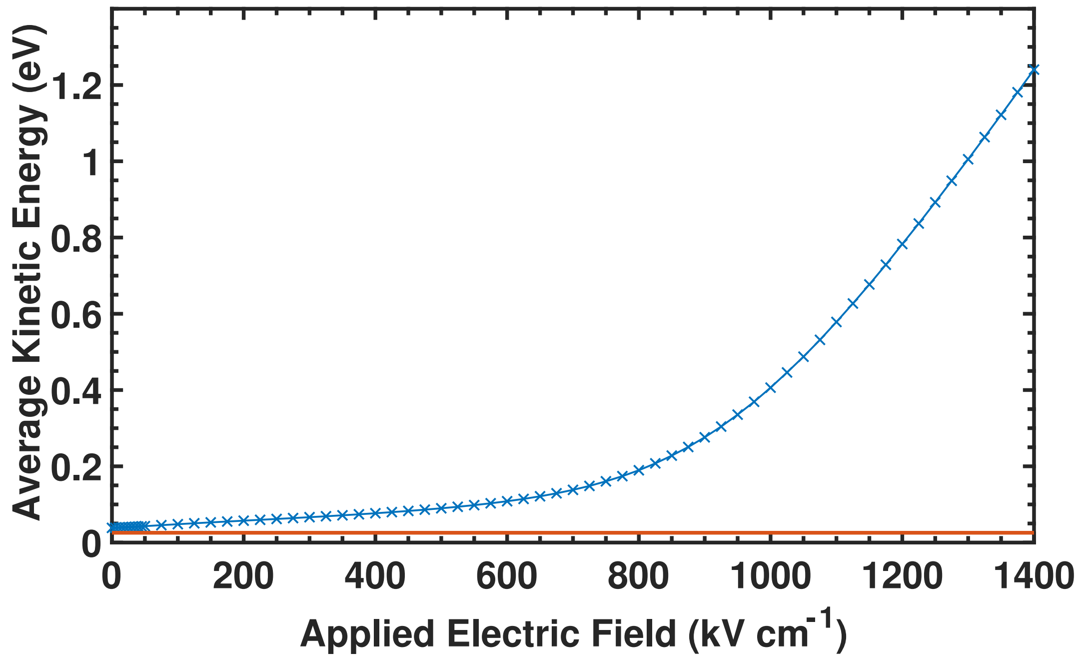

Figure 5.4: Average electron kinetic energy as a function of applied electric field in bulk Al_4SiC_4 simulated below the critical electric field. Red line show the thermal energy of electrons at 25.8 meV and the blue line the average kinetic energy of the electrons.

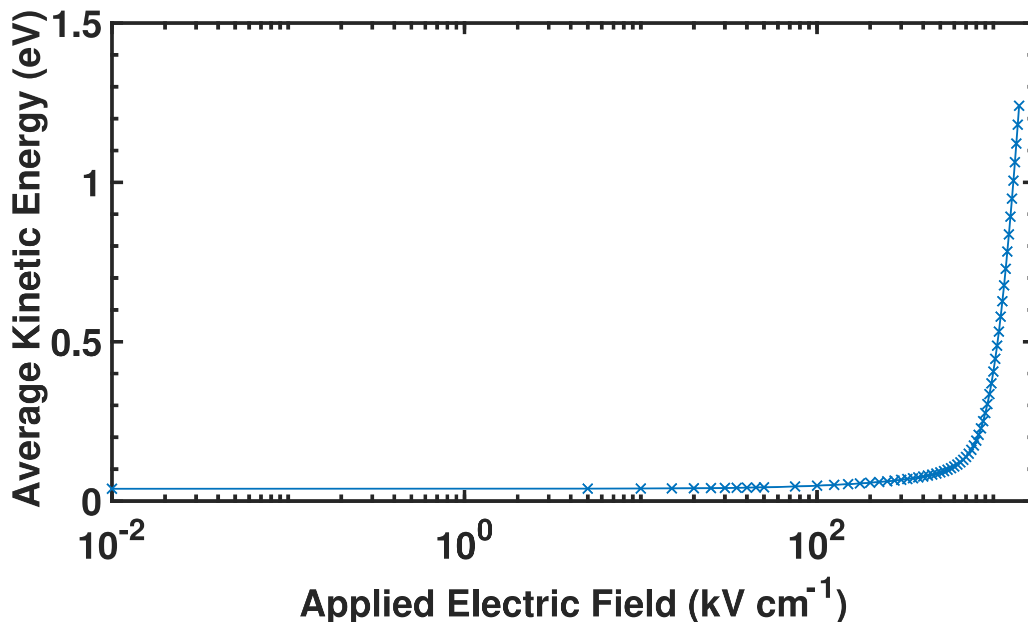

Figure 5.5: The same average electron kinetic energy as a function of applied electric field in bulk Al_4SiC_4 as in Fig. 5.4 but the field in plotted on logarithmic scale, simulated below the critical electric field.

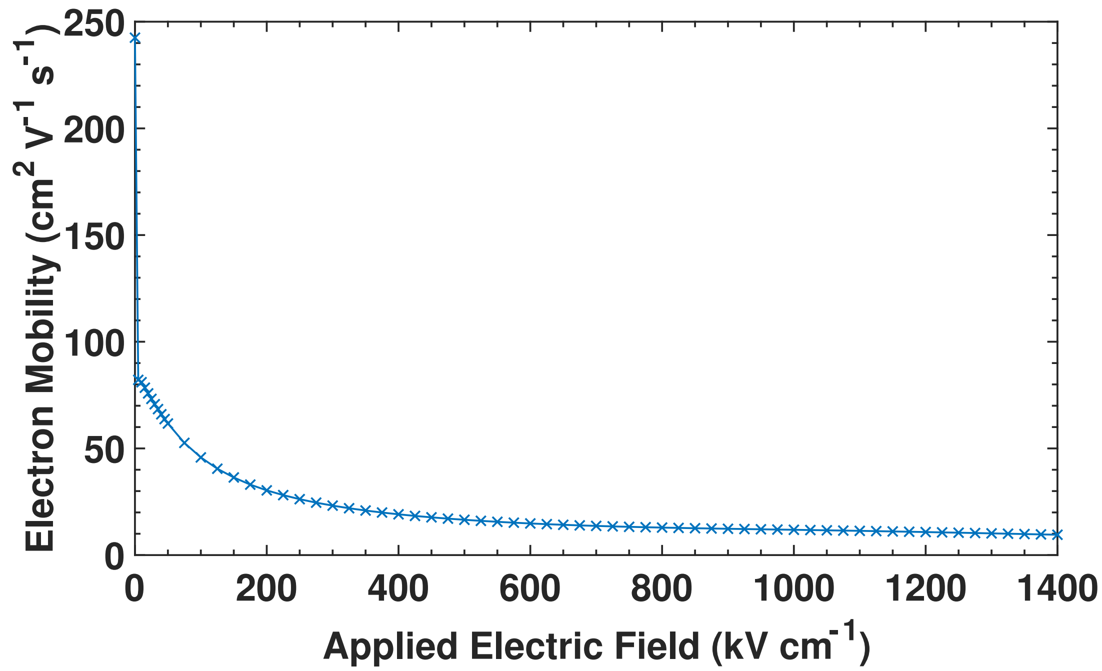

Figure 5.6: Electron mobility on a linear scale as a function of applied electric field in bulk Al_4SiC_4 simulated below the critical electric field.

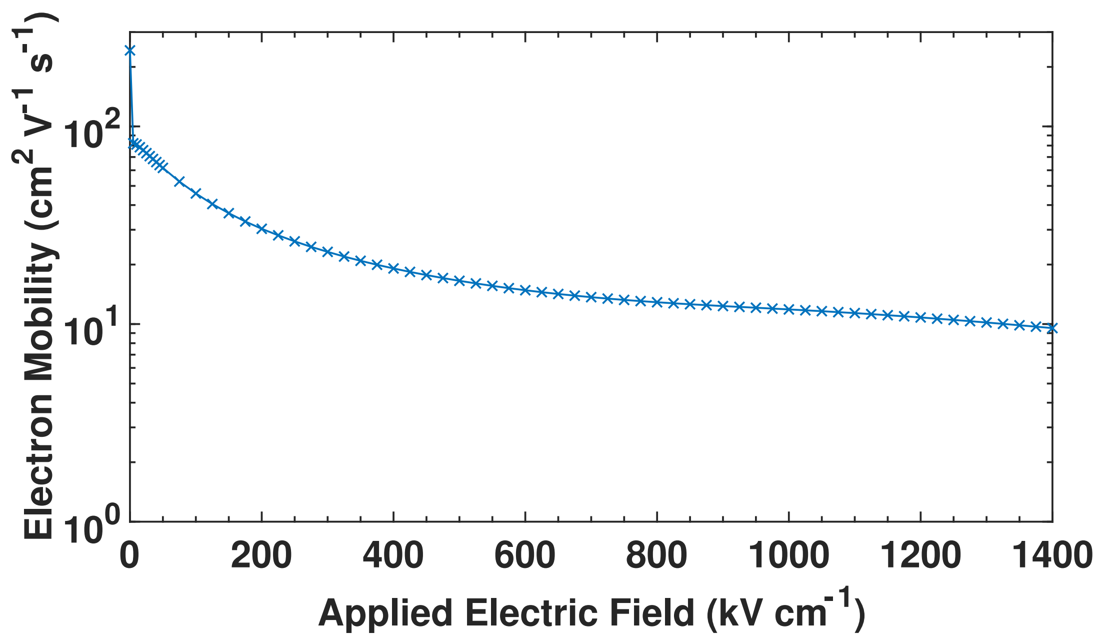

Figure 5.7: The same electron mobility as in Fig. 5.6 but on a logarithmic scale as a function of applied electric field in bulk Al_4SiC_4 simulated below the critical electric field.

low electric field are due to the large effective electron mass that has been obtained from the DFT calculations (see Table 4.2) rather than because of electron-phonon interactions.

Figure 5.10 is using a stacked plot to illustrate a population of electrons occupying each valley (M and K valleys) obtained from the MC simulations. The M valley gets populated evenly at the start of the simulation as expected until the electrons have enough energy to make a transition into the K valley. The K valley does not start to get populated until approximately 450 kVcm^{-1} but remains populated less than 20% even at the largest electric field which justifies our approximation of isotropic K-valley.

Finally, we examine the relationship between electron mobility and ionized impurity concentration in Figure 5.11. The electron mobility of Al_4SiC_4 has a typical dependency on the ionized impurity concentration when the mobility remains approximately constant until an ionized impurity concentration of 2×10^{16}cm^{-3}. When the ionized impurity concentration increases further, the electron mobility start to decline down to about 10 cm^2 $V^{-1}s^{-1}$ as seen in many semiconductor materials [125].

5.2 Device Simulations

In this work, we have employed a commercial TCAD Silvaco software by using two-dimensional (2–D) ATLAS simulations to foresee device characteristics of a SiC/Al_4SiC_4 based HEMT heterostructure for the first time. The device simulations use a combination of material properties of Al_4SiC_4 [126, 132] along with other published material properties [53]. Where material properties are unknown, we have used the material properties of 4H-SiC [133] which are well known. The initial device architecture is designed with a gate length of 5 μm to meet requirements of power applications and then scaled down to gate lengths of ≤ 100nm [121] in order to access the device potential to increase its performance, mainly to increase the switching speed by increasing transconductance. We have employed a conventional HEMT design [37] with 4H-SiC layer on top of Al_4SiC_4 buffer layer in order to promote a 2-D electron gas (2DEG) at the interface between the two materials. This is chosen to be similar to a AlGaN/GaN HEMT structure where a semiconductor with a larger band gap is placed on top of a smaller band gap semiconductor in order to make a band offset at which 2DEG is created.

This initial 5 μm gate length transistor architecture is then scaled down to explore improvement in device characteristics. The characteristics that are investigated are DC current-voltage (I-V) characteristics, transconductance, device breakdown, and a comparison between three devices scaled laterally.

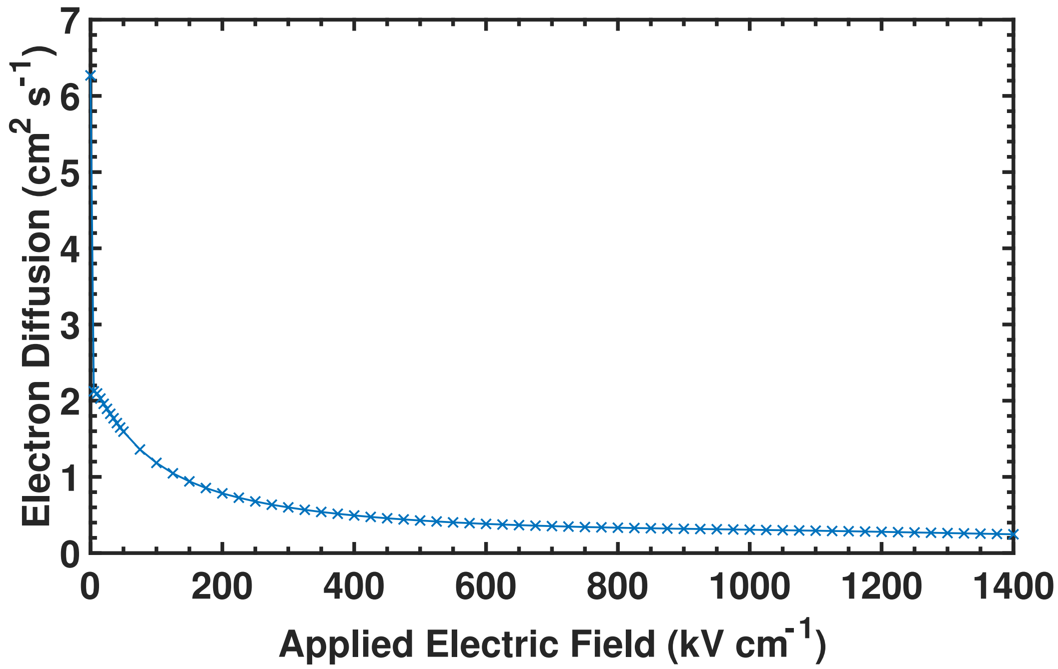

Figure 5.8: Electron diffusion as a function of applied electric field on a linear scale in a bulk Al_4SiC_4 simulated below the critical electric field.

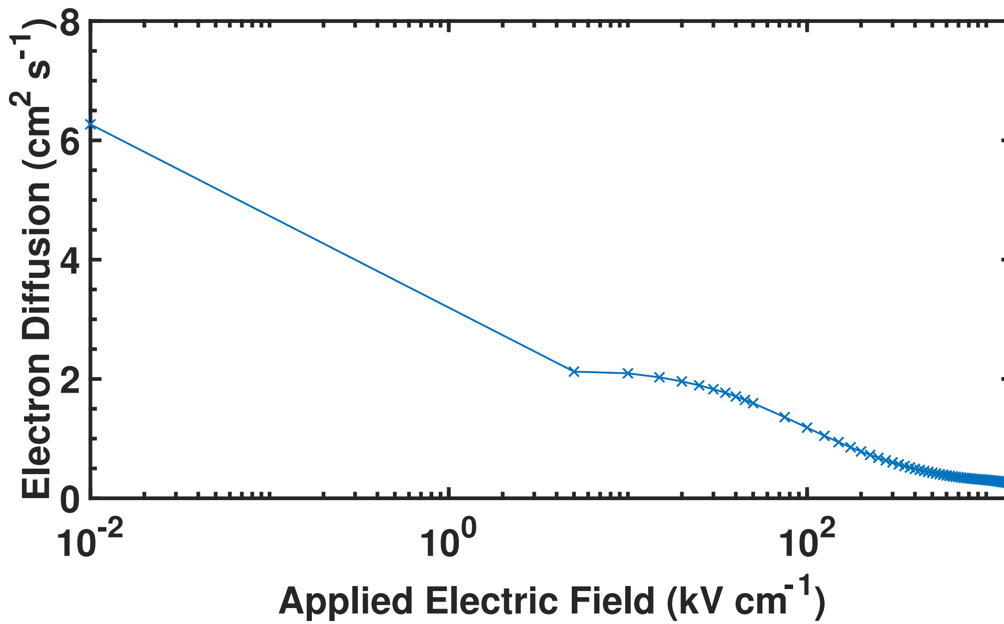

Figure 5.9: The same electron diffusion as a function of applied electric field in bulk Al_4SiC_4 as in Fig. 5.8 but on a logarithmic scale simulated below the critical electric field.

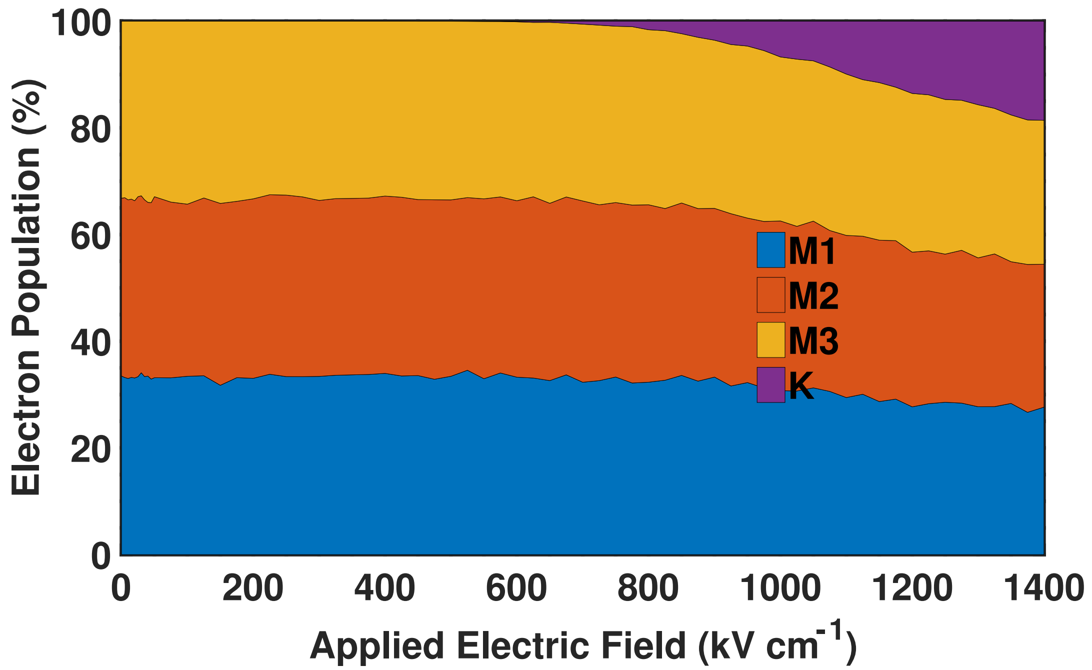

Figure 5.10: Stacked plot of the calculated valley occupancy of electrons in the three M and K valleys as a function of applied electric field in bulk Al_4SiC_4.

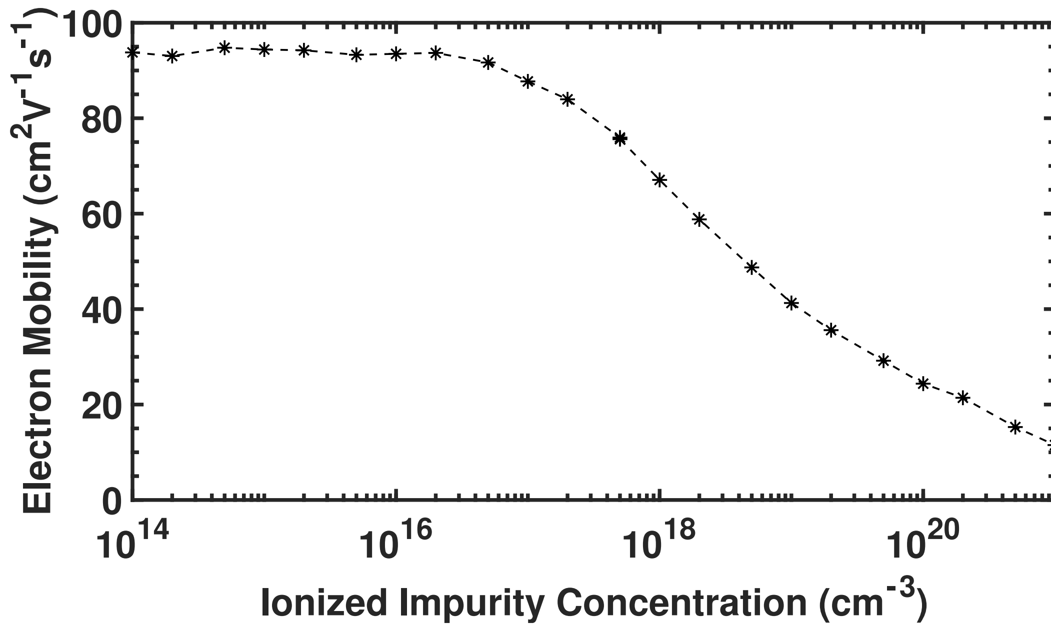

Figure 5.11: Electron mobility as a function of ionized impurity concentration in bulk Al_4SiC_4 at an applied electric field of 1 kV/cm.

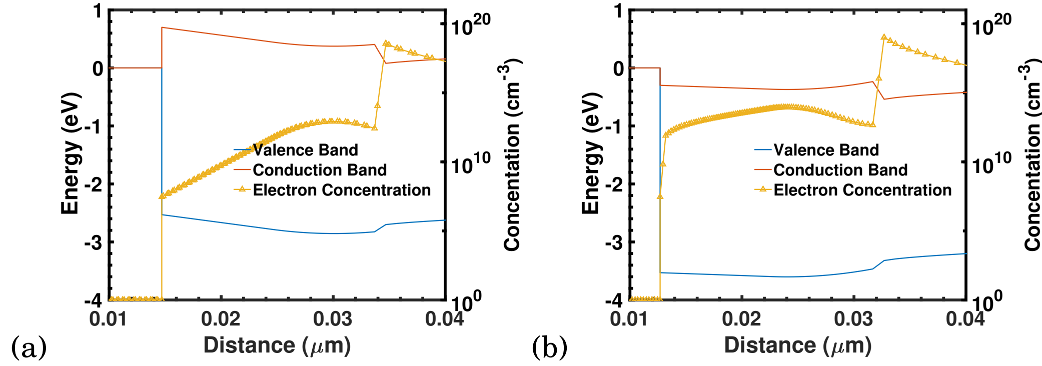

Figure 5.12: Conduction and valence band profiles (left) overlapped with electron density (right) across the middle of the 5 μm gate length device in an off-state with zero bias applied (a), and in an on-state at V_D=5 V and V_G=1 V (b).

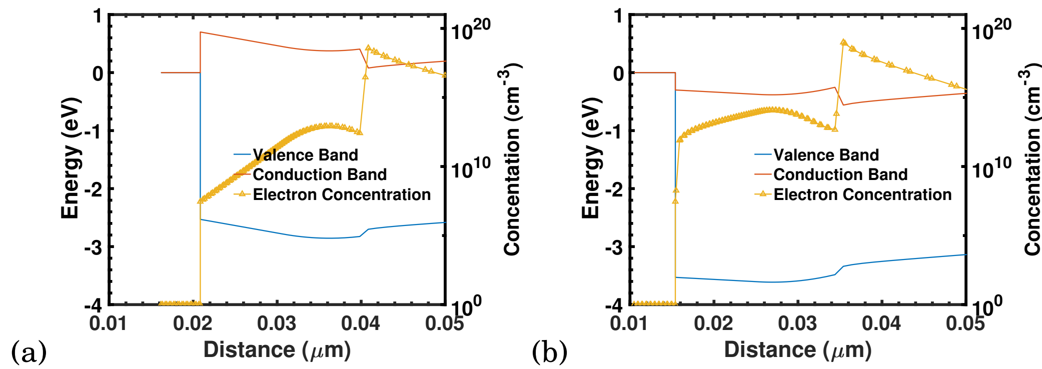

Figure 5.13: Conduction and valence band profile (left) overlapped with electron density (right) across the middle of the 2 μm gate length device in an off-state with zero bias applied (a), and in an on-state at V_D=5 V and V_G=1 V (b).

5.2.1 Transistor Simulations

Figures 5.12 to 5.14 show the conduction and valence band profiles with overlap of the electron concentrations in off and on conditions. When the device is in the off state, that is when zero bias is applied, the Fermi level is located between the conduction band and the valence band. When in the on state, that is when an bias of V_D=5 V and V_G=1 V is applied, the Fermi level shifts up so that the level is located within the conduction band of the device and the electron concentration increases by a factor of six creating a 2DEG at the interface between 4H-SiC and Al_4SiC_4 due to the bandgap offset of the two semiconductors.

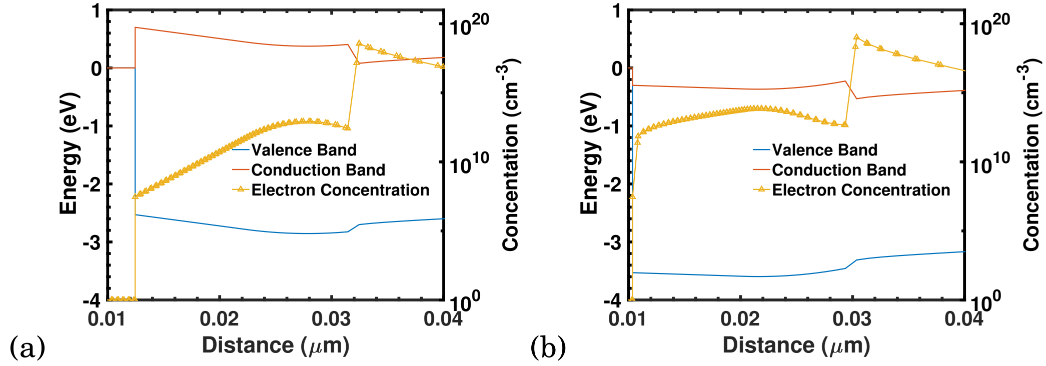

Figure 5.14: Conduction and valence band profile (left) overlapped with electron density (right) across the middle of the 1 μm gate length device in an off-state with zero bias applied (a), and in an on-state at V_D=5 V and V_G=1 V (b).

5.2.2 Device Structure

The 2–D device simulator Atlas by Silvaco is used here to investigate a designed heterostructure transistor for power applications as see in Figure 5.15. The device heterostructure, which has been optimised for a large channel electron density, comprises of a thin layer of n-type doped 4H-SiC with a concentration of $2.5 \times 10^{18} cm^{-3}$ on a top of large layer of p-type doped Al_4SiC_4 with a concentration of $1 \times 10^{16} cm^{-3}$. The purpose of the thin layer of n-type doped SiC is to provide supply of carriers into the device channel which occurs at the interface between the SiC and the Al_4SiC_4 because of the off set in their conduction bands. A n-type doping concentration of $2.5 \times 10^{18} cm^{-3}$ was chosen as this had been optimised by looking at the sheet resistance as a function of n-type doping concentration. The SiC/Al_4SiC_4 heterostructure device has a gate length of 5 μm, a channel length from source-to-drain of 10 μm, a source-to-gate distance of 2.5 μm and a gate-to-drain distance of 2.5 μm. The thickness of the layers is fixed to 20 nm for SiC and to 3 μm for Al_4SiC_4.

The initial 5 μm gate length SiC/Al_4SiC_4 heterostructure transistor is laterally scaled to gate lengths of 2 μm (4 μm channel length from the source to the drain) and 1 μm (2 μm channel length from the source to the drain). The source-to-gate and the gate-to-drain dimensions are scaled to 1 μm for the 2 μm gate length device and to 0.5 μm for the 1 μm gate length (see Table 5.1).

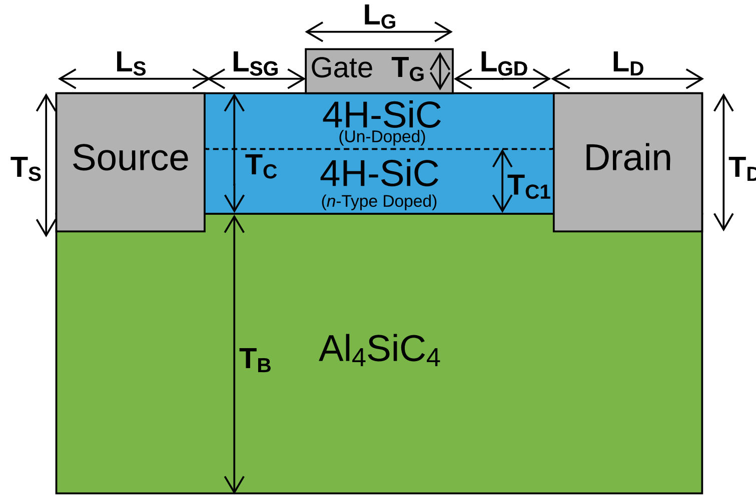

Figure 5.15: Cross-section of the heterostructure SiC/Al_4SiC_4 transistor designed for power applications, see Table 5.1 for dimensions. The concentration of n-type doped 4H-SiC layer is $2.5 \times 10^{18} cm^{-3}$.

Thickness (nm)	Gate length (nm)		
	5000	2000	1000
Source-to-gate spacer (L_{SG})	2500	1000	500
Gate-to-drain spacer (L_{GD})	2500	1000	500
Source thickness (T_S)	25	25	25
SiC as barrier (T_C)	20	20	20
SiC n-type layer (T_{C1})	10	10	10
Al_4SiC_4 as buffer (T_B)	3000	3000	3000
Gate thickness (T_G)	5	5	5
Drain thickness (T_D)	25	25	25

Table 5.1: Corresponding dimensions of the scaled heterostructure transistors shown in Figure 5.15. Note that L_S and L_D dimensions in Figure 5.15 are assumed to be a large enough to make good Ohmic contacts.

5.2.3 Device Model

All simulations were done in SILVACO ATLAS 2D V5.26.1.R using a 2D drift-diffusion transport model with field dependent mobility [40] and Auger recombination [40] simulating both holes and electrons. The solution technique that is used by the simulations is the combined Gummel-Newton algorithm. The material parameters for Al_4SiC_4 are

summarized in Table 5.2.

Parameter (unit)	Value
Electron mobility (cm^2/Vs)	242.5 [a]
Electron saturation velocity (cm/s)	8×10^6 [a]
Bang gap at 300°C (eV)	2.78 [a]
Permittivity	8.32 [b]
Affinity (eV)	3.546 [a]
Conduction band density at 300°C (cm^{-3})	7.887×10^{19} [a]
Valence band density at 300°C (cm^{-3})	1.2×10^{19} [a]
Electron recombination coefficient	5×10^{-31} [c]
Hole recombination coefficient	2×10^{-31} [c]

[a]Calculated from previous works [132] [b]Ref. [53] [c]Ref. [134]

Table 5.2: Al_4SiC_4 material parameters considered in the simulations of heterostructure transistors. The electron mobility is calculated at an applied electric field of 0.01 kV/cm.

5.2.4 Scaled SiC/Al_4SiC_4 Heterostructure Transistors

The $I-V$ characteristics of each heterostructure transistor are simulated for a gate bias (V_G) from 0 V to 20 V, and for the drain bias (V_D) from 1 V to 40 V as depicted in Figures 5.16-5.18. When V_D is increased, the drain current starts to saturate due to a limitation of the maximum electron density in the channel which is determined by the conduction band offset as seen in Figures 5.12–5.14. The drain current saturation exhibits itself as inability to substantially increase saturation current at higher V_D (between 15 V to 40 V). The $I_D - V_G$ characteristics show a linear region, an on-set of the saturation, and a saturation region. At V_D = 40 V, the complete drain current saturation occurs determining the maximum drain current which a scaled transistor can deliver at approximately 1.68×10^{-4} A/μm, 2.44×10^{-4} A/μm, and 3.50×10^{-4} A/μm for gate lengths of 5 μm, 2 μm, and 1 μm, respectively. The decrease in maximum current on the devices is due to the distance between the source and the drain. The further the electrons have to travel the lower the current. On the 5 μm we see a slight decline in the current saturation region of the slop which is most likely cased by self-heating in the device. We also see current crowing at high drain voltage. This is due to the drain voltage being saturated and therefore impacting on the drain current less causing a smaller and smaller shift between the drain current saturation regions.

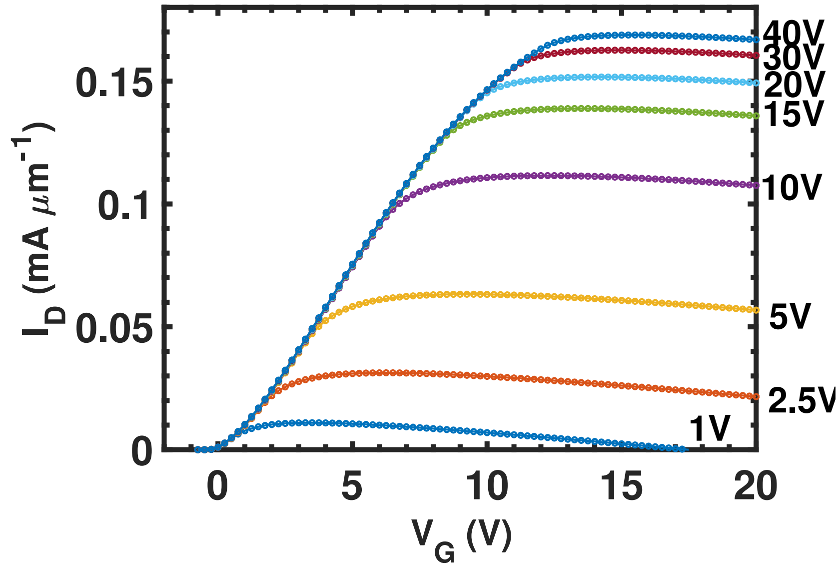

Figure 5.16: $I_D - V_G$ characteristics at indicated drain biases (V_D) for the 5 μm gate length SiC/Al_4SiC_4 heterostructure transistor.

The metal-gate workfunction that is used in the simulations is taken to be 3.9 eV. The threshold voltage is determined from the $I_D - V_G$ characteristics where a linear fit is taken against the linear region of the data. The threshold voltage is found to be 71.0 mV, 28.3 mV, and 28.3 mV for a 5 μm, 2 μm, and 1 μm gate length transistors, respectively. This decrease in threshold voltage is caused by an increase in electron density leading way to an easier accumulation of electrons. The sub-threshold slope has been extracted from the $I_D - V_G$ characteristics on a semi-logarithmic scale by fitting a linear line at a low drain bias of $V_D = 5$ V. The sub-threshold slope is 197.3 mV/dec, 97.6 mV/dec, and 96.1 mV/dec for devices with gate lengths of 5 μm, 2 μm, and 1 μm, respectively, all of which are much larger than the ideal sub-threshold slope of 60 mV/dec [135, 136].

Breakdown of the devices is determined from simulated $I_D - V_D$ characteristics seen in Figures 5.19-5.20 when the transistors are off. The bias at which the device breaks down becomes smaller as the gate length decreases, 59.0 V, 31.0 V, and 18.0 V for gate lengths of 5μm, 2μm, and 1μm, respectively. The 5 μm gate length heterostructure transistor exhibits a non-equilibrium stage between holes and electrons in a form of a kink in its $I_D - V_D$ characteristics at approximately 35 V followed by the device breakdown at 59.0 V. The kink and the device breakdown voltage, when the drain current sharply rises, is seen in Figure 5.19. A similar kink is seen in the 2 μm gate length heterostructure transistor where a sharp rise occurs at approximately 25 V followed by the device breakdown at

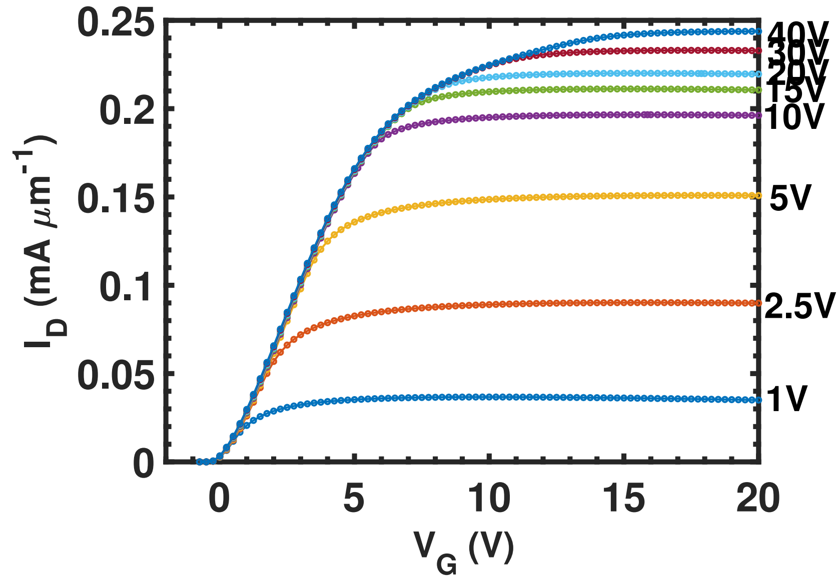

Figure 5.17: $I_D - V_G$ characteristics at indicated drain biases (V_D) for the scaled SiC/Al_4SiC_4 heterostructure transistor with a 2 μm gate length.

31.0 V (see Figure 5.20). No kinks appear in the smallest gate length device where the breakdown voltage occurs at 18.0 V (see Figures 5.21).

Finally, we extract transconductance at a low drain bias of 2.5 V and a high drain bias of 30 V in order to ascertain how well the device will be performing in a switching operation. As the device gate length decreases, the transconductance increases from 1.25 mS/mm (1.69 mS/mm) to 31.90 mS/mm (36.5 mS/mm) and 59.3 mS/mm (65.1 mS/mm) at a low drain bias of 2.5 V (at a high drain bias of 30 V) as summarized in Table 5.3 and, in turn, the switching speed of the device will improve. This increase in switching speed is caused by the gate-source capacitance, which is roughly the same as between the gate and the channel. This means that as the gate dimension become smaller, the smaller the capacitance and thus faster switching. The decline of the transconductance in the 1 μm gate length transistor at the high drain bias of 30 V is caused by a kink at around 13 V at a drain bias of 30 V detectable in the $I_D - V_G$ characteristics shown in Figure 5.18. The kink separates two transport regimes in the transistor operation. The first transport regime is a standard electron accumulation in the channel giving linear regime of the $I_D - V_G$ characteristics. The second transport regime occurs when additional channel is created by electrons spilling into a conduction band minimum in the SiC layer (see the conduction band in the SiC layer in Figure 5.14(b)).

On top of proportional lateral scaling of the device, we also performed asymmetric

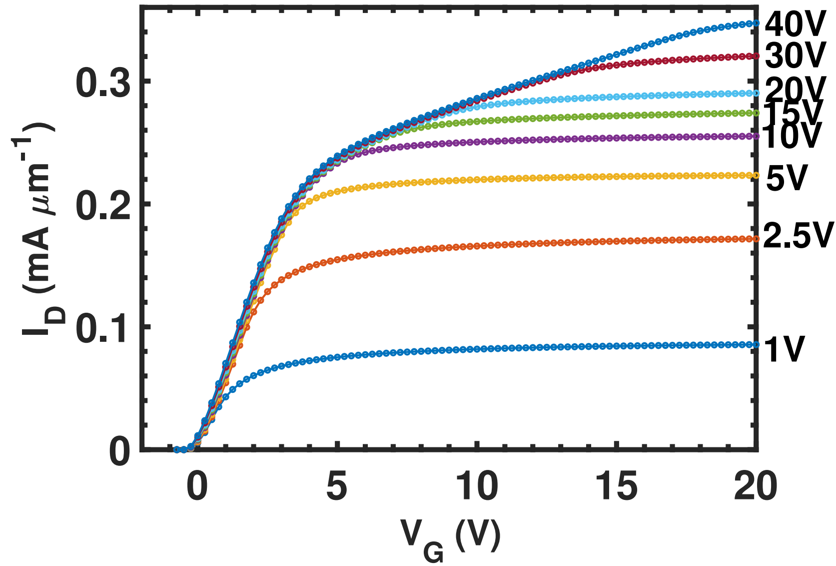

Figure 5.18: $I_D - V_G$ characteristics at indicated drain biases (V_D) for the scaled SiC/Al_4SiC_4 heterostructure transistor with a 1 μm gate length.

scaling, as this is common practice [13, 14, 137], on the 2.0 μm gate length heterostructure, where we increased the gate-to-drain spacer to 2.5 μm in order to re-distribute high electric field occurring between the gate and the drain along the longer distance and thus lower the field when transistor architecture is scaled laterally from a gate length of 5 μm gate to 2 μm and 1 μm. The rest of device sizes stayed the same as per Table 5.1. This asymmetric heterostructure transistor design delivers a breakdown voltage increased by 17.25 V, that is from 31.0 V to 48.25 V. We also look at increasing the breakdown voltage of the 1 μm gate length heterostructure transistor by creating an asymmetric design of the device where the source-to-gate spacer is fixed to 0.5 μm but the gate-to-drain spacer is increased to 1.0 μm and to 2.5 μm. The 1 μm gate length asymmetric heterostructure with a 1.0 μm gate-to-drain spacer exhibits an increase in the breakdown voltage of 4.75 V, that is from 18.0 V to 22.75 V. The 1 μm gate length asymmetric heterostructure with a 2.5 μm gate-to-drain spacer exhibits an increase in the breakdown voltage of 11.25 V, that is from 18.0 V to 29.25 V. Therefore, lateral scaling of the SiC/Al_4SiC_4

Drain Bias (V)	5 μm	2 μm	1 μm
2.5	1.25 $\times 10^{-6}$ S/μm	3.19 $\times 10^{-5}$ S/μm	5.93 $\times 10^{-5}$ S/μm
30	1.69 $\times 10^{-6}$ S/μm	3.65 $\times 10^{-5}$ S/μm	6.51 $\times 10^{-5}$ S/μm

Table 5.3: Maximum transconductance of the scaled heterostructure transistors.

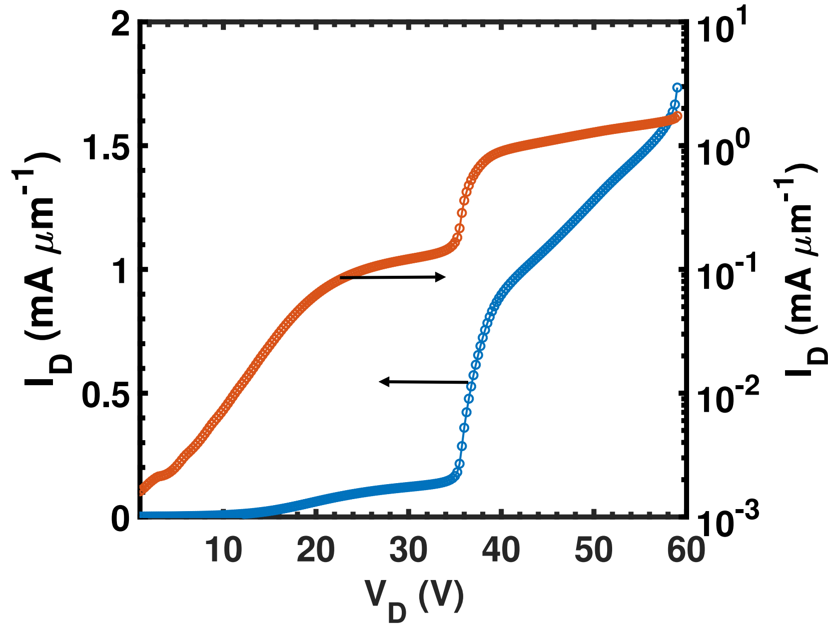

Figure 5.19: Breakdown of 59.0 V for a heterostructure device at a $V_G = 0$ with a 5 μm gate length on a linear scale (left) on a log scale (right)

heterostructure transistor can deliver increase in the device transconductance. However, a consequence of the lateral scaling, which induces an increase in the electric field in the device heterostructure because a decrease in the source-to-gate and the gate-to-drain distances, is also a decrease in the device breakdown voltage. This breakdown decrease can be mitigated by using asymmetric device structure where the distance between the gate and the drain is increased. However, this increase in the breakdown voltage is still small compared to a AlGaN/GaN HEMT at 600 V [13].

5.3 Discussion

The ensemble MC simulations of the electron transport in Al_4SiC_4, which has a hexagonal crystal structure, have been enhanced by including a rotational transformation in the lowest conduction band, the M valley, to consider a strong anisotropy of the bandstructure. The strong anisotropy of the electron effective mass in the M valley has profound impact on electron drift velocity and mobility. The electron effective mass extracted from DFT calculations have shown that there is a large effective mass in both the longitudinal and transverse directions in the K valley of 1.0569 m_e and 0.9360 m_e, respectively, compared with those in the M valley of 0.5678 m_e and 0.6952 m_e, respectively.

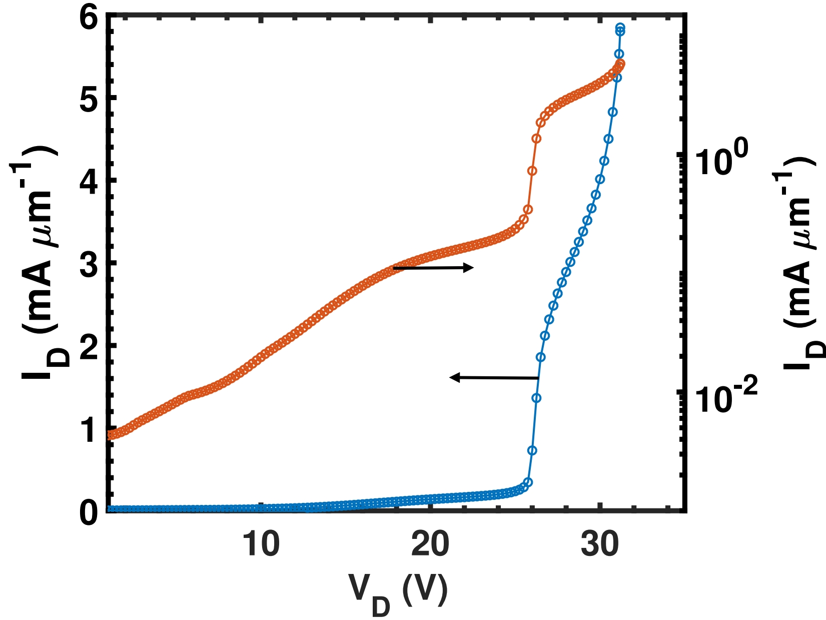

Figure 5.20: Breakdown of 31.0 V for a heterostructure device at a $V_G = 0$ with a 2 μm gate length on a linear scale (left) on a log scale (right).

The MC simulations allows to predict material transport properties in Al_4SiC_4. We have predicted dependence of electron drift velocity, electron mobility, average kinetic energy of electrons, and electron population against the applied electric field, all of which can serve as crucial indicators to assess the electronic and opto-electronic performance of devices. We have shown that the electron drift velocity increases with increasing electric field reaching 1.35×10^7 cms^{-1} at approximately 1400 kVcm^{-1}. The electron kinetic energy has a linear increase as expected and reaches 1.24 eV at 1400 kVcm^{-1}. The threshold energy barrier when electrons start to transfer from the M valley to the K valley occurs at electric field of approximately 450 kVcm^{-1}. We predict that as the number of electrons with high kinetic energy, that is larger than the band gap of the material, will start to increase rapidly as the applied electric field draws closer to the critical field of 1831 kVcm^{-1} causing a breakdown to occur.

The electron mobility decreases with an increase of the electric field from approximately 242.5 cm^{2}V^{-1}s^{-1} to 9.6 cm^{2}V^{-1}s^{-1} and the diffusion constant decreases from approximately 6.27 to 0.25 cm^{2}s^{-1}, both over a range of very low electric field to 1400 kVcm^{-1}. Finally, we have shown that the electron mobility dependent on the ionized impurity concentration declines from its maximum value of 93.8 cm^{2}V^{-1}s^{-1} at low doping concentrations up to 2×10^{16}cm^{-3} to about 10 cm^{2}V^{-1}s^{-1} at a very high doping

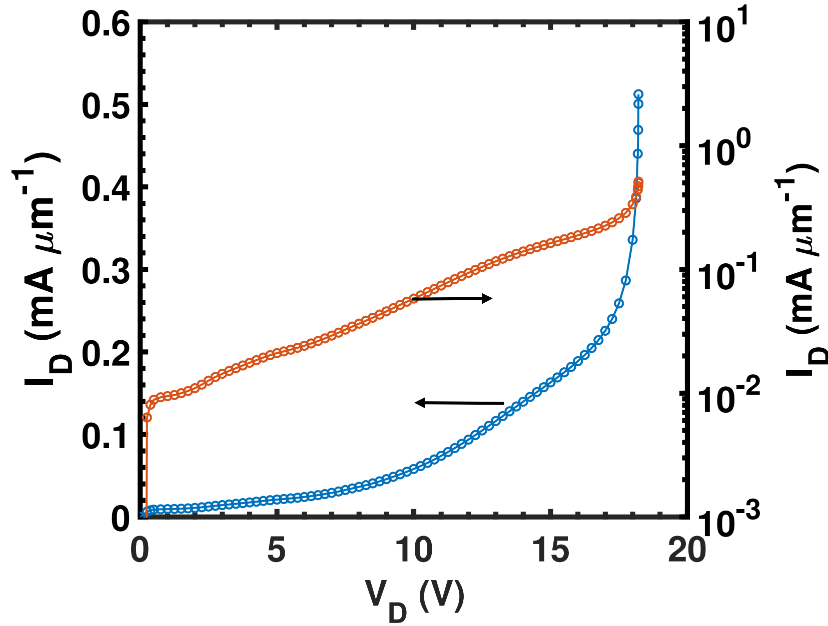

Figure 5.21: Breakdown of 18.0 V for a heterostructure device at a $V_G = 0$ with a 1 μm gate length on a linear scale (left) on a log scale (right).

concentration of 10^{21}cm^{-3}. These predicted material properties show a limited usage of the Al_4SiC_4 in a channel of potential metal-oxide-semiconductor field effect transistors (MOSFETs) due to a maximum drift velocity and electron mobility of 1.35×10^7 cm s^{-1} and 242.5 cm^{2}V^{-1}s^{-1}, respectively. When comparing these two material properties of Al_4SiC_4 with properties of known semiconductor materials, a maximum drift velocity of Al_4SiC_4 is only 61.4 % of the maximum drift velocity of GaN (2.2×10^7 cm s^{-1}) and electron mobility of Al_4SiC_4 is 19.4 % of the GaN electron mobility (2DEG) (1250 cm^{2}V^{-1}s^{-1}) [138]. Compared to 6H-SiC, Al_4SiC_4 is only 67.5 % of the maximum drift velocity of 6H-SiC (2×10^7 cm s^{-1}) and only 48.5 % of the 6H-SiC electron mobility (500 cm^{2}V^{-1}s^{-1}) [138]. Finally, comparing to silicon, Al_4SiC_4 is 135 % of the maximum drift velocity of silicon (1×10^7 cm s^{-1}) and only 16.17 % of the silicon electron mobility (1500 cm^{2}V^{-1}s^{-1}) [138].

These small values of electron mobility and drift velocity that we have seen in these simulations come from the large electron effective mass that was extracted from the DFT calculations of L. Pedesseau et. al. [52]. The results here would also differ slightly if we simulated along a different plane. This is due to the effective masses being slightly anisotropic, see Table 4.2. For instance, we have a longitudinal effective mass of $0.5678m_e$ and a transverse effective mass of $0.6952m_e$ in the M valley.

A performance of heterostructure transistor made of SiC/Al_4SiC_4 material system with a novel ternary carbide of Al_4SiC_4 has been simulated in Silvaco Atlas using known experimental [126] and theoretical data [132]. The heterostructure transistor with a gate length of 5 μm and two heterostructure transistors laterally scaled to gate lengths of 2 μm and 1 μm with respective lateral scaling of source-to-gate distance, channel length, and gate-to-drain distance have been simulated using a drift-diffusion transport model in commercial simulator Atlas by Silvaco. The variants of asymmetric scaled heterostructure transistors with the increased gate-to-drain distance to achieve a larger breakdown voltage have been also studied.

The threshold voltage reduces as the gate length is reduced from 71.0 mV to 28.3 mV, and to 28.3 mV for 5 μm, 2 μm, and 1 μm gate length transistors, respectively, when a metal gate workfunction in the SiC/Al_4SiC_4 HEMT is assumed to be 3.9 eV. Therefore, the device remains off unless a gate bias is applied and all the scaled SiC/Al_4SiC_4 heterostructure transistors provide a n-channel enhancement-mode, normally-off device operation. Sub-threshold voltages of 197.3 mV/dec, 97.6 mV/dec, and 96.1 mV/dec for gate lengths of 5 μm, 2 μm, and 1 μm, respectively, are observed which are, in all cases, much larger than the ideal value of 60 mV/dec at 300 K. This sub-threshold voltage is also higher than the 54 mV that is observed in some AlGaN/GaN HEMTs [139].

The bias point at which the device breakdown occurs reduces from 59.0 V, to 31.0 V, and to 18.0 V as the gate length reduces from 5 μm to 2 μm and to 1 μm, respectively. These breakdown voltages for SiC/Al_4SiC_4 heterostructure transistors are much lower than what is seen for AlGaN/GaN HEMT at between 90 V [140] to 600 V [13]. The breakdown voltage can be increased to 48.25 V when we increase the gate-to-drain spacer to 2.5 μm in the 2 μm gate device, and to 22.75 V and to 29.25 V in the 1 μm gate device when the gate-to-drain spacer is increased to 1.0 μm and to 2.5 μm. The drain current saturation point increases with the reduction of the gate length and increase of the drain voltage. At a large drain voltage of 40 V, a drain current saturation appears at 1.68×10^{-4} mA/mm, 2.44×10^{-4} mA/mm, and 3.50×10^{-4} mA/mm for gate lengths of 5 μm, 2 μm, and 1 μm, respectively.

A good figure of merit for such HEMTS is transconductance which relates the current through an output to the voltage across the input of a device. This is useful as it shows the switching speed of a device and how quickly a signal can be transmitted through the device. The higher the transconductance the better the performance of a device. In all cases, the maximum transconductance that has been observed is much smaller that for a AlGaN/GaN HEMT which sees values of 120 mS/mm [14] compared to our best

result, which is in the 1 μm gate device at a drain bias of 30 V, which shows highs of 0.6.51 μS/μm.

Chapter 6

Experimental Results

This chapter is organised as follows. It starts with an introduction into the various experimental methods that were used to characterise Al_4SiC_4. Section 6.2 introduces the UV/Vis/NIR spectroscopy experiments and details the results. Section 6.3 looks at the XPS experiments that were carried out, detailing the results obtained from them. Section 6.4 looks at the final group of experiments that were performed, these being two- and four-probe DC current voltage measurements and again details the results obtained. Finally, Section 6.5 draws a conclusion from all the experiments.

6.1 Introduction

In this work, a multitude of experiments have been carried out in order to characterise Al_4SiC_4, these being UV/Vis/NIR Spectroscopy, X-Ray Photoelectron Spectroscopy (XPS) and two- and four-probe DC current voltage characterisation. Each of these techniques work off different physical principles of which have been detailed in Chapters 3 and 4. Two sets of samples have been used in these experiments. One sample has been prepared by the fabrication method using solution grown crystals of Al_4SiC_4 [42] and second sample by the fabrication method using sublimation grown crystals of Al_4SiC_4 [141]. Both of these samples have been provided by Grenoble University for use in this joint research thesis.

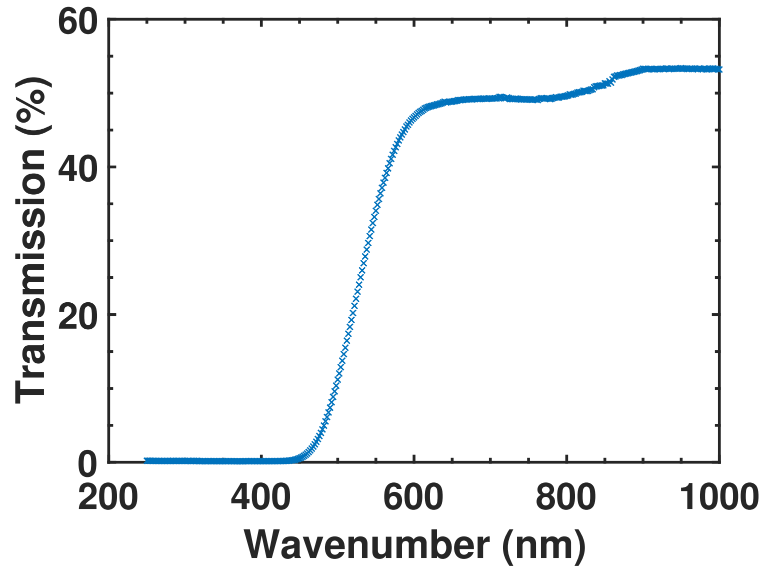

FIGURE 6.1. Wave-number as a function of the light transmission through the solution grown sample of Al_4SiC_4 obtained from the UV/Vis/NIR spectroscopy.

6.2 UV/Vis/NIR spectroscopy

Solution grown samples [42] are used in the UV/Vis/NIR spectroscopy due to the requirements of the spectroscopy system needing to be able to transmit light through a sample. This experiment was performed on the Perkin Elmer Lambda 950 spectrophotometer at LMGP, Grenoble University. These sample were prepared by cleaning them in isopropanol and acetone for 5 minutes each in a sonic bath. The samples are then attached individually to an aperture on the spectrophotometer. The light of wavelengths ranging from a 250 nm to 1000 nm is shone at them and the transmitted light is measured. The measured transmitted light is plotted as a function of wave-number in Figure 6.1. Figure 6.1 shows around 50% transmission over a wavelength of 600 nm before a rapid decrease in transmission down to 0% at 450 nm. Therefore, the sample starts to absorb the transmitted light at 600 nm before total absorption is seen from 450 nm down to 250 nm.

The data collected from the spectrophotometer, see Figure 6.1, is then converted to optical absorption ($\alpha h\nu$), using the Beer-Lambert's Law details in Section 3.4, and incident photon energy using $E = h\nu$ to form a Tauc plot. The Tauc plot can be used to extract a bandgap as illustrated in Figure 6.2. The black dotted region in the plot, often referred to as Urbach tailing [142], serves to ascertain a bandgap for the material.

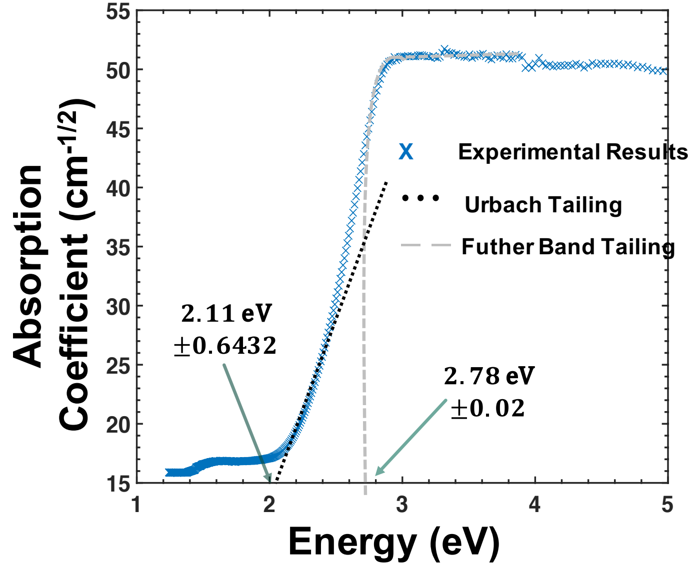

FIGURE 6.2. Tauc plot showing photon energy as a function of absorption coefficient, showing a best fit to the Urbach tail giving a bandgap of 2.11 eV, as well as further band tailing giving a bandgap of 2.78 eV.

However, in our case, the Urbach tailing results in a band gap of only 2.11 ±0.643 eV. According to computational works from the literature review [52], the bandgap should be at least 2.4 eV. By taking further band tailing into account, we reveal a bandgap of 2.778 ±0.02 eV leading way to a $\alpha = b(E_{ph} - E_0)^2$ relationship, where $b = 35$, E_{ph} is the photon energy and E_0 is the absorption edge, in this case 2.778 eV. This further band tailing can be explained through several means such as doped or defective material. Further details on the band tailing are in Sections 3.5 and 3.6. This measured bandgap is in line with Valence Electron Energy-Loss Spectroscopy (VEELS) experiment that was undertaken on our behalf at the University of Cadiz and published in various posters [126, 143, 144]. They revealed a bandgap of 2.8 ±0.2eV.

A similar band tailing effect occurs also in GaAs. When GaAs becomes doped, its bandgap reduces as reported in Ref. [145]. The Tauc plot in the reference shows a larger effect on the band tailing for the p-type doped GaAs than the n-type doped GaAs. This would suggest that Al_4SiC_4 has an unintentional p-type doping because we observe the similar larger band tail in our experimental works.

A larger bandgap has been seen extracted from experimental measurements using the UV/Vis/NIR Spectroscopy when compared to DFT calculations from literature [42, 50, 52–54]. The bandgaps obtained in DFT calculations are well known to underestimate the

bandgap of a material [51]. This underestimation is also seen in DFT calculations for various poly-types of SiC where, for instance, 4H-SiC is shown to have a bandgap of 2.224 eV [146], while experimentally this has been shown to be 3.23 eV [147]. We report here the first experimental measurements on the bandgap of Al_4SiC_4 as all other reported bandgaps were obtained in computational works.

6.3 XPS

The first measurement performed on each sample as part of the XPS analysis was a survey spectrum. This is a sensitive (high pass energy), low-resolution scan over a large binding energy range (0 to 1200 eV). Although this is a low-resolution scan and so precise analysis is impossible, it does give a good overview of the elements in the sample composition leading way to identification of interesting energy ranges to be examined in further details. Figure 6.3 shows a survey spectrum of sublimation grown samples [141] of Al_4SiC_4 with the main peaks labelled as to what their chemical element is. Note that the small peaks within the spectrum are not taken into consideration as of yet, as we are only looking at the main peaks that make up the majority of the sample.

The following chemical elements collected in Table 6.1 can be identified from the XPS survey spectrum in Figure 6.3.

Chemical Element	Binding Energy (eV)
Na 1s	1073
O KLL	979
O 1s	534
C 1s	287
Si 2s	153
Al 2s	121
Si 2p	101.5
Al 2p	75.5
O 2s or Na 2p	27

Table 6.1: Table of the chemical elements picked up in the XPS survey spectrum of Al_4SiC_4 in Figure 6.3 with their corresponding binding energy.

6.3.1 Composition

A low-resolution scan is performed over the sample before and after various types of surface treatments such as etching and sputtering. These surface treatments were

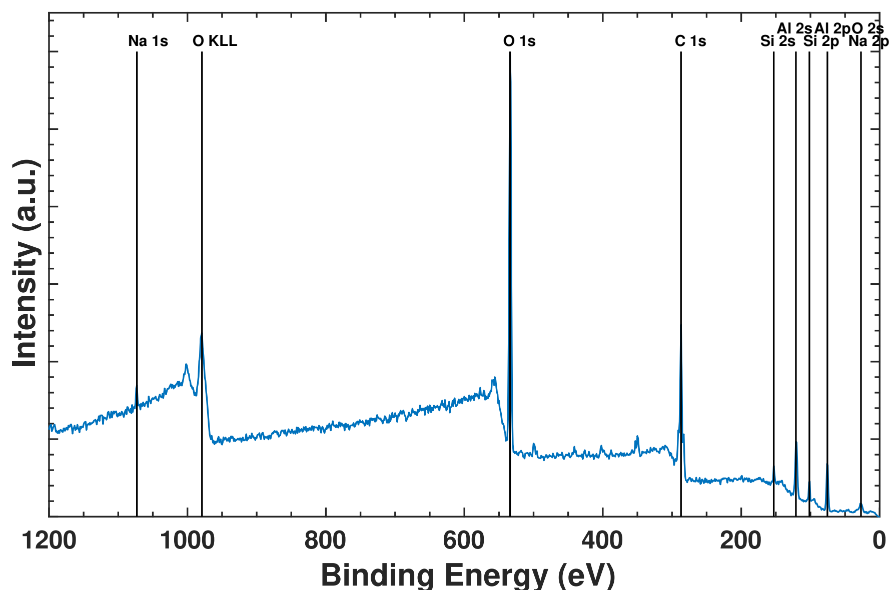

Figure 6.3: XPS survey spectra for a sublimation grown sample of Al_4SiC_4 over the range of 0 – 1200 eV measured on the DAISY FUN system at Darmstadt University. Here the peaks detail where certain elements have been found. We have added lines to these peaks to show what the elements are.

undertaken in order to remove any contamination that is on the surface of the sample to reveal the underlying chemical make up of the ternary carbide. In order to be able to perform all of the surface treatments, the sample has to be split into two pieces (A and B). We can then compare the chemical elements make up of each treatment to see what affect it has on the sample. The treatments that were performed as listed below:

- Angle Resolved XPS (ARXPS) on sample A
- Annealed at 600°C for 20 minutes on sample A;
- $Argon^+$ sputter at 250V, 10mA for 3 minutes on sample A;
- $Argon^+$ sputter at 500V, 10mA for 5 minutes on sample A;
- Wet etched - Sample B was put into a solution of H_2SO_4 to 2 parts H_2O_2 for 9 minutes followed by NH_4F for 4 minutes.

The results of the survey spectra are detailed in the pie charts in Figures 6.4a - 6.4f and reveals the chemical elements that have been picked up.

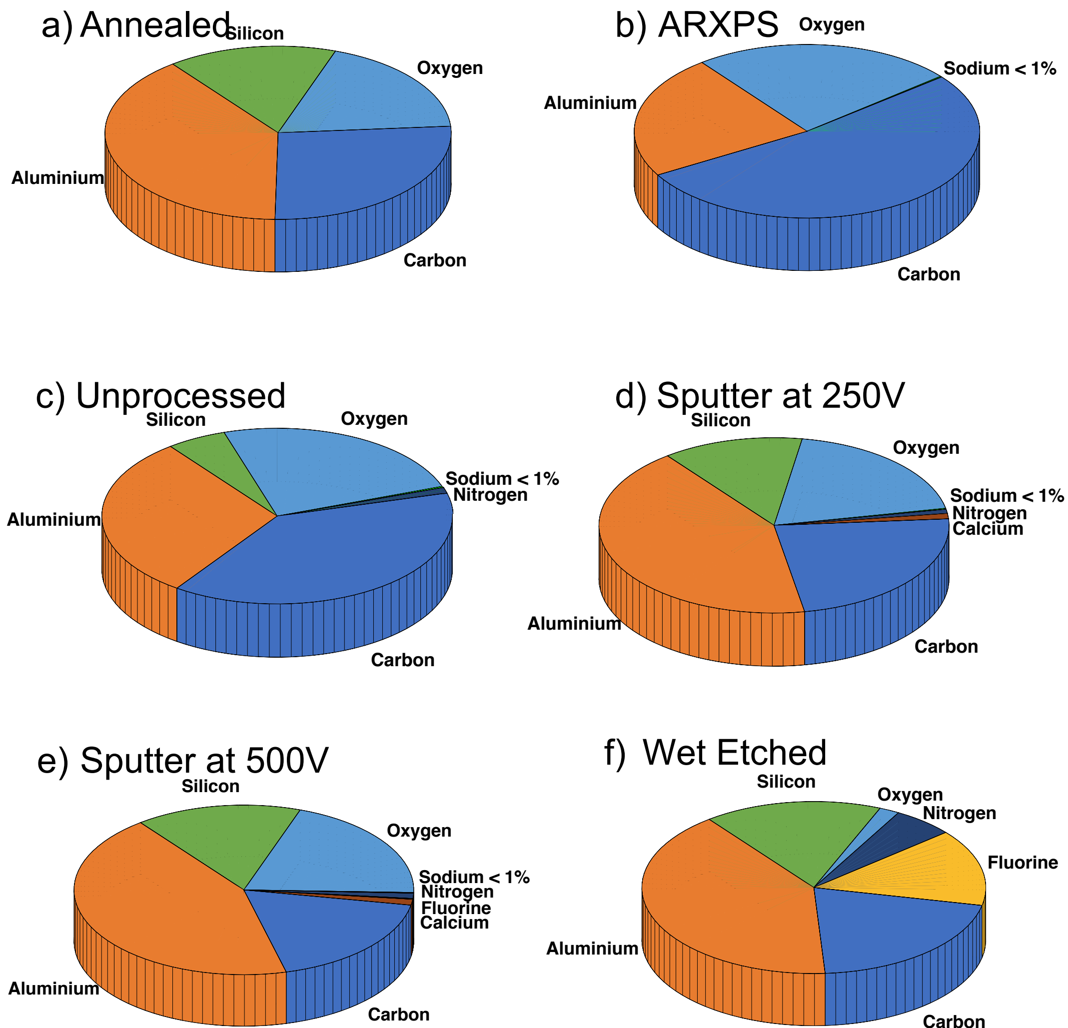

Figure 6.4: Compositions of surface treated or angled samples taken from XPS survey spectra that were recorded on the DAISY FUN system at Darmstadt University: annealed sample (a), ARXPS sample (b), unprocessed sample (c), sputtered at 250 V sample (d), sputtered at 500 V sample (e), wet etched sample (f).

Figures 6.4(a) - 6.4(f) shows the chemical make up of the sublimation grown Al_4SiC_4 samples before and after each of the surface treatments have been performed, with the exception of Figure 6.4(b) which is the unprocessed sublimation grown Al_4SiC_4 sample examined at an angel of 70° to the norm. The ternary carbide sample is primarily made up of aluminium, silicon and carbon as we would expect the compound to have. However, there is also a lot of oxygen present in the most of samples.

Table 6.2 details the pie charts in Figures 6.4(a) - 6.4(f). The chemical make up of the unprocessed sample allows to gain its relative chemical formula. Quantification

Chemical Element	Percentage found (%)					
	Unprocessed	Annealed	ARXPS	Sputtered 250V	Sputtered 500V	Wet Etched
Aluminium	29.9	39.3	23	42.4	43.6	40.6
Carbon	38.9	26.5	52.4	23.4	18.1	20.6
Calcium	0	0	0	0.992	1.1	0
Fluorine	0	0	0	0	0.153	14.4
Nitrogen	1.07	0	0	0.772	1	5.73
Sodium	0.217	0	0.159	0.173	0.136	0
Oxygen	24.4	18.4	24.5	19.3	20.1	1.89
Silicon	5.52	15.8	0	13	15.8	16.7

Table 6.2: Percentage of chemical elements found in each of the XPS survey spectra as shown in the pie charts of Figures 6.4(a) - 6.4(f).

reveals the following chemical formula when comparing to one Silicon as we have one Silicon in the formula for Al_4SiC_4: $Al_{5.45}Si_1C_{12.1}O_{7.58}Na_{0.0676}N_{0.331}$. The quantification shows 3 times as much carbon as expected. This carbon is a residue left over from the sublimation process, slightly more aluminium that expected, again a residue left over from the sublimation process, high amounts of oxygen, most likely from an oxide layer on top of the sample and, finally, small amounts of nitrogen and sodium which are contamination from handing the sample.

The unprocessed sample (Figure 6.4(c)) is primarily made up of aluminium (29.9%), carbon (38.9%), oxygen (24.4%) and silicon (5.52%) with small amounts of nitrogen (1.07%) and sodium (0.217%).

Figure 6.4(b) shows the ARXPS, which was performed on the sample at 70°, with the following primary elements: aluminium (23.0%), carbon (52.4%), and oxygen 24.5%) with a small amount of sodium (0.159%). The ARXPS allows one to vary the emission angle at which the electrons are collected, thereby enabling electron detection at different depths including a 'bulk angle', 0°, and 'surface angels', > 0°. We have performed the ARXPS at 70° in order to ascertain surface details. The ARXPS analysis indicates an absence of silicon and only aluminium, carbon and oxygen are present. This is due to detecting the surface layers of the material rather than the bulk material. Figure 2.2 shows a molecular model of the material with its layers

, and the ARXPS reveals that the surface is on a carbon layer with linking aluminium atoms. The ARXPS has also detected the sodium contamination but not the nitrogen contamination that was seen on the unprocessed sample in Figure 6.4(c).

Figure 6.4(a) shows the sample after annealing. Here four elements make up the

sample, that being; aluminium (39.3%), carbon (52.4%), oxygen (18.4%) and silicon (15.8%). When comparing this sample to the unprocessed sample, Figure 6.4c, we can see that the nitrogen and sodium contaminates have been removed. Also removed have been 6% of oxygen and 12.4% carbon leading way to higher amounts of silicon, 10.28% increase, and aluminium, 9.4% increase.

Figures 6.4(d) and 6.4(e) shows the samples after sputtering at 250V and 500V respectively. Here four main elements are seen, that being; aluminium (42.4%, 43.6%), carbon (23.4%, 18.1%), oxygen (19.3%, 20.1%) and silicon (13.0%, 15.8%). Also see is that of nitrogen (0.772%, 1.0%) and fluorine (0%, 0.153%) which are contaminates that have been introduced during this surface, treatment these are most like to be contaminates that are already in the apparatus interacting with the sample. Comparing this surface treatment to the unprocessed sample, Figure 6.4c, we see an increase in aluminium (12.5%, 13.7%), and silicon (7.48%, 10.28%). Also see is a decrease in carbon (15.5%, 20.8%) and oxygen (5.1%, 4.3%).

Figure 6.4(f) shows the sample after wet etching. Here we can still see the four main elements, aluminium (40.6%), carbon (20.6%), oxygen (1.89%) and silicon (16.7%). In addition to the main elements we see that of fluorine (14.4%) and nitrogen (5.73%) that have introduced during the etching process. Comparing the etched sample to the unprocessed sample, we can see that there has been an increase of aluminium (10.7%) and silicon (11.18%) and a decease in carbon (18.36%) and oxygen (22.51%).

From the XPS spectra the elements that could be used for doping Al_4SiC_4 could be similar to SiC as we require the same amount of outer electrons for doping, 5 for n-type and 3 for p-type. For p-type doping, Sodium as it can already be seen on the survey spectrum and has 3 outer electrons. For n-type doping there is no evidence in the spectrum for what elements could be used for this. However, n-type doping would most likely be brought on by defects in the material.

6.3.2 Valence Band

A detailed scan was undertaken at the lowest binding energy from 0 eV to 10 eV in order to get a valence band spectrum for the samples as presented in Figures 6.5 to 6.10. Each spectrum is fitted with a step-down function via the software package CasaXPS and a tangent to this function which is done by visual inspection. The point at with this tangent crosses the x-axis is the point where the Fermi level, E_F, lies above the valence band.

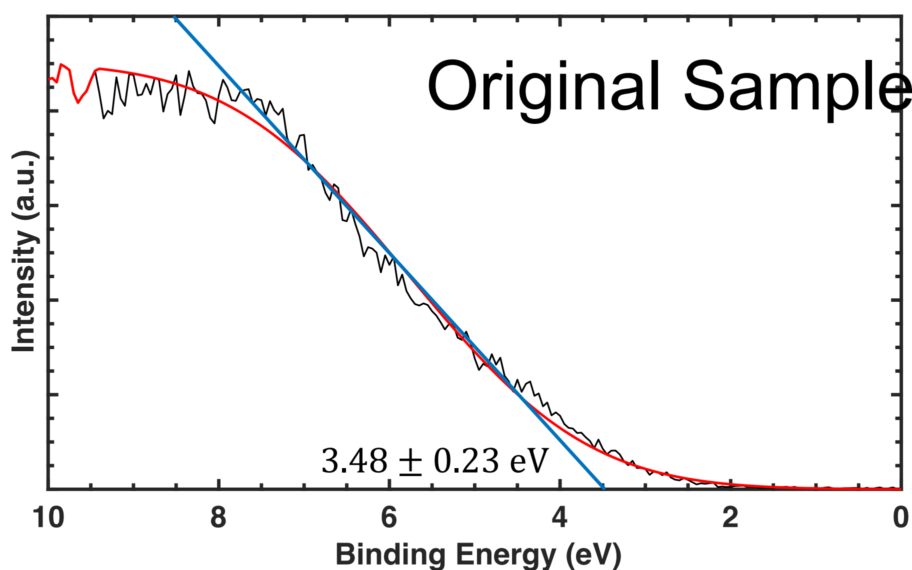

Figure 6.5: XPS valence band profiles obtained on the DAISY FUN system at Darmstadt University for the unprocessed sample. A fitted step down function (blue line) and a tangent to this (red line) are also shown. The point at which the tangent crossed the axis is noted on each of the figures, this is the amount the Fermi level lies above the valence band.

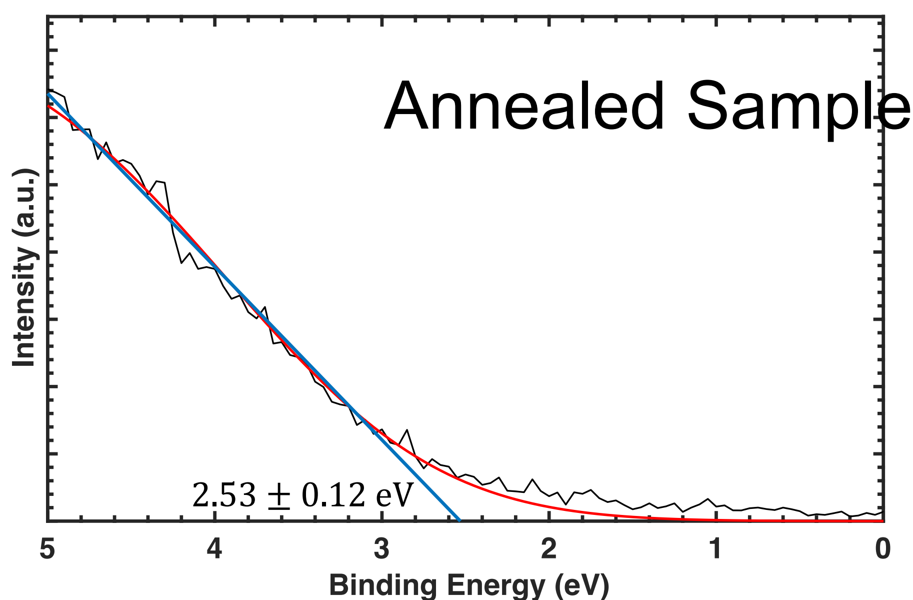

Figure 6.6: XPS valence band profiles obtained on the DAISY FUN system at Darmstadt University for the unprocessed sample. A fitted step down function (blue line) and a tangent to this (red line) are also shown. The point at which the tangent crossed the axis is noted on each of the figures, this is the amount the Fermi level lies above the valence band.

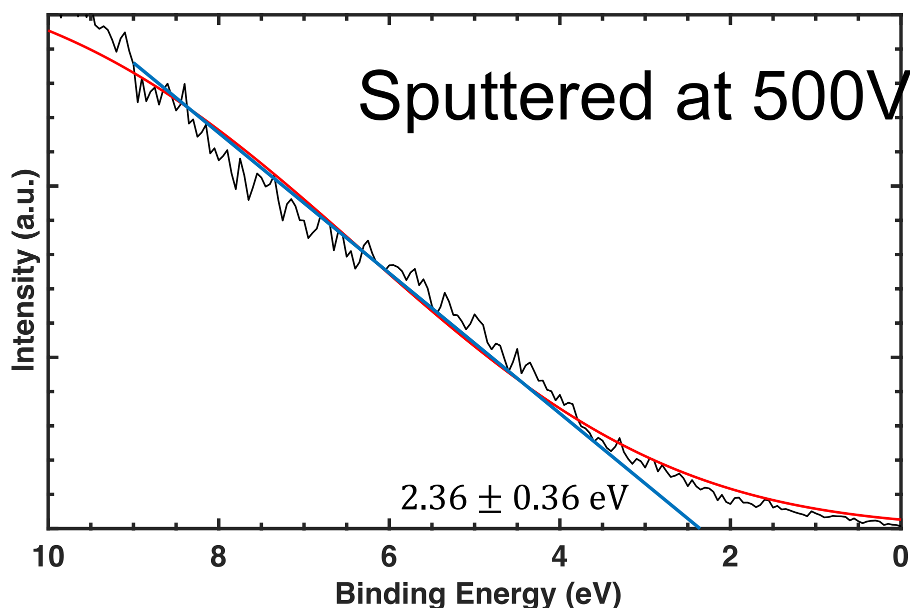

Figure 6.7: XPS valence band profiles obtained on the DAISY FUN system at Darmstadt University for the sputtered sample at 500 V. A fitted step down function (blue line) and a tangent to this (red line) are also shown. The point at which the tangent crossed the axis is noted on each of the figures, this is the amount the Fermi level lies above the valence band.

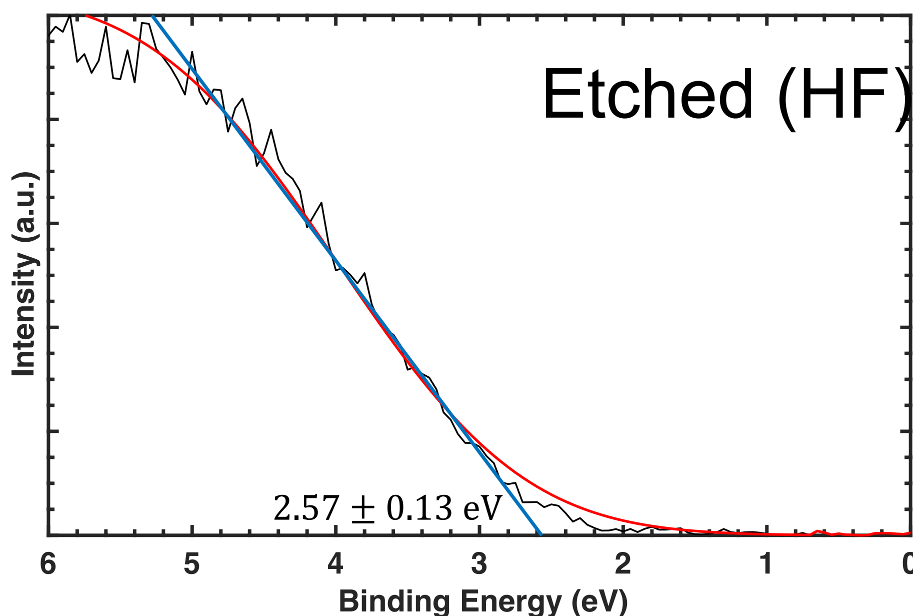

Figure 6.8: XPS valence band profiles obtained on the DAISY FUN system at Darmstadt University for the wet etched sample with HF. A fitted step down function (blue line) and a tangent to this (red line) are also shown. The point at which the tangent crossed the axis is noted on each of the figures, this is the amount the Fermi level lies above the valence band.

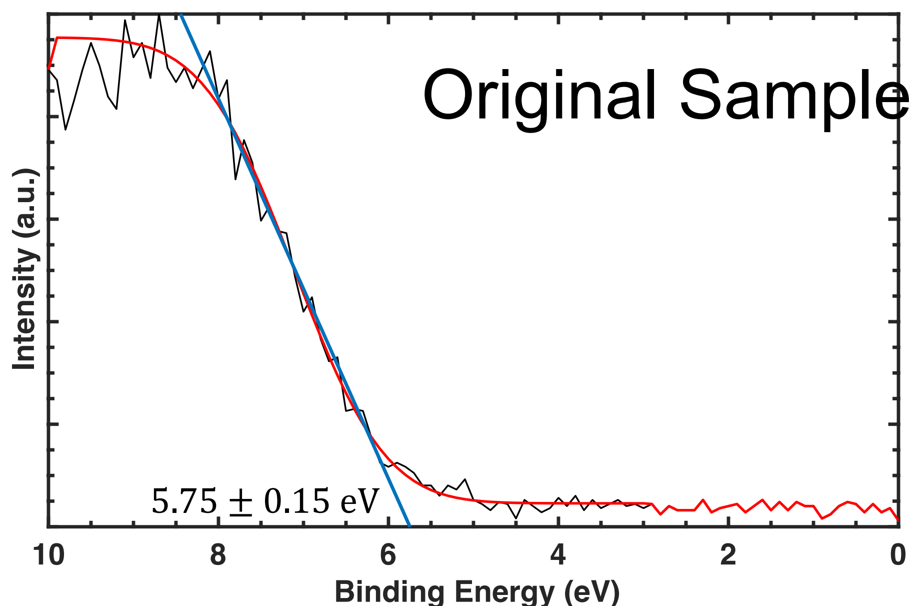

Figure 6.9: XPS valence band profiles obtained on the Kratos Supra XPS spectrometer at Swansea University for the unprocessed sample. A fitted step down function (blue line) and a tangent to this (red line) are also shown. The point at which the tangent crossed the axis is noted on each of the figures, this is the amount the Fermi level lies above the valence band.

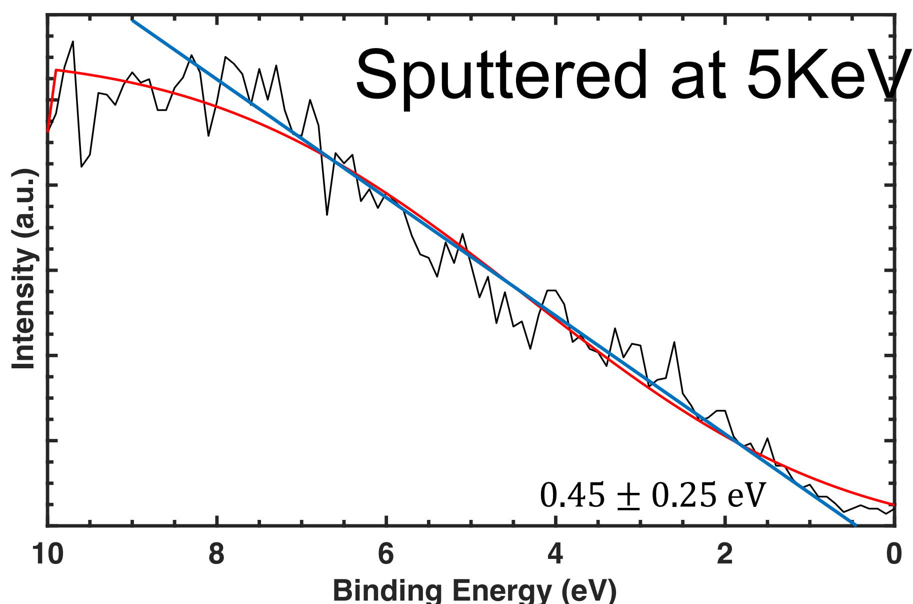

Figure 6.10: XPS valence band profiles obtained on the Kratos Supra XPS spectrometer at Swansea University for the sputter sample at 5 keV . A fitted step down function (blue line) and a tangent to this (red line) are also shown. The point at which the tangent crossed the axis is noted on each of the figures, this is the amount the Fermi level lies above the valence band.

Figures 6.5 to 6.10 show that the point at which the Fermi level lies shifts lower when the sample are cleaned by various methods. The higher the value for the Fermi level indicates a thicker oxidation layer on top of the Al_4SiC_4 sample which is clear to see when we look at depth profile in Section 6.3.4. The oxidation layer has most likely formed during the growth of the Al_4SiC_4 sample as aluminum oxy carbides where present during the fabrication process [148]. This oxidation layer is marking the material n-type as the Fermi level is sitting above the midpoint between the valence band and the conduction band. As the sample is cleaned and the oxidation layer gets removed, the sample goes from being n-type to p-type as the Fermi level sit below the midpoint between the valence band and the conduction band.

6.3.3 Workfunction

By performing ultraviolet photoelectron spectroscopy (UPS) we can determine the workfunction of the sample by determining the low kinetic energy cut-off point of the material. This was performed on sample after some of the surface treatments was and was done on both the DAISY FUN system at Darmstadt University and on the Kratos Supra XPS spectrometer at Swansea University. The main difference between the two set ups was, the Kratos Supra XPS spectrometer uses a helium 1α gas as a discharge in the determination of the workfunction and the DAISY FUN system did not. This means that calculating the workfunction is slightly different. Equation (6.1) is used when using helium, He1 = 21.21 eV, and Equation (6.2) is used when helium is not used.

$$\Phi = \mathrm{He1} - 2^{\mathrm{nd}}_{\mathrm{cutoff}} \tag{6.1}$$

$$\Phi = 2^{\mathrm{nd}}_{\mathrm{cutoff}} - E_F \tag{6.2}$$

When helium gas discharge is used, the calculation is straightforward as the helium is used as a reference energy and them combined with the secondary cut off point, see Equation 6.1. When the helium is not used we need to know the position of the Fermi level which comes from the XPS valence band data that was measured in Figures 6.5-6.10 and is combined with the secondary cut off point, see Equation 6.2.

Figures 6.11 to 6.13 present a UPS spectra detailing the workfunction for 2 samples which have undergone different surface treatments. A variation in the workfunction can be seen. It can be seen that the workfunction of the Al_4SiC_4 sample increases from 3.6 eV to 5 eV as the cleaning is performed on the sample on the DAISY FUN system at

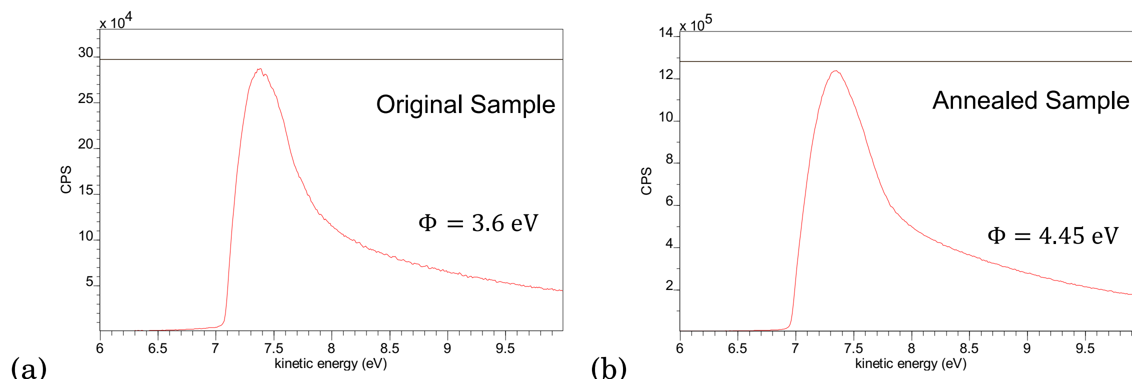

Figure 6.11: UPS spectrum obtained on the DAISY FUN system at Darmstadt University showing the secondary cut-off point and the calculated workfunction for: unprocessed sample (a), and annealed sample (b).

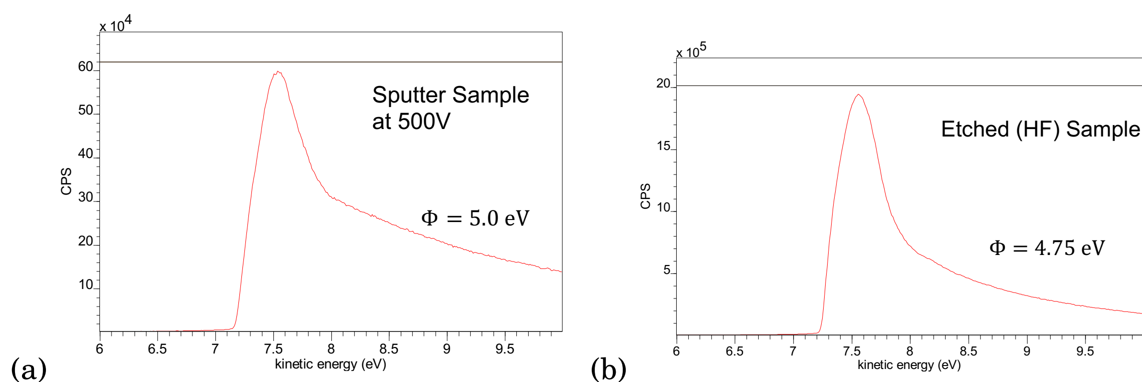

Figure 6.12: UPS spectrum obtained on the DAISY FUN system at Darmstadt University showing the secondary cut-off point and the calculated workfunction for: sputter sample at 500V (a), and wet etched sample with HF (b).

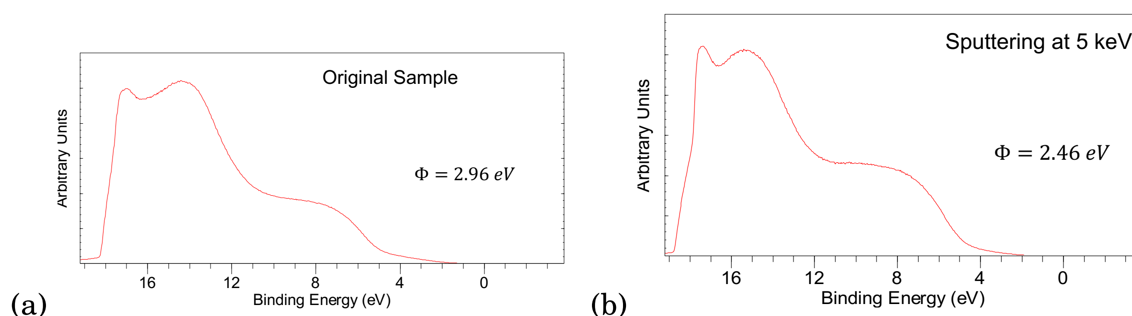

Figure 6.13: UPS spectrum obtained on the Kratos Supra XPS spectrometer at Swansea University showing the secondary cut-off point and the calculated workfunction for: unprocessed sample (a), and sputter sample at 5 keV (b).

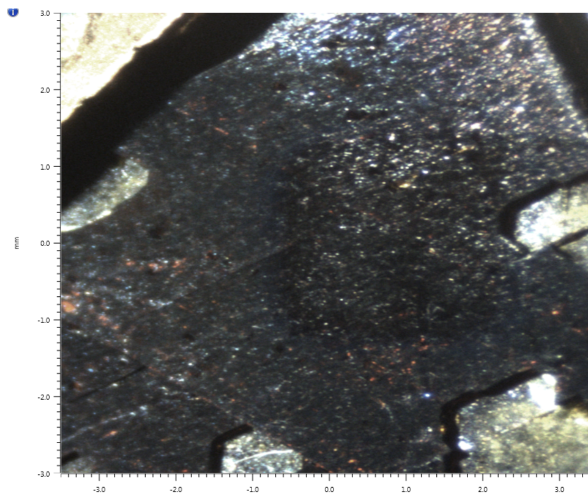

Figure 6.14: Microscope image of the Al_4SiC_4 sample under the Kratos Supra XPS spectrometer showing the area that has been sputtered, by the slightly darker square area.

Darmstadt University. However, this workfunction increase is not seen with the sample done on the Kratos Supra XPS spectrometer at Swansea University as the workfunction is reduced from 2.96 eV to 2.46 eV after sputtering at 5 keV. This change in workfunction during a surface treatment is most likely linked to the oxidation layer that occurs on the sample and/or relates to any other contamination that has been seen on the surface of our samples. It stands to reason that the work we did on DAISY FUN system at Darmstadt University is correct as it matched other XPS experiments, where it is seen that the more aluminum oxide removed the higher the workfunction [149, 150].

6.3.4 Depth Profiling

Depth profiling is a very useful way to examine a sample. A high resolution scan of selected areas of interest around the carbon, oxygen and aluminum positions is performed after sputtering a sample at 5 keV for 1 minute. Then, another sputtering is performed at the same energy and time length. We repeated this process 35 times cutting into the Al_4SiC_4 sample as seen by the dark square patch in Figure 6.14. With depth profiling we look at the oxygen (O1s), carbon (C1s) and aluminum (Al2p) peaks, Figures 6.15, 6.16 and 6.19 respectively. We decided not to look at the silicon peak here as we were more interested in the three other peaks

Figure 6.15 shows multiple detailed spectra in the range of 525-543 eV where is the location of the oxygen 1s peak. The spectrum is made up of 35 individual spectra take

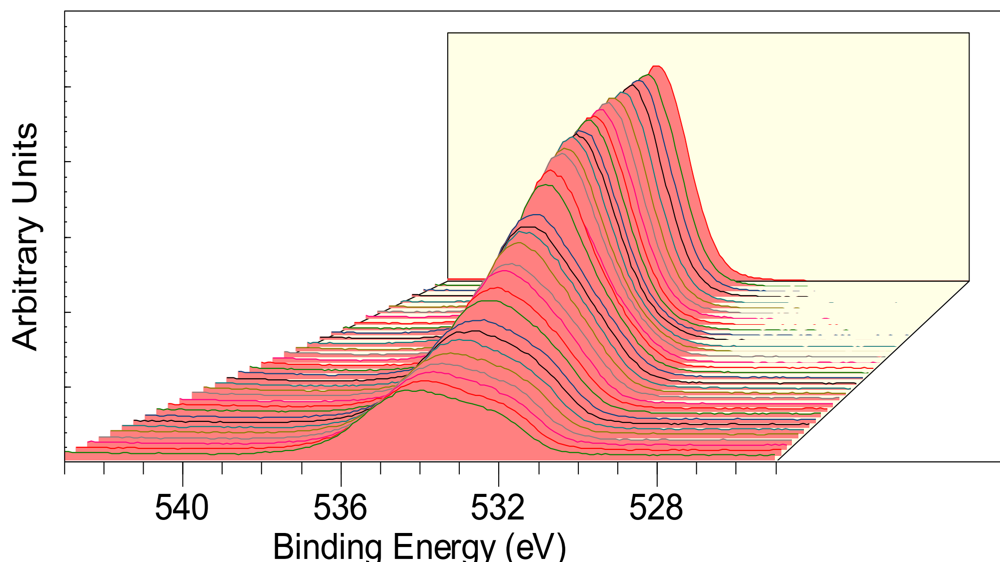

Figure 6.15: Depth profile made up of XPS spectra in the O1s region during the 35 sputterings. The first spectra is at the further point along the z-axis and the last spectra is at the front of the z-axis in order to show the reduction of the O1s peak as the sputters take place.

before each of the 5 eV sputterings. Figure 6.15 therefore details the oxygen 1s peak over the course of the sputterings. The sputtering removes the oxygen from the sample which is evident from the decreasing oxygen 1s peak, but does not vanish all together and, therefore, does not completely remove all of the oxygen from the sample. Note; the first recorded spectra in the 3D plot, Figure 6.15 is at the back of the 3D plot and the last recorded spectra after all 35 sputterings have taken place, is at the front of the 3D plot.

Figure 6.16 shows multiple detailed spectra in the range of 275-295 eV, this is the location of the carbon 1s peak. The spectrum is made up of 35 individual spectra take before each of the 5 eV sputterings. Figure 6.16 therefore details the carbon 1s peak over the course of the sputterings showing that as sputtering is taking place, there is a rise in the amount of carbon detected. This carbon increase can be detected by a rise in the peak at low binding energy, 282 eV. There is also a peak at high binding energy, 289 eV, which reduces as the sputtering continues. We can analyse these peaks further by taking a cross-section through Figure 6.16, see Figures 6.17 and 6.18. Note; the first recorded spectra is at the front of the 3D plot and the last recorded spectra is at the back of the 3D plot.

Figure 6.17 is taken half way through Figure 6.16 in order to details the diminishing peaks and the rising peaks. The cross-section details four main bonds: C-C, C-O-AL, C-Si

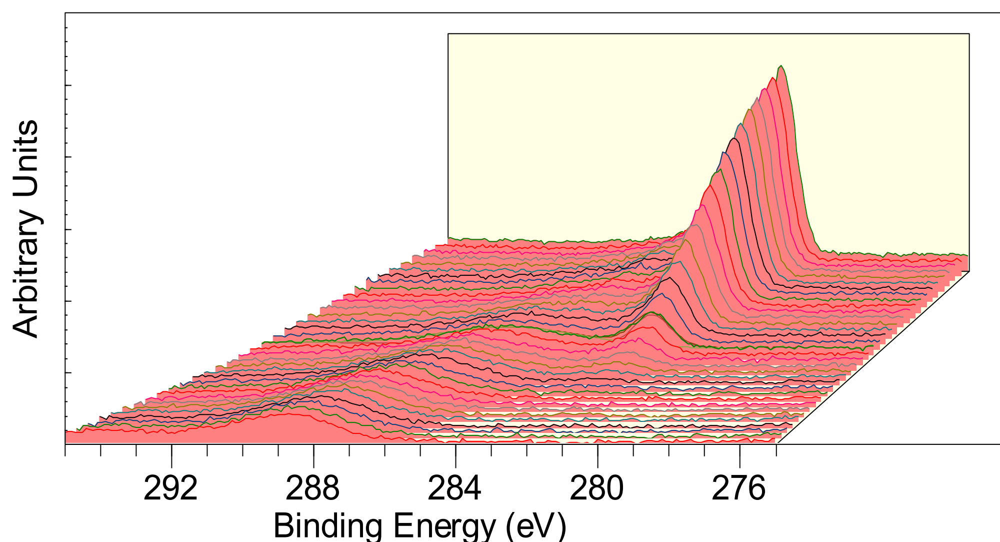

Figure 6.16: Depth profile made up of XPS spectra in the C1s region during the 35 sputterings. The first spectra is at the front of the z-axis and the last spectra is at the further point along the z-axis.

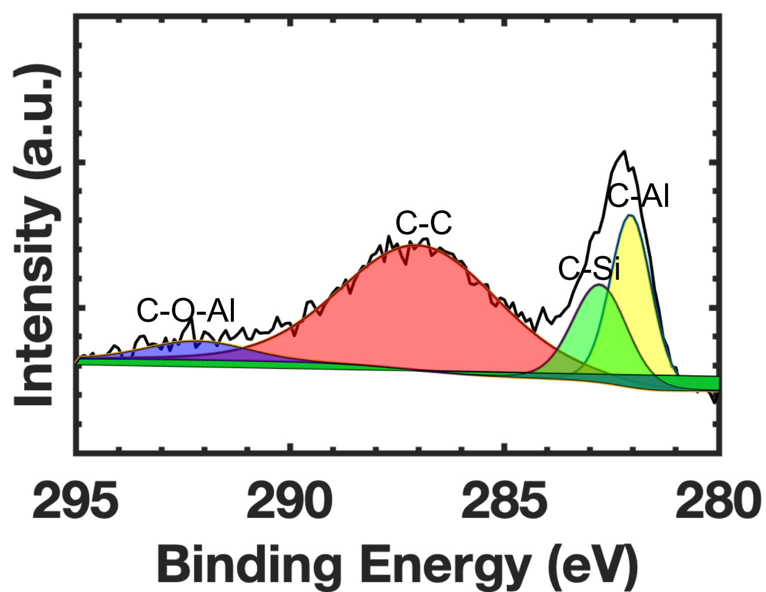

Figure 6.17: XPS spectra taken from the middle of the C1s depth profile, see Figure 6.16, showing the chemical bonds that are present.

and C-Al. During the sputtering, the C-C bond is decreasing along with the Al-O-C bond and the primary bond, C-Al, is most dominate. This is due to the molecular make-up of Al_4SiC_4, as shown in Figure 2.2, where the top layer of our sample is showing C-Al, and the carbon contamination on the surface of the sample is removed as shown with the reduction in the peak for the C-C bond.

Multiple detailed spectra in the range of 66-86 eV, which is the location of the aluminium 2p peak is shown in Figure 6.19. Figure 6.19 is made up of 35 individual spectra taken before each of the 5 eV sputterings and so details the aluminium 2p over the course of the sputtering. Here it can be seen that there is a change in the aluminium bond by a rise in the peak at the lowest energy level and a decrease in the peak at highest energy level. The peaks can be analysed further but taking two cross-section through Figure 6.19, see Figures 6.20 and 6.21.

The first cross-section Figure 6.20 details four main bonds: Al-C, Al-O, Al-O-C and Al-Al. During the 35 sputterings, the Al-O-C and the Al-O bonds are decreasing and the primary bond, Al-C, come through as most dominant. This is most likely due to the molecular make up of of Al_4SiC_4 as illustrated in Figure 2.2 where the top layer of the molecule is made up of Al-C bonds.

6.4 I-V Measurements

Solution grown samples [42] are probed with two separate methods, one a standard two-probe method and a four-probe Van der Pauw method, as explained in Section 3.9. These samples are prepared by washing them in isopropanol and acetone for 5 minutes each in a sonic bath. The samples are then attached to a sapphire crystal as illustrated in Figure 6.22. The sapphire substrates are used in order to electrically isolate samples from the bottom plate of the apparatus. Note also that the sublimation grown samples could not be used as they were attached to a conducting substrate during the growth period and which is not possible to remove without a damage to the samples.

Each sample was then probed by moving two sharp titanium probes (which had been calibrated beforehand, by touching the two probes together) onto the surface of the sample in order to make an electrical contact. Once electrical contact was made, current was applied and measurements taken. The results of these measurements are presented in Figures 6.23, 6.24 and 6.25.

An I-V linear region is identified by a straight line (red line on the figure) on Figures 6.23 and 6.24.

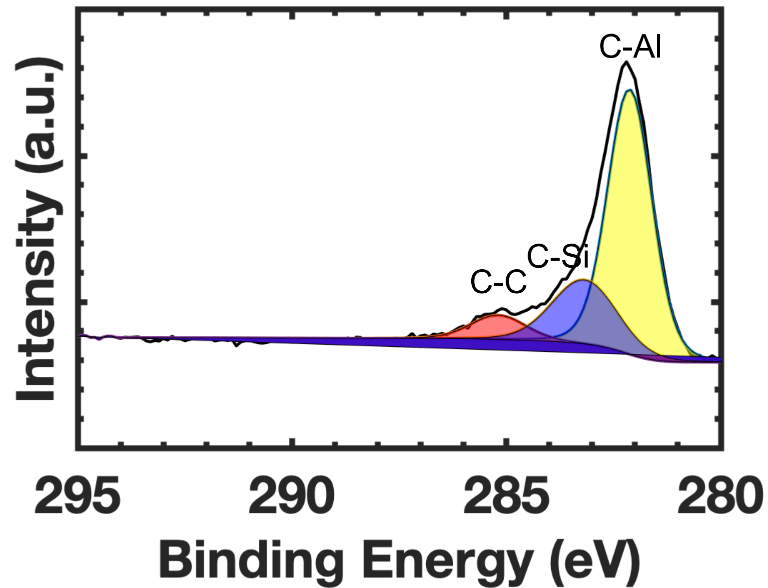

Figure 6.18: Final XPS spectrum of the C1s region after all the 35 sputterings have taken place and showing the chemical bonds that are present.

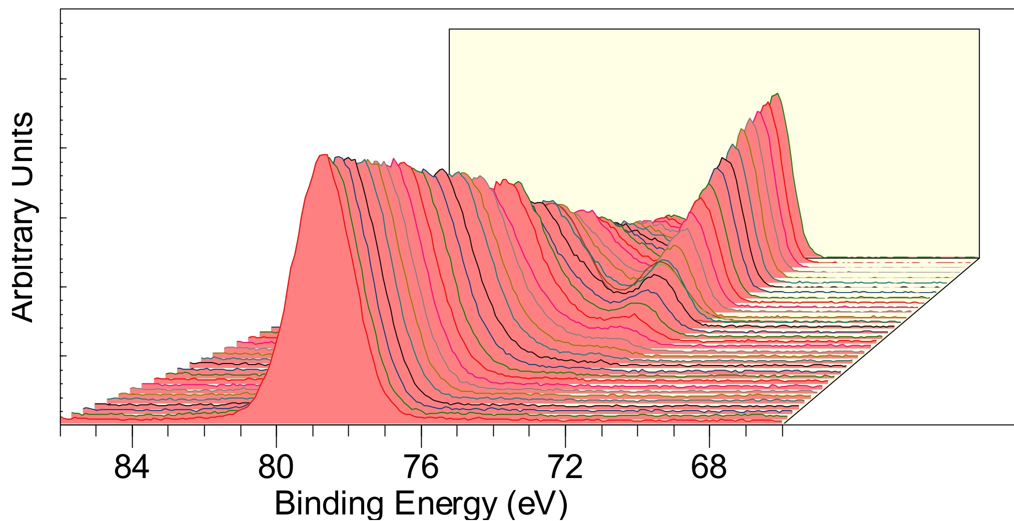

Figure 6.19: Depth profile made up of XPS spectra in the Al 2p region during 35 sputterings. First sputter is at the front of the z-axis and the last sputter is at the back of the z-axis

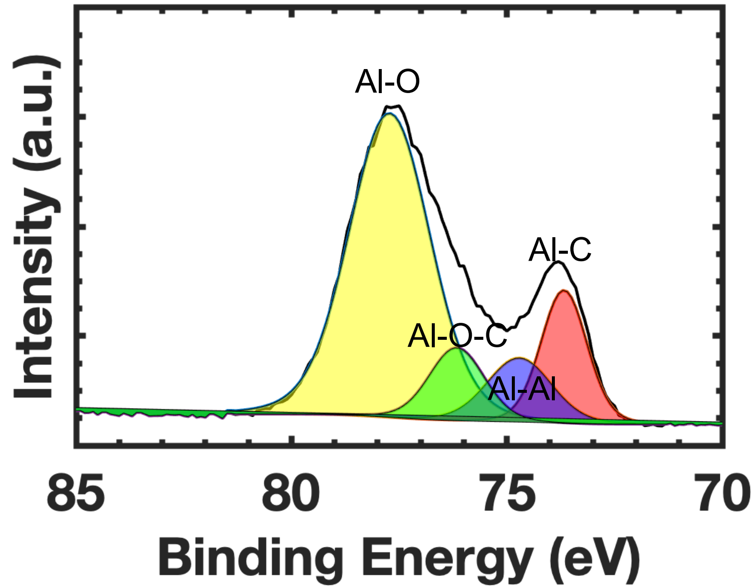

Figure 6.20: XPS spectra taken from the middle of the Al 2p depth profile, see Figure 6.19, showing the chemical bonds that are present.

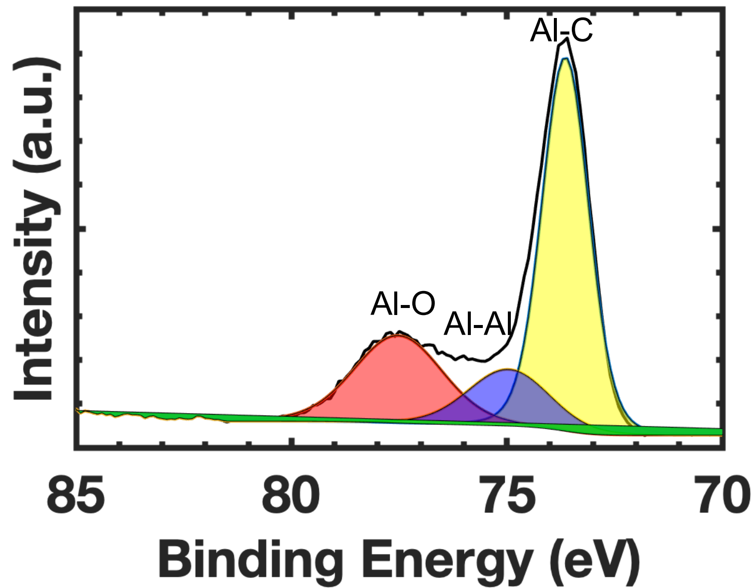

Figure 6.21: Final XPS spectra of the Al 2p region after all the 35 sputterings have taken place and showing the chemical bonds that are present.

FIGURE 6.22. Photographic image of four samples prepared and attached to a sapphire crystal.

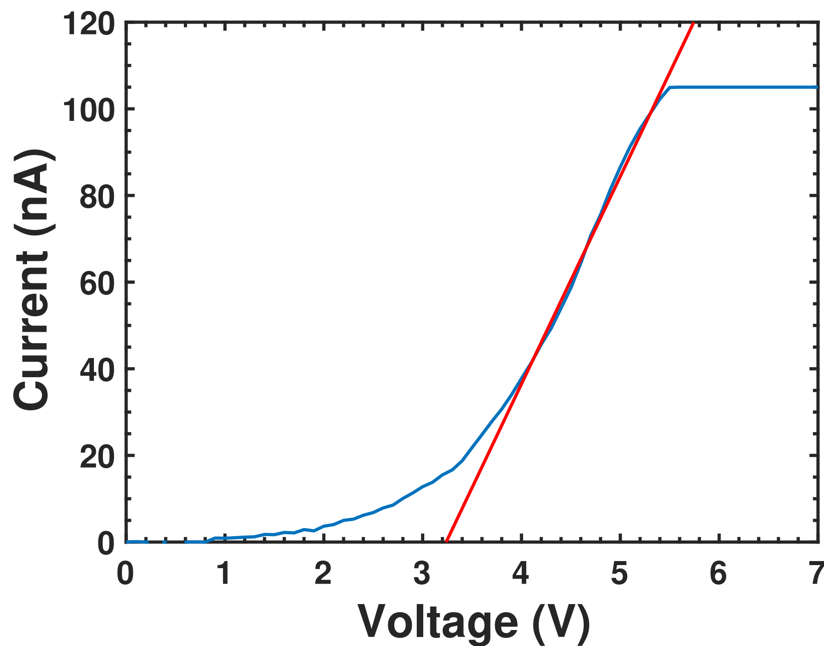

FIGURE 6.23. I-V characteristics obtained from two probe measurements Ossila four-probe system at Swansea University. Blue line shows the data collect and the red line is a linear fit against the slope.

A first order polynomial fit is used to fit the data in the linear region in Matlab. The regression coefficient R^2 was given as $R^2 = 0.9892$ for Figure 6.23 and $R^2 = 0.9151$ for Figure 6.24. The polynomial fit was taken in order to calculate the resistivity, resistance, and conductivity of the Al_4SiC_4 sample. The sample was probed on two different system,

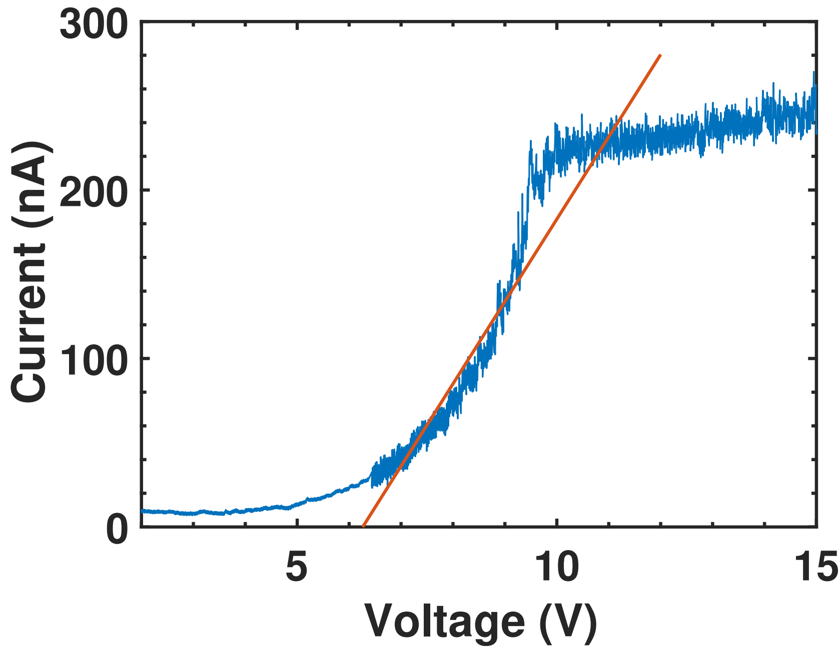

FIGURE 6.24. I-V characteristics obtained from two probe measurements on the Ametek ModuLab XM Material Test System at Neel Institute. Blue line shows the data collect and the red line is a linear fit against the slope.

the Ametek ModuLab XM Material Test System in Grenoble (Neel Institute) and the Ossila four-probe system in Swansea (Swansea University). There are more data points in the results obtained from on the Ametek ModuLab XM Material Test System compared to the Ossila four-probe system. We also see that the Al_4SiC_4 sample is saturating at around 5.3 V on the Ossila four-probe system, at a lower voltage when compared to 9.8 V on the Ametek ModuLab XM Material Test System.

From the I-V characteristic measurements done in Swansea we can calculate the resistivity (R) and conductivity (σ) of the sample in the following way:

$$\rho = \frac{V}{I} = 2.088 \times 10^{6} \Omega m \tag{6.3}$$

$$R = \rho \frac{L}{A} = 2.88 \times 10^{6} \Omega m \frac{338.71 \times 10^{-6} m}{3.19 \times 10^{-8} m^{2}} = 2.217 \times 10^{10} \Omega \tag{6.4}$$

$$\sigma = \frac{1}{R} = \frac{1}{2.217 \times 10^{10} \Omega} = 4.512 \times 10^{-11} S m^{-1} \tag{6.5}$$

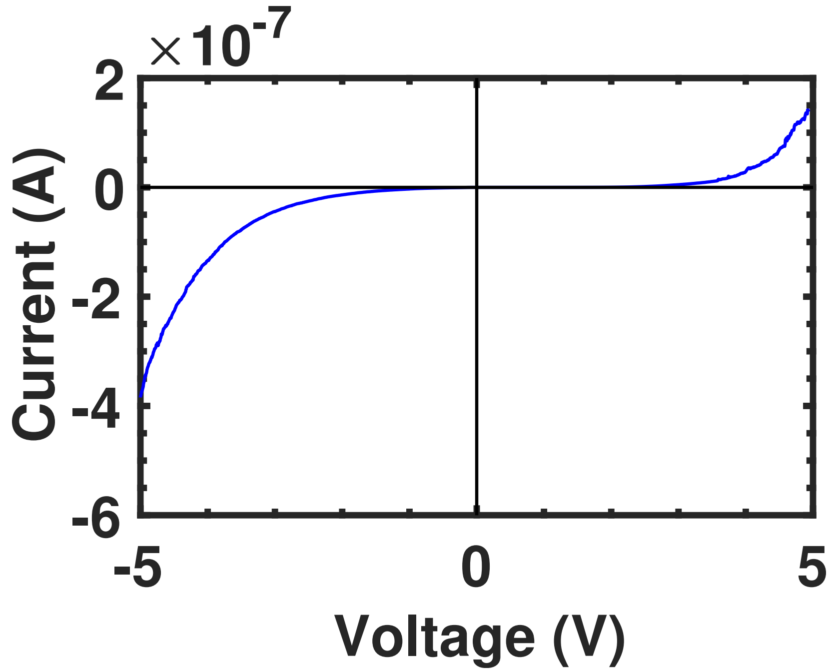

FIGURE 6.25. I-V characteristics obtained from two probe measurements for a sample with silver epoxy contacts showing the type of contact that is being made with the probes and the sample.

Parameters:
L (Distance between probes) = $338.71 \times 10^{-6} m$
W (Width of the sample) = $1276.1 \times 10^{-6} m$
T (Thickness of the sample) = $25 \times 10^{-6} m$
A (Cross-section area) = W x T = $3.19 \times 10^{-8} m^3$

Compound	Resistivity (Ωm)	Conductivity (Sm^{-1})
Al_4SiC_4 (Swansea)	2.2165×10^{10}	4.5117×10^{-11}
Al_4SiC_4 (Grenoble)	2.1725×10^{10}	4.6030×10^{-11}
GaN	1×10^{5}[151]	1×10^{-5}
4H-SiC	1.99×10^{11} [152]	5.025×10^{-12}

TABLE 6.3. Comparison of resistivity, conductivity for Al_4SiC_4, un-doped GaN and un-doped 4H-SiC. Note: The doping has a large impact on the resistivity and conductivity and so these values might vary considerably.

Figure 6.25 shows the type of contact that has been made with the probe and the sample which has been identified as a Schottky contact due to the rectifying properties.

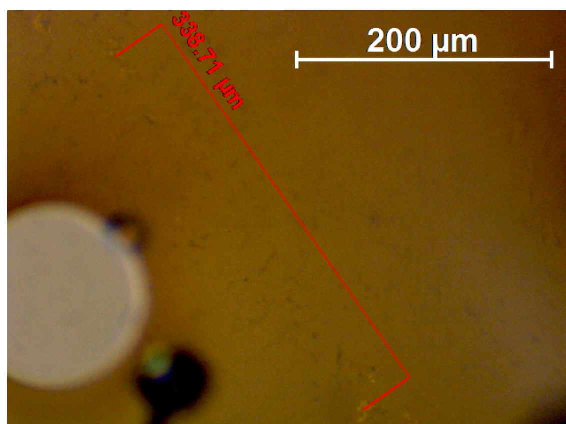

FIGURE 6.26. Microscope image of the Al_4SiC_4 sample showing the measured distance between the two probes.

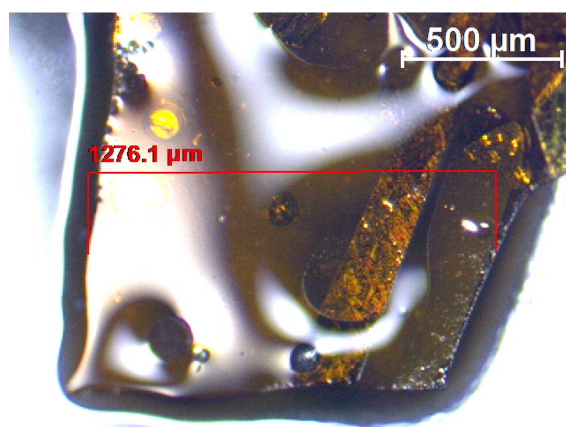

FIGURE 6.27. Microscope image of the Al_4SiC_4 sample showing the measured width of the sample.

The resistivity and conductivity of the two samples of Al_4SiC_4 were measured to be almost the same on the two different probing systems, see Table 6.3. Comparing the results of the two-probe measurements with other well known WBG semiconductors we can see that the measured resistivity and conductivity of the Al_4SiC_4 samples are similar to that of 4H-SiC, within one order of magnitude.

These results make Al_4SiC_4 a viable semiconductor for use in the electronics industry which could be used in the place of SiC or in a conjunction with SiC.

The four-probe measurements are performed in a similar way to the two-probe measurements. Four-probes measurements seen in Figure 6.28 have a voltage applied across two of the probes and a current measured across the other two.

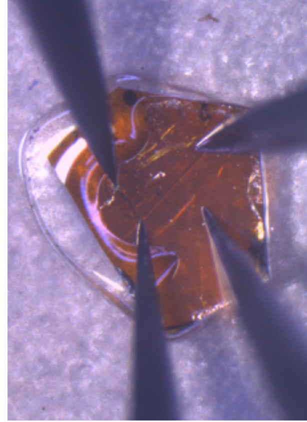

FIGURE 6.28. Microscope image on the Ametek ModuLab XM Material Test System showing the Al_4SiC_4 sample with four probes attached.

Here we could not get a good electrical contact directly with the sample and the probe. Therefore, contact were tried on the solution grown Al_4SiC_4 samples. This is done in order to reduce the contact resistance between the sample and the probes. Two different contact are used: silver epoxy and deposited titanium. The silver epoxy is a silvery/white paste that is applied to the Al_4SiC_4 in four locations using a needle in order to get four small contacts for the titanium probes to be located on. The titanium contact are deposited by using a mask and a deposition process, six titanium contact are deposited in total, where only four are used in the probing process. The titanium contacts can be seen in Figure 6.29. Here we found that the titanium contacts disintegrated during annealing leaving only small amounts of titanium which were not good enough for the probes to gain an electrical contact with the sample.

The results from the four-probe I-V characteristic measurements did not reveal any usable data as we were unable to make an electrical contact with the sample and the probes. We think think this was due to issues over a insulating layer on top of the sample, possibly from the oxide causing the apparatus no to read the current or voltage as one would expect. Due to this the data collected has been omitted from the thesis. We can use the measured conductivity and the calculated electron mobility to calculate the carrier (electron) concentration using the following equation

$$\sigma = ne\mu_e \tag{6.6}$$

where σ is the conductivity, n is the concentration of electrons, e is the elementary charge and μ_e is the mobility of the electrons at low electric field.

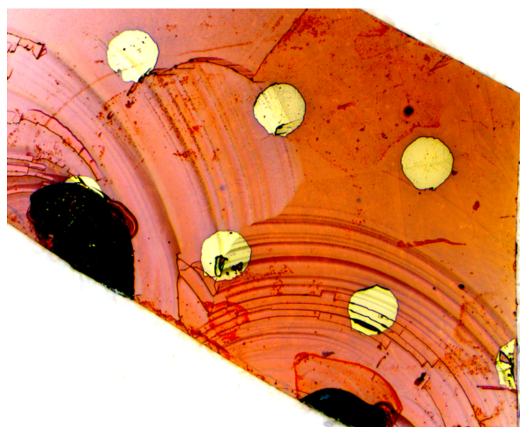

FIGURE 6.29. Microscope image of a Al_4SiC_4 sample with six titanium contacts grown on top.

Using Equation 6.6 reveals an electron concentration of $3.396 \times 10^{16} cm^{-3}$. This concentration value is similar to the ionized impurity concentration data that was calculated in the MC simulation as shown in Figure 5.11.

6.5 Discussion

Solution grown crystals [42] of Al_4SiC_4 have been examined by use of UV/Vis/NIR spectroscopy in order to ascertain their bandgap. By taking further band tailing into account, the technique has revealed a bandgap of 2.778 ± 0.02 eV which is inline with the results reported from Valence Electron Energy-Loss Spectroscopy (VEELS) experiment [126]. The VEELS experiment was carried out at the University of Cadiz in Spain using a transmission electron microscope (TEM), in particular the Field Electron and Ion Company (FEI) Titan Themis system, which revealed a bandgap of 2.8 eV ± 0.2 eV.

Sublimation grown crystals [44] of Al_4SiC_4 were examined by XPS on two different set ups, the Darmstadter Integrated System for Fundamental Research (DAISY FUN) system at Darmstadt University and on a Kratos Supra XPS spectrometer at Swansea University. The workfunction, valence band and chemical composition were all studied. The data on the workfunction varied from giving a workfunction of 5.0 eV - 2.46 eV between the two systems and varied depending on the surface treatment that was performed on the Al_4SiC_4 samples. This variability in workfunction data has made it difficult to make any correlation with the data and the samples and, therefore, further studies of the workfunction would be needed in order to ascertain any correlation.

The sample used at Swansea University seems to have bigger oxidation layer than the sample used at Darmstadt University. This oxidation layer has a direct impact on the position of the Fermi level. The thicker this oxidation layer for example, at 5.75 eV as measured on the Kratos Supra XPS spectrometer system. Therefore, a higher Fermi level is in the material thus making it an n-type material as the Fermi level sits closer to the conduction band. As this oxidation layer is removed by surface treatment, the material changes its intrinsic doping characteristic from n-type to p-type, this was seen after the harshest treatment of 5 keV where a valence band position drops from 5.75 eV to 0.45 eV and so the Fermi level is closer to the valance band.

Through the XPS, we have been able to show that contamination from the samples of Al_4SiC_4 can be removed through various surface treatments. The oxygen contamination is the hardest to remove and need a high energy treatment in order to remove it. We have also shown that as the surface treatment takes place and removes the oxide layer, the larger the workfunction of the material is changing from 3.6 eV to 5.0 eV, which is inline with current literature [149, 150].

The I-V characteristic measurements taken from electrical probing with the two probe method has revealed resistivity and conductivity of 2.2×10^{10} Ωm and 4.6×10^{-11} Sm^{-1}), respectively, which is very similar to 4H-SiC. We had been able to show that a Schottky contact is present on the sample. In order to gain more precise values for resistivity and conductivity, we have measured the I-V characteristics by four probe method and with the deposition of contacts on the sample both by silver epoxy and titanium. No usable data was collected by the four probe method due to an insulating layer on top of the Al_4SiC_4 sample preventing to measure a current across the sample. This is most likely due to the oxidation layer that has been seen on the surface of Al_4SiC_4 sample during the XPS.

The I-V characteristic measurements have allowed us to extract a conductivity which has been then used to calculate the electron concentration revealing a value of 3.396×10^{16} cm^{-3}. This concentration matches the MC simulated data for ionized impurity concentration of 10^{14} cm^{-3} to 10^{17} cm^{-3} at a mobility of approximately 96 cm^{2}V^{-1}s^{-1} (see Figure 5.11).

Chapter 7

Summary and Conclusion

This chapter will give a short summary of the obtained results from both the computation and the experimental works. It will then discuss the consequences in a broader context and, finally, it will give an outlook on possible future works.

7.1 Summary

The goal of this work was to evaluate a novel wide bandgap semiconductor material based on ternary carbides, that being Al_4SiC_4, for applications in the electronics industry, primarily power electronics. Both computational and experimental approaches were used in various applications to ascertain the opto-electronic properties of Al_4SiC_4. The computational approach looked at two different areas: (1) bulk electrical properties of Al_4SiC_4 simulated using an ensemble Monte Carlo code; and (2) device modelling of a SiC/Al_4SiC_4 heterostructure transistor by Silvaco Atlas [40]. The experimental approach saw three experiments undertaken: (1) UV/Vis/NIR Spectroscopy looked at defining the bandgap of Al_4SiC_4, (2) XPS looked at the workfunction, a position of the valence band and the overall composition of Al_4SiC_4, and (3) two- and four-probe DC current voltage characteristics obtained the resistivity of Al_4SiC_4. The experiments used samples of Al_4SiC_4 that were grown at Grenoble University [42, 141].

Experimental and computational data on material properties of Al_4SiC_4 are rare and often inaccurate, with Al_4SiC_4 being difficult to model computationally. Therefore, scattering potentials for electron-phonon interactions are unknown while the phonon

energies were taken from Raman spectroscopy. In places, we have opted for material properties for 4H-SiC as the semiconductor closest to the material properties of Al_4SiC_4.

We have employed an in-house bulk ensemble MC simulation code to foresee electron transport properties of Al_4SiC_4. The bulk MC simulations assume a two-valley model for the conduction band of Al_4SiC_4 because the M and K valleys are principal valley in the conduction band within an analytical non-parabolic anisotropic band structure. The simulation code was enhanced by including a rotational transformation for the lowest conduction band, the M valley. The MC code used electron effective masses extracted from DFT calculations. The DFT calculations have shown that there is a large effective mass in both the longitudinal and transverse directions for the K valley of 1.0569 m_e and 0.9360 m_e, respectively, compared with those for the M valley of 0.6952 m_e and 0.5678 m_e, respectively, where m_e is the electron mass in vacuum. The large effective masses in the M valley have profound impact on the electron drift and mobility.

The MC simulations of Al_4SiC_4 predicted dependence of electron drift velocity, electron mobility, average kinetic energy of electrons, and electron population against the applied electric field, all of which can serve as crucial indicators to assess the electronic and opto-electronic performance of devices. We have shown that the electron drift velocity increases with increasing electric field reaching 1.35×10^7 cms^{-1} at approximately 1400 kVcm^{-1}. The average electron kinetic energy has a linear increase as expected and reaches 1.24 eV at 1400 kVcm^{-1}. The threshold energy barrier, when electrons start to transfer from the M valley to the K valley, occurs at electric field of approximately 450 kVcm^{-1}. When the electric field approaches the critical field of 1831 kVcm^{-1}, the number of electrons with higher energy that is larger than the band gap of the material will start to increase rapidly causing a breakdown of the material.

The bulk transport properties of Al_4SiC_4 predicted by the ensemble Monte Carlo modelling has been compared with properties of know semiconductor materials including drift velocity and electron mobility. A maximum drift velocity of Al_4SiC_4 is only 61.4 % of the maximum drift velocity of GaN (2.2×10^7 cms^{-1}) and electron mobility of Al_4SiC_4 is 19.4 % of the GaN electron mobility (1250 cm^{2}V^{-1}s^{-1}) [138]. When the transport properties of Al_4SiC_4 are compared to 6H-SiC, Al_4SiC_4 is only 67.5 % of the maximum drift velocity of 6H-SiC (2×10^7 cms^{-1}) and only 48.5 % of the 6H-SiC electron mobility (500 cm^{2}V^{-1}s^{-1}) [138]. Finally, when the transport properties are compared to silicon, Al_4SiC_4 is 135 % of the maximum drift velocity of silicon (1×10^7 cms^{-1}) and only 16.17 % of the silicon electron mobility (1500 cm^{2}V^{-1}s^{-1}) [138].

A performance of heterostructure transistor made of SiC/Al_4SiC_4 material system

with a novel ternary carbide of Al_4SiC_4 has been simulated in commercial simulator Atlas by Silvaco using known experimental [126] and theoretical data [132]. The heterostructure transistor with a gate length of 5 μm and two heterostructure transistors scaled to gate lengths of 2 μm and 1 μm, with a respective lateral scaling of the source-to-gate distance, the channel length, and the gate-to-drain distance, have been studied using a drift-diffusion transport model. The variants of asymmetrically scaled heterostructure transistors with the increased gate-to-drain distance to achieve a larger breakdown voltage have been also studied. The device modelling through Silvaco Atlas consider a 2D drift-diffusion transport model with field dependent mobility and Auger recombination simulating both holes and electrons.

The device modeling predicted that all of the devices remained off when assuming a metal gate workfunction of 3.9 eV unless a gate bias was applied. Therefore, the SiC/Al_4SiC_4 heterostructure transistor provides a n-channel enhancement-mode, normally-off device operation. I_D-V_G (drain current-gate voltage) characteristics in a range of drain biases were obtained for the heterostructure device. The I_D-V_G characteristics exhibit well defined linear and saturation regions but the increase in the saturation current in the I_D-V_G characteristics start to reduce with the drain bias increase. This reduction in the increase in the saturation current is due to a limitation in the increase in electron density at the heterostructure interface creating the device channel which is determined by the conduction band off-set. Additionally, transconductance and device breakdown were also investigated and a comparison made between three devices scaled laterally.

The threshold voltage reduces as the gate length is reduced from 71.0 mV to 28.3 mV, and to 28.3 mV for 5 μm, 2 μm, and 1 μm gate length transistors, respectively, and is inline with that seen from AlGaN/GaN HEMTs ranging from −4 V to 0.9 V [153]. Therefore, the device remains off unless a gate bias is applied and all the scaled SiC/Al_4SiC_4 heterostructure transistors provide a n-channel enhancement-mode, normally-off device operation. Sub-threshold slopes of 197.3 mV/dec, 97.6 mV/dec, and 96.1 mV/dec for gate lengths of 5 μm, 2 μm, and 1 μm, respectively, are observed which are, in all cases, much larger than the ideal sub-threshold slope of 60 mV/dec at 300 K.

The bias point at which the device breakdown occurs reduces from 59.0 V to 31.0 V and to 18.0 V as the gate length reduces from 5 μm to 2 μm and to 1 μm, respectively. The breakdown voltage can be increased to 48.25 V when we increase the gate-to-drain spacer to 2.5 μm in the 2 μm gate device, and to 22.75 V and to 29.25 V in the 1 μm gate device when the gate-to-drain spacer is increased to 1.0 μm and to 2.5 μm. In all cases,

this breakdown voltage is lower than the breakdown voltages for AlGaN/GaN HEMTs which are reported to be between 90 V [140] to 600 V [13]. The drain current saturation region occurs at smaller gate bias with the reduction of the gate length. At a large drain voltage of 40 V, a drain current saturation appears at 1.68×10^{-4} A/μm, 2.44×10^{-4} A/μm, and 3.50×10^{-4} A/μm for gate lengths of 5 μm, 2 μm, and 1 μm, respectively. In all cases, the maximum transconductance that has been observed is much smaller than that for AlGaN/GaN HEMTs which sees values like 120 mS/mm [14] compared to the lows of only 0.319 μS/μm in our SiC/Al_4SiC_4 HEMT.

Experimental characterisation was carried out with samples of Al_4SiC_4 employing: (1) UV/Vis/NIR Spectroscopy, (2) XPS, and (3) two- and four-prove DC current voltage measurements. UV/Vis/NIR Spectroscopy was performed on solution grown samples of Al_4SiC_4 [42] in order to ascertain the bandgap of Al_4SiC_4. Because the Al_4SiC_4 samples had a small size. The default apertures for the spectrophotometer were too large for the samples to be attached. Smaller apertures had to be created in order to accommodate the samples of Al_4SiC_4. The measurements from the spectrophotometer ascertained a bandgap of 2.78 eV $\pm$ 0.02 eV. This bandgap was inline with our reports of VEELS experiments [126] that found a bandgap of 2.8 eV $\pm$ 0.2 eV. This bandgap value was then used in the Monte Carlo simulator and device simulator in order to get an accurate prediction of the electron transport properties of Al_4SiC_4.

The XPS was performed on sublimation grown samples of Al_4SiC_4 [141] in order to look at the workfuction, valence band and chemical make-up of Al_4SiC_4. The XPS revealed a thick layer of oxide on the sample which was hard to remove and, therefore, affected our results. The affect of this oxide layer is an indeterminate workfunction as the measurements varied from $5.0 - 2.46$ eV between the two systems and varied depending on the surface treatments. The oxide layer also gave a variation in the position of the valence band and the location of the Fermi level. The position of the Fermi level is directly linked to the thickness of the oxide layer. The thicker the oxidation layer is the larger n-type doping occurred in the material indicated by the valence band sitting at 5.75 eV. As this oxidation layer was reduced through surface treatment, the valence band position reduced to 0.45 eV and the material became lightly p-type doped. The XPS also showed that various surface treatments can remove surface contamination where the oxide was hardest to remove.

The two- and four-probe I-V characteristic measurements were carried out to ascertain the resistivity and the related conductivity of Al_4SiC_4. The two-probe I-V characteristic measurements revealed the resistivity and the conductivity of Al_4SiC_4 to be similar

to 4H-SiC at $2.2 \times 10^{10}\ \Omega m$ and $4.6 \times 10^{-11}\ Sm^{-1}$, respectively. However, the four-probe I-V characteristic measurements proved to be futile as we were unable to contact the samples properly. This was most likely due to a thick layer of oxide residing on the surface of the Al_4SiC_4 samples.

7.2 Conclusion

Al_4SiC_4 is a robust material suitable for use in harsh environments, primarily due to its wide bandgap of 2.78 ± 0.02 eV which was measured by UV/Vis/NIR Spectroscopy. The predicted material properties obtained from our simulations using ensemble MC bulk code indicate a limited usage of the Al_4SiC_4 as a channel material of potential metal-oxide-semiconductor field effect transistors (MOSFETs) due to a maximum electron drift velocity and electron mobility of 1.35×10^7 cms^{-1} and 242.5 cm^{2}V^{-1}s^{-1}, respectively. Al_4SiC_4 has a lower electron drift velocity compared to GaN. However, the drift velocity gives better continuity at high electric field which could be of some benefit to the power electronic applications. The low electron drift velocity and electron mobility is primarily due to the high electron effective masses that were extracted from band-structure data obtained by DFT calculations. Future works would need to look at the values for the electron effective mass to see if experimental works can confirm the predicted electron mobility and electron drift velocity. Al_4SiC_4 would also need to be grown in larger crystal sizes than what was used in this work as it was very difficult at times to use the samples of sizes smaller than 5mm^2.

It is therefore the opinion of the author that Al_4SiC_4 would be a suitable material to complement 4H-SiC in order to make heterostructure devices of SiC/Al_4SiC_4 such as HEMTs or based on quantum wells. However, the large electron effective mass that has been extracted from the DFT calculations [52] in this study gives a limited electron drift velocity and electron mobility which impair the usability of Al_4SiC_4 for electronic applications. There is also scope for Al_4SiC_4 to be used in optoelectronic applications due to its wide bandgap of 2.78 ± 0.02 eV which is in the green light region of the visible light spectrum and could lead way to new green LED being produced. Finally there is scope for Al_4SiC_4 to be used in sensors where one envisions Al_4SiC_4 to be used in X-ray detector due to its potential to withstand large amounts of radiation. Here Al4SiC4 could be used as a stand alone material or in parallel with SiC X-ray detectors [36].

Bibliography

[1] J. Fan and P. K. Chu.
Silicon carbide nanostructures: fabrication, structure, and properties.
Springer, 2014.

[2] T. P. Chow, D. K. Gaskill, C. D. Brandt, and R. J. Nemanich.
III-nitride, SiC, and diamond materials for electronic devices.
In *Eds. Gaskill DK, Brandt CD and Nemanich RJ, Material Research Society Symposium Proceedings, Pittsburgh, PA. 423 (1996)*, pages 69–73, 1996.

[3] D. J. Frank.
Power-constrained CMOS scaling limits.
IBM Journal of Research and Development, 46(2.3):235–244, 2002.

[4] M. Fleischer.
The abundance and distribution of the chemical elements in the earth's crust.
Journal of Chemical Education, 31(9):446, 1954.

[5] R. W. Keyes.
Physical limits of silicon transistors and circuits.
Reports on Progress in Physics, 68(12):2701, 2005.

[6] Z. Galazka.
β-Ga2O3 for wide-bandgap electronics and optoelectronics.
Semiconductor Science and Technology, 33(11):113001, 2018.

[7] O. Mostaghimi, N. Wright, and A. Horsfall.
Design and performance evaluation of SiC based DC-DC converters for PV applications.
In *2012 IEEE Energy Conversion Congress and Exposition (ECCE)*, pages 3956–3963. IEEE, 2012.

[8] R. Ramachandran and M. Nymand.
Experimental demonstration of a 98.8% efficient isolated DC–DC GaN converter.
IEEE Transactions on Industrial Electronics, 64(11):9104–9113, 2016.

[9] S. Zhang, G. Lan, Z. Dong, and X. Wu.
A High Efficiency two-stage ZVS AC/DC converter with all SiC MOSFET.
In *2017 IEEE 3rd International Future Energy Electronics Conference and ECCE Asia (IFEEC 2017-ECCE Asia)*, pages 163–169. IEEE, 2017.

[10] A. De Bernardinis, A. Kolli, J. P. Ousten, and R. Lallemand.
High efficiency Silicon carbide DC-AC inverter for EV-charging Flywheel system.
In *2017 IEEE Transportation Electrification Conference and Expo (ITEC)*, pages 421–424. IEEE, 2017.

[11] M. Bhatnagar, P. K. McLarty, and B. J. Baliga.
Silicon-carbide high-voltage (400 V) Schottky barrier diodes.
IEEE Electron Device Letters, 13(10):501–503, 1992.

[12] A. Elasser, M. H. Kheraluwala, M. Ghezzo, R. L. Steigerwald, N. A. Evers, J. Kretchmer, and T. P. Chow.
A comparative evaluation of new silicon carbide diodes and state-of-the-art silicon diodes for power electronic applications.
IEEE Transactions on Industry Applications, 39(4):915–921, 2003.

[13] W. Saito, Y. Takada, M. Kuraguchi, K. Tsuda, I. Omura, T. Ogura, and H. Ohashi.
High breakdown voltage AlGaN-GaN power-HEMT design and high current density switching behavior.
IEEE Transactions on electron devices, 50(12):2528–2531, 2003.

[14] E. Y. Chang.
GaN HEMT on Si for high power applications.
In *2011 IEEE Regional Symposium on Micro and Nano Electronics*, pages A2–A2. IEEE, 2011.

[15] C. J. Humphreys.
Solid-state lighting.
MRS Bulletin, 33(4):459–470, 2008.

[16] Y. K. Cheng and K. W. E. Cheng.

General study for using LED to replace traditional lighting devices.
In *2006 2nd International Conference on Power Electronics Systems and Applications*, pages 173–177. IEEE, 2006.

[17] E. F. Schubert, J. Cho, and J. K. Kim.
Light-emitting diodes.
Kirk-Othmer Encyclopedia of Chemical Technology, pages 1–20, 2000.

[18] G. Zorpette.
Let there be light.
IEEE Spectrum, 39(9):70–74, 2002.

[19] M. Zhang, J. Wang, Q. Zhang, W. Ding, and Q. Su.
Optical properties of Ba2SiO4: Eu2+ phosphor for green light-emitting diode (LED).
Materials Research Bulletin, 42(1):33–39, 2007.

[20] R. Sharma, P. M. Pattison, H. Masui, R. M. Farrell, T. J. Baker, B. A. Haskell, F. Wu, S. P. DenBaars, J. S. Speck, and S. Nakamura.
Demonstration of a semipolar (10 1¯ 3¯) In Ga N/ Ga N green light emitting diode.
Applied Physics Letters, 87(23):231110, 2005.

[21] S. J. Pearton, F. Ren, Y. L. Wang, B. H. Chu, K. H. Chen, C. Y. Chang, W. Lim, J. Lin, and D. P. Norton.
Recent advances in wide bandgap semiconductor biological and gas sensors.
Progress in Materials Science, 55(1):1–59, 2010.

[22] H. Nanto, T. Minami, and S. Takata.
Zinc-oxide thin-film ammonia gas sensors with high sensitivity and excellent selectivity.
Journal of Applied Physics, 60(2):482–484, 1986.

[23] K. S. Weißenrieder and J. Müller.
Conductivity model for sputtered ZnO-thin film gas sensors.
Thin Solid Films, 300(1-2):30–41, 1997.

[24] J. F. Chang, H. H. Kuo, I. C. Leu, and M. H. Hon.
The effects of thickness and operation temperature on ZnO: Al thin film CO gas sensor.
Sensors and Actuators B: Chemical, 84(2-3):258–264, 2002.

[25] A. Cusano, F. J. Arregui, M. Giordano, and A. Cutolo.
Optochemical Nanosensors.
Series in Sensors. CRC Press, 2016.

[26] W. Lim, J. S. Wright, B. P. Gila, J. L. Johnson, A. Ural, T. Anderson, F. Ren, and S. J. Pearton.
Room temperature hydrogen detection using Pd-coated GaN nanowires.
Applied Physics Letters, 93(7):072109, 2008.

[27] S. Roy, C. Jacob, and S. Basu.
Studies on Pd/3C-SiC Schottky junction hydrogen sensors at high temperature.
Sensors and Actuators B: Chemical, 94(3):298–303, 2003.

[28] M. Andersson, H. Wingbrant, and A. L. Spetz.
Study of the CO response of SiC based field effect gas sensors.
In *SENSORS, 2005 IEEE*, page 4. IEEE, 2005.

[29] Z. Darmastuti, R. Pearce, A. L. Spetz, and M. Andersson.
The influence of gate bias and structure on the CO sensing performance of SiC based field effect sensors.
In *SENSORS, 2011 IEEE*, pages 133–136. IEEE, 2011.

[30] M. Aslam, V. A. Chaudhary, I. S. Mulla, S. R. Sainkar, A. B. Mandale, A. A. Belhekar, and K. Vijayamohanan.
A highly selective ammonia gas sensor using surface-ruthenated zinc oxide.
Sensors and Actuators A: Physical, 75(2):162–167, 1999.

[31] C. S. Lao, M. C. Park, Q. Kuang, Y. Deng, A. K. Sood, D. L. Polla, and Z. L. Wang.
Giant enhancement in UV response of ZnO nanobelts by polymer surface-functionalization.
Journal of the American Chemical Society, 129(40):12096–12097, 2007.

[32] T. C. Chen, Y. T. Lin, C. Y. Lin, W. C. Chen, M. R. Chen, H. L. Kao, J. I. Chyi, and C. H. Hsu.
Suitability of surface acoustic wave oscillators fabricated using low temperature-grown AlN films on GaN/sapphire as UV sensors.
IEEE Transactions on Ultrasonics, Ferroelectrics, and Frequency Control, 55(2):489–493, 2008.

[33] V. M. Zaletin.
Development of semiconductor detectors based on wide-gap materials.
Atomic Energy, 97(5):773–780, 2004.

[34] R. Bellazzini, G. Spandre, A. Brez, M. Minuti, M. Pinchera, and P. Mozzo.
Chromatic X-ray imaging with a fine pitch CdTe sensor coupled to a large area photon counting pixel ASIC.
Journal of Instrumentation, 8(02):C02028, 2013.

[35] D. S. McGregor, Z. He, H. A. Seifert, D. K. Wehe, and R. A. Rojeski.
Single charge carrier type sensing with a parallel strip pseudo-Frisch-grid CdZnTe semiconductor radiation detector.
Applied Physics Letters, 72(7):792–794, 1998.

[36] G. Bertuccio and R. Casiraghi.
Study of silicon carbide for X-ray detection and spectroscopy.
IEEE Transactions on Nuclear Science, 50(1):175–185, 2003.

[37] S. Zhu, H. Jia, T. Li, Y. Tong, Y. Liang, X. Wang, T. Zeng, and Y. Yang.
Novel High-Energy-Efficiency AlGaN/GaN HEMT with High Gate and Multi-Recessed Buffer.
Micromachines, 10(7):444, 2019.

[38] F. A. Ponce and D. P. Bour.
Nitride-based semiconductors for blue and green light-emitting devices.
Nature, 386(6623):351, 1997.

[39] J. E. Lees, A. M. Barnett, D. J. Bassford, R. C. Stevens, and A. B. Horsfall.
SiC X-ray detectors for harsh environments.
Journal of Instrumentation, 6(01):C01032, 2011.

[40] ATLAS User's Manual.
SILVACO Int.
Santa Clara, CA, 5, 2008.

[41] V.J. Barczak.
Optical and X-Ray Powder Diffraction Data for $Al_4Si_2C_5$.
American Ceramic Society, 44:274, 1961.

[42] D. Zevgitis, O. Chaix-Pluchery, B. Doisneau, M. Modreanu, J. La Manna, E. Sarigiannidou, and D. Chaussende.
Synthesis and Characterization of Al_4SiC_4: A "New" Wide Band Gap Semiconductor Material.
In *Materials Science Forum*, volume 821-823, pages 974–977. Trans Tech Publ, 2015.

[43] L. Pedesseau, O. Chaix-Pluchery, M. Modreanu, D. Chaussende, E. Sarigiannidou, A. Rolland, J. Even, and O. Durand.
Al_4SiC_4 vibrational properties: density functional theory calculations compared to Raman and infrared spectroscopy measurements.
Journal of Raman Spectroscopy, 48(6):891–896, 2017.

[44] H. L Le-Tran, E. Sarigiannidou, I. Gélard, and D. Chaussende.
Vaporization and condensation in the Al_4C_3-SiC system.
Journal of the European Ceramic Society, 37(15):4475–4482, 2017.

[45] A. Yamaguchi and S. Zhang.
Synthesis and some properties of Al_4SiC_4.
Nippon Seramikkusu Kyokai Gakujutsu Ronbunshi-Journal of the Ceramic Society of Japan, 103(1):20–24, 1995.

[46] O. Yamamoto, M. Ohtani, and T. Sasamoto.
Preparation and oxidation of Al_4SiC_4.
Journal of Materials Research, 17(4):774–778, 2002.

[47] K. Inoue, A. Yamaguchi, and S. Hashimoto.
Fabrication and oxidation resistance of A(14)SiC(4) body.
Journal of the Ceramic Society of Japan, 110(11):1010–1015, 2002.

[48] J Grobner, H. L. Lukas, and F. Aldinger.
Thermodynamic calculation of the ternary system Al-Si-C.
Calphad-Computer Coupling of Phase Diagrams and Thermochemistry, 20(2):247–254, 1996.

[49] T. Liao, J. Y. Wang, and Y. C. Zhou.
Atomistic deformation modes and intrinsic brittleness of Al_4SiC_4: A first-principles investigation.
Physical Review B, 74(17), 2006.

[50] A. Hussain, S. Aryal, P. Rulis, M. A. Choudhry, and W. Y. Ching.
Density functional calculations of the electronic structure and optical properties of the ternary carbides Al_4SiC_4 and $Al_4Si_2C_5$.
Physical Review B, 78(19), 2008.

[51] J. P Perdew and A. Zunger.
Self-interaction correction to density-functional approximations for many-electron systems.
Physical Review B, 23(10):5048, 1981.

[52] L. Pedesseau, J. Even, M. Modreanu, D. Chaussende, E. Sarigiannidou, O. Chaix-Pluchery, and O. Durand.
Al_4SiC_4 wurtzite crystal: Structural, optoelectronic, elastic, and piezoelectric properties.
APL Materials, 3(12):121101, 2015.

[53] Y. F. Li, B. Xiao, L. Sun, Y. M. Gao, and Y. H. Cheng.
A Theoretical Study of Dielectric Tensor, Born Effective Charges, LO-TO Splitting and Infrared Response of Al_4SiC_4 and $Al_4Si_2C_5$.
Journal of Alloys and Compounds, 692:713–719, 2017.

[54] L. Sun, Y. Gao, Y. Li, K. Yoshida, T. Yano, and D. Yi.
Structural, bonding, anisotropic mechanical and thermal properties of Al_4SiC_4 and $Al_4Si_2C_5$ by first- principles investigations.
Journal of Asian Ceramic Societies, 4(3):289–298, 2016.

[55] G. Schneider, L. J. Gauckler, G. Petzow, and A. Zangvil.
Phase Equilibria in the System Al_4C_3-Be_2C-SiC.
Journal of the American Ceramic Society, 62(11?12):574–576, 1979.

[56] Z. Inoue, Y. Inomata, H. Tanaka, and H. Kawabata.
X-ray crystallographic data on aluminum silicon carbide, α-Al 4 SiC 4 and $Al_4Si_2C_5$.
Journal of Materials Science, 15(3):575–580, 1980.

[57] J. Schoennahl, B. Willer, and M. Daire.
The mixed carbide Al_4SiC_4 - Preparation and Structural Data.
Journal of Solid State Chemistry, 52(2):163–173, 1984.

[58] R. P. Beyer and E. A. Johnson.
Heat capacity of aluminum silicon carbide (Al_4SiC_4) from 5.26 to 1047 K.
The Journal of Chemical Thermodynamics, 16(11):1025–1029, 1984.

[59] R. G. Behrens and G. H. Rinehart.
Vaporization thermodynamics and enthalpy of formation of aluminum silicon carbide.
Journal of the American Ceramic Society, 67(8):575–578, 1984.

[60] B. L. Kidwell, L. L. Oden, and R. A. McCune.
$2Al_4C_3SiC$: a new intermediate phase in the Al–Si–C system.
Journal of Applied Crystallography, 17(6):481–482, 1984.

[61] L. L. Oden and R. A. McCune.
Phase equilibria in the Al-Si-C system.
Metallurgical Transactions A, 18(12):2005–2014, 1987.

[62] L. L. Oden and R. A. McCune.
Contribution to the Phase Diagram Al_4C_3-AIN-SiC.
Journal of the American Ceramic Society, 73(6):1529–1533, 1990.

[63] J. Gröbner, H. L. Lukas, and F. Aldinger.
Thermodynamic calculations in the Y-Al-C system.
Journal of Alloys and Compounds, 220(1-2):8–14, 1995.

[64] T. I. Barry, A. T. Dinsdale, J. A. Gisby, B. Hallstedt, M. Hillert, B. Jansson, S. Jonsson, B. Sundman, and J. R. Taylor.
The compound energy model for ionic solutions with applications to solid oxides.
Journal of Phase Equilibria, 13(5):459–475, 1992.

[65] H. Kleykamp and G. Schumacher.
The constitution of the silicon-carbon system.
Berichte der Bunsengesellschaft für physikalische Chemie, 97(6):799–804, 1993.

[66] A. Magnus.
Die spezifische wärme des kohlenstoffs, siliziums und siliziumkarbids bei hohen temperaturen.
Annalen der Physik, 375(4):303–331, 1923.

[67] E. A. Guseva, A. S. Bolgar, S. P. Gordienko, V. A. Gorbatyuk, and V. V. Fesenko.
Determination of the enthalpy of self-bonded silicon carbide in the temperature range 1300–2000 K.
Teplofizika Vysokikh Temperatur, 4(5):649–652, 1966.

[68] V. Y. Chekhovskoy.
Enthalpy and thermodynamic properties of SiC at temperatures up to 2900 K.
The Journal of Chemical Thermodynamics, 3(3):289–296, 1971.

[69] R. P. Beyer and E. A. Johnson.
Heat capacity of aluminum silicon carbide (Al_4SiC_4) from 5.26 to 1047 K.
The Journal of Chemical Thermodynamics, 16(11):1025–1029, 1984.

[70] L. L. Oden, , and R. A. McCune.
Phase equilibria in the Al-Si-C system.
Metallurgical Transactions A, 18(12):2005–2014, 1987.

[71] L. L. Oden and R. P. Beyer.
Heat capacity of $2Al_4C_3SiC$ from 447 to 1447 K and enthalpy of peritectic decomposition of Al_4C_3, $2Al_4C_3SiC$, and Al_4C_3SiC.
Thermochimica Acta, 115:11–19, 1987.

[72] K. Inoue and A. Yamaguchi.
Temperature dependence of electrical resistivity of the Al_4SiC_4 sintered bodies prepared by pulse electronic current sintering.
Journal of the Ceramic Society of Japan, 111(4):267–270, 2003.

[73] K. Inoue and A. Yamaguchi.
Synthesis of Al_4SiC_4.
Journal of the American Ceramic Society, 86(6):1028–1030, 2003.

[74] G. W. Wen and X. X. Huang.
Increased high temperature strength and oxidation resistance of Al_4SiC_4 ceramics.
Journal of the European Ceramic Society, 26(7):1281–1286, 2006.

[75] V. L. Solozhenko and O. O. Kurakevych.
Equation of state of aluminum silicon carbide alpha-Al_4SiC_4.
Solid State Communications, 135(1-2):87–89, 2005.

[76] J. L. Zhao, W. Lin, A. Yamaguchi, J. Ommyoji, and J. Sun.
Synthesis of Al_4SiC_4 from alumina, silica and graphite.
Journal of the Ceramic Society of Japan, 115(1347):761–766, 2007.

[77] D. Chengji, K. Jianlei, Z. Hongxi, and B. Chen.
Effects of Fe_2O_3 on synthesis of Al_4SiC_4/Al_4O_4C composite refractory from natural raw materials.
Journal of the Chinese Ceramic Society, 8:049, 2010.

[78] Y. Sun, H. Cui, L. Gong, J. Chen, J. She, Y. Ma, P. Shen, and C. Wang.
Carbon-in-Al_4C_3 nanowire superstructures for field emitters.
ACS Nano, 5(2):932–941, 2011.

[79] M. S Shur.
Handbook series on semiconductor parameters, volume 1.
World Scientific, 1996.

[80] Y. A. Goldberg and N. M. Schmidt.
Handbook series on semiconductor parameters.
Volume, 1:191–213, 1999.

[81] S. Kasap and P. Capper.
Springer handbook of electronic and photonic Materials.
Springer Handbooks. Springer US, 2017.

[82] L. Patrick and W. J. Choyke.
Static dielectric constant of SiC.
Physical Review B, 2(6):2255, 1970.

[83] S. Y. Davydov.
Estimates of the spontaneous polarization and permittivities of AlN, GaN, InN, and SiC crystals.
Physics of the Solid State, 51(6):1231–1235, 2009.

[84] H. Iwata and K. M. Itoh.
Donor and acceptor concentration dependence of the electron Hall mobility and the Hall scattering factor in n-type 4H-and 6H-SiC.
Journal of Applied Physics, 89(11):6228–6234, 2001.

[85] P. Hohenberg and W. Kohn.
Density Functional Theory (DFT).
Physical Review Journals, 136:B864, 1964.

[86] D. Pines.
Elementary excitations in solids.
CRC Press, 2018.

[87] S. M. Sze and K. K. Ng.
Physics of semiconductor devices.
John Wiley & Sons, 2006.

[88] M. Lundstrom.
Fundamentals of Carrier Transport.
Cambridge University Press, Cambridge; New York, 2nd ed. edition, 2000.

[89] K. Banoo, M. Lundstrom, and R. K. Smith.
Direct solution of the Boltzmann transport equation in nanoscale Si devices.
In *2000 International Conference on Simulation Semiconductor Processes and Devices*, pages 50–53. IEEE, 2000.

[90] S. A. Trugman and A. J. Taylor.
Analytic solution of the Boltzmann equation with applications to electron transport in inhomogeneous semiconductors.
Physical Review B, 33(8):5575, 1986.

[91] N. Goldsman, L. Henrickson, and J. Frey.
A physics-based analytical/numerical solution to the Boltzmann transport equation for use in device simulation.
Solid-State Electronics, 34(4):389–396, 1991.

[92] L. Pareschi and G. Russo.
An introduction to Monte Carlo method for the Boltzmann equation.
In *ESAIM: Proceedings*, volume 10, pages 35–75. EDP Sciences, 2001.

[93] M. Lenzi, P. Palestri, E. Gnani, S. Reggiani, A. Gnudi, D. Esseni, L. Selmi, and G. Baccarani.
Investigation of the transport properties of silicon nanowires using deterministic and Monte Carlo approaches to the solution of the Boltzmann transport equation.

IEEE Transactions on Electron Devices, 55(8):2086–2096, 2008.

[94] J. Zimmermann, P. Lugli, and D. K. Ferry.
On the physics and modeling of small semiconductor devices-IV. Generalized, retarded transport in ensemble Monte Carlo techniques.
Solid-State Electronics, 26(3):233–239, 1983.

[95] C. Jacoboni and L. Reggiani.
The Monte Carlo method for the solution of charge transport in semiconductors with applications to covalent materials.
Reviews of Modern Physics, 55(3):645, 1983.

[96] T. Kurosawa and H. Maeda.
Monte Carlo calculation of hot electron phenomena. I. Streaming in the absence of a magnetic field.
Journal of the Physical Society of Japan, 31(3):668–678, 1971.

[97] C. Jacoboni and P. Lugli.
The Monte Carlo method for semiconductor device simulation.
Springer Science & Business Media, 2012.

[98] H. D. Rees.
Calculation of distribution functions by exploiting the stability of the steady state.
Journal of Physics and Chemistry of Solids, 30(3):643–655, 1969.

[99] C. Moglestue.
Monte Carlo simulation of semiconductor devices.
London : Chapman and Hall, London, 1993.

[100] D. Vasileska, S. M. Goodnick, and G. Klimeck.
Computational electronics: Semiclassical and quantum device modeling and simulation.
CRC press, 2016.

[101] B. K. Ridley.
Quantum processes in semiconductors.
Oxford University Press, 2013.

[102] B. K. Ridley.
Electrons and phonons in semiconductor multilayers, volume 5.

Cambridge University Press, 2009.

[103] D. K. Ferry.
Semiconductors.
Macmillan Publishers Company, 1991.

[104] K. Tomizawa.
Numerical simulation of submicron semiconductor devices.
Artech House Materials Science Library. Artech House Publishers, 1993.

[105] I. Aynul.
Monte Carlo device modelling of electron transport in nanoscale transistors.
PhD thesis, Swansea University, 2012.

[106] J. G. Ruch and W. Fawcett.
Temperature dependence of the transport properties of gallium arsenide determined by a Monte Carlo method.
Journal of Applied Physics, 41(9):3843–3849, 1970.

[107] L. V. Keldysh.
Concerning the Theory of Impact Ionization in Semiconductors.
Soviet Journal of Experimental and Theoretical Physics, 21:1135, December 1965.

[108] D. F. Swinehart.
The Beer-Lambert law.
Journal of Chemical Education, 39(7):333, 1962.

[109] K. Skorupska.
Optical properties of semiconductors.
Lecture notes. Available: http: / / www. uwyo. edu / cpac / _files / docs / kasia_lectures / 3-opticalproperties. pdf. [Accessed: 17-Sep-2019].

[110] K. H. J. Buschow, R. W. Cahn, M. C Flemings, B. Ilschner, E. J. Kramer, and S. Mahajan.
Encyclopedia of materials.
Science and Technology, 1:11, 2001.

[111] A. McClelland and M. Mankin.
Optical Measurements for Scientists and Engineers: A Practical Guide.
Cambridge University Press, 2018.

[112] T. S. Moss and T. D. F. Hawkins.
Infrared absorption in gallium arsenide.
Infrared Physics, 1(2):111–115, 1961.

[113] T. S. Moss.
The potentialities of silicon and gallium arsenide solar batteries.
Solid-State Electronics, 2(4):222–231, 1961.

[114] A. Rockett.
The Materials Science of Semiconductors.
Springer US, 2007.

[115] D. Redfield.
Energy-band tails and the optical absorption edge; the case of a-Si: H.
Solid State Communications, 44(9):1347–1349, 1982.

[116] S. K. O'Leary.
On the relationship between the distribution of electronic states and the optical absorption spectrum in amorphous semiconductors.
Solid State Communications, 109(9):589–594, 1999.

[117] P. Van Mieghem.
Theory of band tails in heavily doped semiconductors.
Reviews of Modern Physics, 64(3):755, 1992.

[118] G. A. N. Connell.
Optical properties of amorphous semiconductors.
In *Amorphous Semiconductors*, pages 73–111. Springer, 1979.

[119] L. Pauw.
A method of measuring specific resistivity and Hall effect of discs of arbitrary shape.
Philips Research Reports, 13(2):1–9, 1958.

[120] W. T. R. W. Shockley and W. T. Read Jr.
Statistics of the recombinations of holes and electrons.
Physical Review, 87(5):835, 1952.

[121] V. Palankovski and R. Quay.
Analysis and simulation of heterostructure devices.

Springer Science, 2004.

[122] C. K. Sarkar.
Technology computer aided design: simulation for VLSI MOSFET.
CRC Press, 2013.

[123] S. Selberherr.
Analysis and simulation of semiconductor devices.
Springer Science & Business Media, 2012.

[124] K. Tomizawa, Y. Awano, N. Hashizume, and F. Suzuki.
Monte Carlo Simulation of GaAs Submicron n+-n-n+ Diode with GaAlAs Heterojunction Cathode.
Electronics Letters, 18(25):1067–1069, December 1982.

[125] A. Islam and K. Kalna.
Monte Carlo simulations of mobility in doped GaAs using self-consistent Fermi-Dirac statistics.
Semiconductor Science and Technology, 26(5):055007, 2011.

[126] S. Forster, J. Cañas, F. Lloret, M. Gutiérrez, D. Araujo, K. Kalna, and D. Chaussende.
Experimental Extraction of the Bandgap for Al_4SiC_4.
In *Proceedings of UK Semiconductor*, 2018.

[127] M. A. Elmessary, N. Daniel, M. Aldegunde, N. Seoane, G. Indalecio, J. Lindberg, W. Dettmer, D. Perić, Antonio J. García-Loureiro, and K. Kalna.
Scaling/LER study of Si GAA nanowire FET using 3D finite element Monte Carlo simulations.
Solid State Electronics, 128:17–24, 2017.

[128] J. L. Hudgins.
An Assessment of Wide Bandgap Semiconductors for Power Devices.
IEEE Transactions on Power Electronics, 18(3):907–915, May 2003.

[129] C. Herring and E. Vogt.
Transport and deformation - potential theory for many-valley semiconductors with anisotropic scattering.
Physical Review, 101(3):944–961, 1956.

[130] PerkinElmer Company.
LAMBDA 950 UV/Vis Spectrophotometer. https://www-punchout.perkinelmer.com/product/lambda-950-uv-vis-nir-spectrophotometer-l950 [accessed Feb. 11 2020].

[131] S. Dimitrijev.
Principles of semiconductor devices.
Oxford University Press, USA, 2006.

[132] S. Forster, D. Chaussende, and K. Kalna.
Monte Carlo Simulations of Electron Transport Characteristics of Ternary Carbide Al_4SiC_4.
ACS Applied Energy Materials, 2(1):715–720, 2019.

[133] G. L. Harris.
Properties of silicon carbide.
Number 13. Iet, 1995.

[134] A. Arvanitopoulos, N. Lophitis, S. Perkins, K. N. Gyftakis, M. B. Guadas, and M. Antoniou.
Physical parameterisation of 3C-Silicon Carbide (SiC) with scope to evaluate the suitability of the material for power diodes as an alternative to 4H-SiC.
In *2017 IEEE 11th Symposium on Diagnostics for Electric Machines, Power Electronics and Drives (SDEMPED)*, pages 565–571. IEEE, 2017.

[135] T. Yuan.
An analytical solution to a double-gate MOSFET with undoped body.
IEEE Electron Device Letters, 21(5):245–247, 2000.

[136] K. Boucart and A. M. Ionescu.
Double-Gate Tunnel FET With High-κ Gate Dielectric.
IEEE Transactions on Electron Devices, 54(7):1725–1733, 2007.

[137] N. Q. Zhang, S. Keller, G. Parish, S. Heikman, S. P. DenBaars, and U. K. Mishra.
High breakdown GaN HEMT with overlapping gate structure.
IEEE Electron Device Letters, 21(9):421–423, 2000.

[138] B. Ozpineci and L. M. Tolbert.
Comparison of wide-bandgap semiconductors for power electronics applications.
United States. Department of Energy, 2004.

[139] X. Liu, H. Gu, K. Li, L. Guo, D. Zhu, Y. Lu, J. Wang, H. C. Kuo, Z. Liu, and W. Liu.
AlGaN/GaN high electron mobility transistors with a low sub-threshold swing on free-standing GaN wafer.
AIP Advances, 7(9):095305, 2017.

[140] L. Shen, R. Coffie, D. Buttari, S. Heikman, A. Chakraborty, A. Chini, S. Keller, S. P. DenBaars, and U. K. Mishra.
High-power polarization-engineered GaN/AlGaN/GaN HEMTs without surface passivation.
IEEE Electron Device Letters, 25(1):7–9, 2004.

[141] L. Tran and H. Long.
Croissance en phase gazeuse d'Al_4SiC_4 et étude d'hétérostructures dans lesystème Al-Si-C sur SiC.
PhD thesis, Grenoble Alpes, 2018.

[142] I. Studenyak, M. Kranjčec, and M. Kurik.
Urbach rule in solid state physics.
International Journal of Optics and Applications, 4(3):96–104, 2014.

[143] Forster, S. and Cañas, J. and Lloret, F. and Gutiérrez, M. and Araujo, D. and Kalna, K. and Chaussende, D.
Experimental study of al_4sic_4.
In *Proceedings of Zienkeiwicz Centre for Computational Engineering*, 2019.

[144] Forster, S. and Cañas, J. and Lloret, F. and Gutiérrez, M. and Araujo, D. and Kalna, K. and Chaussende, D.
Experimental Extraction of the Bandgap for Al_4SiC_4.
In *Proceedings of The European Conference on Silicon Carbide and Related Materials (ECSCRM)*, 2018.

[145] H. C. Casey Jr, D. D. Sell, and K. W. Wecht.
Concentration dependence of the absorption coefficient for n- and p- type GaAs between 1.3 and 1.6 eV.
Journal of Applied Physics, 46(1):250–257, 1975.

[146] Z. Jiang, X. Xu, H. Wu, F. Zhang, and Z. Jin.
Ab initio calculation of SiC polytypes.
Solid State Communications, 123(6-7):263–266, 2002.

[147] J. Goldberg.
Properties of Advanced Semiconductor Materials: GaN, AlN, InN, BN, SiC, SiGe.
Inc., New York, page 31, 2001.

[148] L. Tran and H. Long.
Growth in gas phase of Al4SiC4 and étude d'Hétérostructures in le système Al-Si-C on SiC.
PhD thesis, Grenoble Alpes, 2018.

[149] V. K. Agarwala and T. Fort Jr.
Nature of the stable oxide layer formed on an aluminum surface by work function measurements.
Surface Science, 54(1):60–70, 1976.

[150] P. Vinet, T. Lemogne, and H. Montes.
Aluminum work function: Effect of oxidation, mechanical scraping and ion bombardment.
National Aeronautics and Space Administration, 1985.

[151] S. Porowski, M. Boćkowski, B. Łucznik, I. Grzegory, M. Wroblewski, H. Teisseyre, M. Leszczyński, E. Litwin-Staszewska, T. Suski, and P. Trautman.
High Resistivity GaN Single Crystalline Substrates.
Acta Physica Polonica A, 5(92):958–962, 1997.

[152] M. Lu.
Semiconductors: Silicon Carbide and Related Materials.
Materials Science Forum. Trans Tech Publications, Limited, 2019.

[153] Y. Cai, Y. Zhou, K. M. Lau, and K. J. Chen.
Control of threshold voltage of AlGaN/GaN HEMTs by fluoride-based plasma treatment: From depletion mode to enhancement mode.
IEEE Transactions on Electron Devices, 53(9):2207–2215, 2006.